The Dissertation Committee for Linda Tae Nieman certifies that this is the approved version of the following dissertation:

Early Detection of Curable Precancerous Lesions in the Oral Cavity Using Polarized Reflectance Spectroscopy

Committee:

Konstantin Sokolov, Co-Supervisor

Mark Raizen, Co-Supervisor

Rebecca Richards-Kortum

Linda Reichl

Chih-Kang Shih

Early Detection of Curable Precancerous Lesions in the Oral Cavity Using Polarized Reflectance Spectroscopy

by

Linda Tae Nieman, B. S., M. A.

Dissertation

Presented to the Faculty of the Graduate School of
The University of Texas at Austin
in Partial Fulfillment
of the Requirements
for the Degree of

Doctor of Philosophy

The University of Texas at Austin

August 2004

Dedication

To my mom, for always being there with support and love.

Acknowledgements

I would like to thank some of the people who, without their support, this dissertation could not have been written. First, I want to thank my advisor, Kostia, for his guidance and enthusiasm. I remember an email he sent me when I first began working in the lab, which ended with "work hard, have fun, and make fun of others." In this great environment, the long hours required for this doctoral work flew by. And on days when nothing seemed to work, his steadfast encouragement and humor made all the difference.

I would also like to thank Dr. Rebecca Richards-Kortum for her critical insight and guidance with my research. She is also a great role model, proving that it is possible to balance career and family.

At MD Anderson Cancer Center there are several people who I'd like to thank for their tremendous help. First, I'd like to thank Dr. Ann Gillenwater, the collaborating physician. Without her I would have never gotten through the clinical pilot study. I'd like to thank Qasim Hasan and Reza Naderi for being the uncomplaining and patient intermediaries between clinician and engineer. I'd also like to thank Dr. Adel El-Naggar for taking time out of his busy schedule to do pathology readings of my slides.

Finally, I'd like to I'd like to thank my family and the friends that have provided a crucial support network for me when things got tough. I'd also like to thank the great friendly people in the lab. The time I have spent in this lab has been full of laughter as well as exciting research.

Early Detection of Curable Precancerous Lesions in the Oral Cavity Using Polarized Reflectance Spectroscopy

Publication No. ___________

Linda Tae Nieman, Ph.D.

The University of Texas at Austin, 2004

Co-supervisor: Konstantin Sokolov

Co-supervisor: Mark Raizen

In 2004, the American Cancer Society estimates that more than 1,500 deaths a day associated with cancer will occur. For all cancers, the five-year survival rate is greater if diagnosis is made at an early stage of cancer development. The focus of this dissertation is on the development of a highly selective and sensitive non-invasive optical device for the early detection of epithelial precancers, which has enormous potential to reduce patient morbidity and mortality. Specifically, this dissertation will concentrate on the assessment of the polarized reflectance spectroscopy (PRS) to detect and diagnose early curable precancerous lesions within the oral cavity.

PRS is a variation of elastic scattering spectroscopy which is sensitive to important morphological indicators of early precancer, such as scatterer size and refractive index. In this dissertation I will present a fiber optic probe that combines polarized illumination and detection with an angled distal probe geometry to detect the size dependent scattering within the epithelial layer of tissue, where most cancer originate. This technique allows a simple Mie theory based model to be used to extract the nuclear sizes.

Tissue phantoms that mimic the two-layered scattering structure of mucosal tissue were used to test the feasibility of PRS to extract scatter sizes. Results of these studies showed excellent agreement between spectroscopically derived scatter sizes and direct microscopy measurements. *In vivo* measurements within the oral cavity of normal volunteers also yielded nuclear sizes that corresponded very well to published values.

The PRS device was found to be capable of discriminating normal oral mucosa tissue from severe dysplasia in a collaborative pilot clinical trial of 21 patients, at the UT MD Anderson Cancer Center. Nuclear morphology extracted from the polarized spectroscopy measurements compared very well to quantitative histopathology.

Overall this dissertation gives a thorough basis for a larger statistically significant clinical trial to be performed to determine the sensitivity and specificity of polarized reflectance spectroscopy as a screening and diagnostic instrument in the oral cavity. The work in this dissertation lays the foundation for future exploration of the optical scattering properties polarized light within tissue for clinical applications.

TABLE OF CONTENTS

LIST OF TABLES

LIST OF FIGURES

CHAPTER 1

Introduction

1.1 MOTIVATION

Cancer is the second leading cause of death in the United States, after heart disease. It is estimated that 1,368,030 Americans will be diagnosed with cancer in 2004. As a result, more than 1,500 deaths a day will occur [3]. To date, the most effective treatment is based on the early detection of cancer and its precursors. Table 1.1 gives the five-year survival rates relative to a normal life expectancy for a variety of cancers initially detected in a local, regional, or distant state of development. Local staging is defined as an invasive malignant cancer confined entirely to the organ or origin. Regional staging is defined as a malignant cancer that 1.) has extended beyond the limits of the organ of origin directly into surrounding organs or tissues; 2.) involves regional lymph nodes by way of the lymphatic system; or 3.) has both regional extension and involvement of regional lymph nodes. Distant staging is defined as a malignant cancer that has spread to parts of the body remote from the primary tumor either by direct extension or by discontinuous metastasis to distant organs, tissues, or via the lymphatic system to distant lymph nodes [3]. In all cases shown in Figure 1.1, the five-year survival rate is greater for local staging than for all stages combined. In some cases such as oral cancer this difference is quite dramatic. Ideally, screening and detection would be sensitive to tissue changes that occur at the local staging of cancer. The high turn over rate of cells in epithelium makes it the most common site for cancer to emerge. Indeed, 85% of all cancers are epithelial in origin [10]. Some epithelial cancers include: cancer of the colon and rectum, esophageal cancer, bladder cancer, and oral cavity cancer. Development of highly selective and sensitive optical devices for the early detection of epithelial precancers has enormous potential to reduce patient morbidity and mortality. The focus of this dissertation is the early detection of precancerous and cancerous lesions in the oral cavity mucosa using a non-invasive fiber optic-based method.

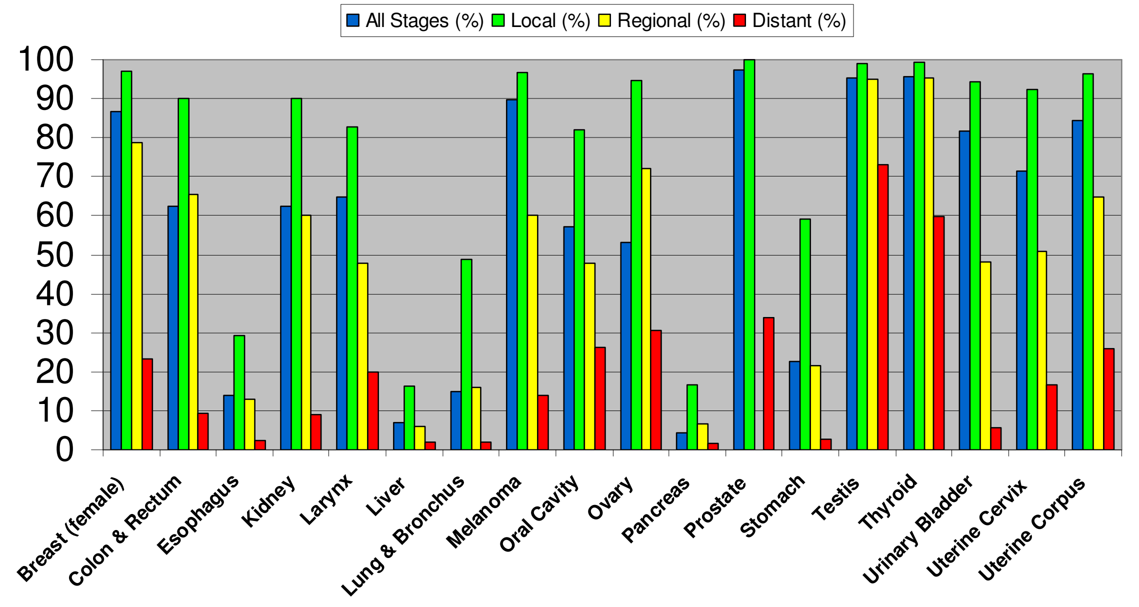

Figure 1.1: Five-year survival rates by stage at diagnosis, 1992-1999. Adapted from ref. [3].

1.2 SPECIFIC AIMS

The primary objective of my research was to assess the feasibility of using polarized reflectance spectroscopy for detection of morphologic changes associated with the early development of oral neoplasias for the ultimate purpose of improving early detection rates.

My specific goals were to:

1. Use tissue engineering methods to create tissue phantoms of epithelial tissue to better understand reflectance properties, beginning with simple polystyrene bead phantoms, and progressing to more complex and realistic tissue phantoms composed of cancer cells.
2. Test fiber optic probe design using tissue phantoms and biopsies, using results to develop and test mathematical algorithms to determine nuclear sizes. Compare the spectroscopically derived nuclear sizes with direct light microscopy measurements of *in vitro* samples. Test proper operation of equipment and fitting algorithm on normal volunteers at UT Austin.
3. Use equipment in a pilot clinical trial of 21 patients presenting precancerous or cancerous oral cavity lesions. Clinical trial is in collaboration with Dr. Ann Gillenwater at The University of Texas M.D. Anderson Cancer Center in Houston, Texas. For each eligible patient, Dr. Gillenwater performed standard white light examination of the oral mucosa. Then, the polarized reflectance spectra *in vivo* of one normal site and two-three abnormal sites in the oral cavity were taken. Biopsies were obtained from all measured sites, normal and abnormal.

4. Compare morphologic information including nuclear size obtained by the spectroscopic approach to quantitative histopathology. Quantitative histopathology is used as the gold standard to validate the approach based on polarized reflectance spectroscopy.
5. Use hyperspectral imaging system to further understanding of scattering properties of cancerous cells. Also obtain region-specific spectroscopic information of tissue slices.
6. Further refine the polarized reflectance spectroscopy system for detection and diagnosis of oral cavity lesions for use in underdeveloped countries.

1.3 DISSERTATION OVERVIEW

Chapter 2 gives background information on oral cavity cancer, oral cavity anatomy, scattering theory, and a review of recent literature. Chapter 3 presents the testing of the fiber optic probe and fitting algorithm in engineered tissue phantoms and in normal volunteers. Chapter 4 presents the results of the pilot clinical study. Finally, Chapter 5 provides a summary of results and suggests future directions for this project.

CHAPTER 2

Background

2.1 INTRODUCTION

Chapter 2 provides background information that will form the foundation for the rest of this dissertation. It is divided into five parts: 1.) motivation for studying oral cancer, 2.) anatomy of the oral cavity , 3.) pathology of the oral cavity, 4.) techniques for detection of oral precancer, 5.) optical spectroscopy and imaging.

2.2 MOTIVATION

Worldwide, oral cancer is a major health problem. In India it is the leading cancer in men [11], and it is the leading death due to cancer for women in Cuba [3]. Oral cancer is an epithelial cancer, which arises from genetic damage that accumulates over time with exposure to carcinogens [12]. Because of the rapid turnover rate of epithelial cells, these mutagenic changes can eventually progress to cancer. These mutations inevitably result in morphologic tissue changes indicative of precancer. Oral cancer is closely linked with tobacco usage and alcohol consumption [13]. Additional causative factors include nutritional deficiencies, poor dentition, genetic predispositions, and viruses such as the human papilloma and the herpes simplex viruses (HPV, HPS) [14, 15]. However, the greatest risk is from the synergistic effect of tobacco and alcohol. The

World Health Organization predicts increasing tobacco use over the next three decades with a corresponding increase in oral cancer cases.

In the U.S., it is estimated that there will be 28,260 new cases of oral cancer in 2004, resulting in 7,230 deaths [3]. The mortality rate for oral cancer is greater than that due to cutaneous melanoma or cervical cancer [12]. Despite years of research in cancer treatment, U.S. oral cancer survival rates have remained the same for approximately 30 years [16]. This plateau is largely due to the late staging of oral cancer when it is initially detected. It is often not found until it has become large and symptomatic, when cancer has progressed to a regional or distant stage of development, in which case treatment success is poor. The five-year survival rates for regional and distant staging are 47.9 % and 26.1 %, respectively. However, if caught early the five-year survival increases dramatically to 82.1 % [3].

Current screening methods are limited by the variety of the tissue architecture within the oral cavity and the numerous lesions that can appear at each site. Clinically, benign inflammatory conditions are difficult to visually distinguish from premalignant lesions. Microscopic inspection must be made using an invasive biopsy to discriminate benign from premalignant lesions. However, patients and clinicians are hesitant to have biopsies performed. Further, high risk patients have carcinogenic exposure from tobacco and/or alcohol that usually covers the entire mucosal lining. According to the theory of field cancerization, the entire mucosal lining is at risk for developing multiple lesions. Because the extent of genetic damage is not localized, even after successful treatment of a cancerous tumor, secondary tumors can develop in adjacent areas over time [17].

Monitoring of these high risk areas would require multiple biopsies over the entire oral cavity, taken routinely over many years. Clearly, noninvasive optical modalities to detect the early stages of oral cancer have the potential to greatly aid monitoring and diagnosing of premalignant lesions. Improved early detection will translate into reduced oral cancer mortality and morbidity.

2.3 ANATOMY OF THE ORAL CAVITY

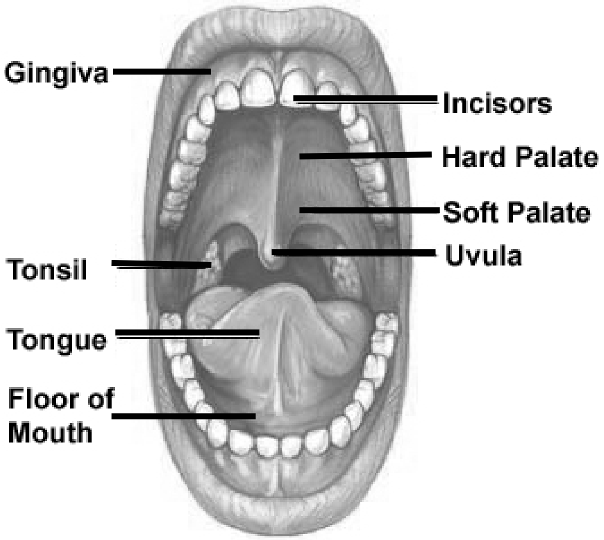

Figure 2.1: Major anatomical structures of the oral cavity. Modified from ref. [4].

The major anatomical structures within the oral cavity are shown in Figure 2.1. Areas that are most likely to develop cancer are indicated in Table 2.1. The tissue lining the oral cavity is classified as stratified squamous epithelium. Figure 2.2 (a) illustrates the basic architecture of stratified squamous epithelium. "Stratified" refers to the layers of cells stacked atop of the basement membrane, which separates the epithelium from the

General Location	Incidence	Specific Location
Tongue	26 %	• Lateral surface • Ventral posterior surface
Oral Pharynx	23 %	• Soft Palate • Tonsillar pillars
Lip	20 %	• Vermillion surface
Floor of Mouth	17 %	• Floor of mouth
Gingiva	9 %	• Gingiva
Buccal Mucosa	3 %	• Buccal mucosa (cheek)
Hard Palate	2 %	• Hard palate

Table 2.1: Incidence of squamous cell carcinoma by location. Modified from ref. [1].

submucosa. Germinative cells immediately above the basement membrane are responsible for new cell growth.

Cell growth proliferates upward from the germinative layer toward the tissue surface. Typically, the outer cells of oral epithelium are sloughed off and regenerated every 3 – 7 days. “Squamous” refers to the thin, flat shape these cells take at the tissue surface. The main function of stratified squamous epithelium is to offer protection against mechanical and chemical stresses. Areas exposed to severe abrasions, such as masticatory mucosa, develop a top layer of keratin as shown in Figure 2.2 (b).

The tissue directly below the basement membrane is called the lamina propria or stroma. It is connective tissue comprised primarily of fibrous proteins such as collagen. In this region nutrients are delivered via capillaries. Diffusion of these nutrients through the basement membrane supplies the epithelium. Recently, evidence has been gathered indicating that there are concomitant chemical and morphological changes that occur in the stroma with epithelial dysplasia [18-20].

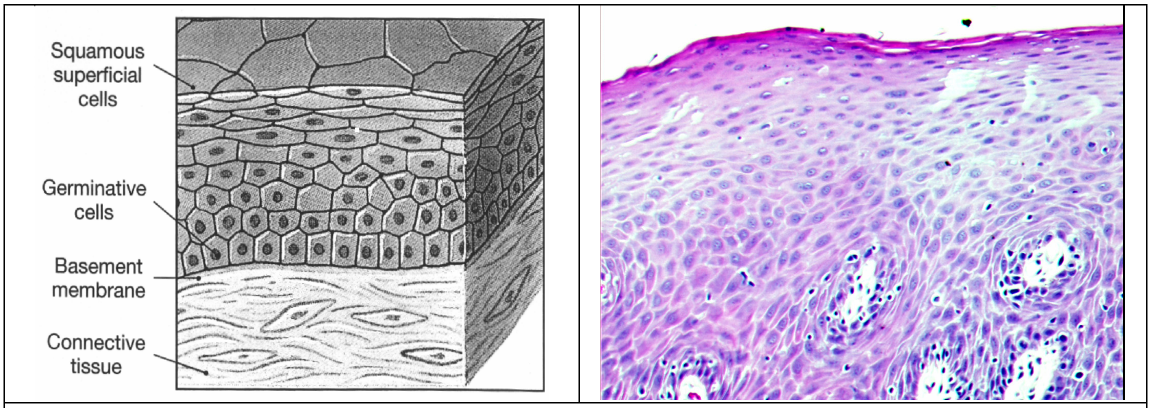

Figure 2.2: (a) Illustration of the basic architecture of stratified squamous epithelium. Modified from ref. [5]. (b) H&E (hematoxylin and eosin) section of buccal mucosa that has been exposed to severe abrasion, causing a thin layer of keratin (dark pink) to form at tissue surface.

2.4 PATHOLOGY OF THE ORAL CAVITY

By far the most common type of oral cancer is squamous cell carcinoma (SCC). Nine out of 10 oral malignancies are SCC [15]. Therefore, this dissertation concentrates on the early detection of this predominate oral cancer. Some of the difficulties that arise in diagnosing oral cancer are due to the variety of appearances of precancer and SCC. There is no standard clinical appearance of SCC, so clinicians must biopsy a lesion to rule out cancer regardless of appearance. In this section I will describe common oral cavity lesions, some of which may develop into cancer.

The clinical appearance of most lesions in the oral cavity can be divided into three categories: 1.) white patch, 2.) red patch, 3.) speckled. All three types of lesions have the potential to progress to cancer. As a result, histopathologic examination must be preformed to exclude malignancy. Figure 2.3 illustrates the progression of normal tissue to mild dysplasia, moderate-severe dysplasia, carcinoma-in-situ, and finally to invasive carcinoma.

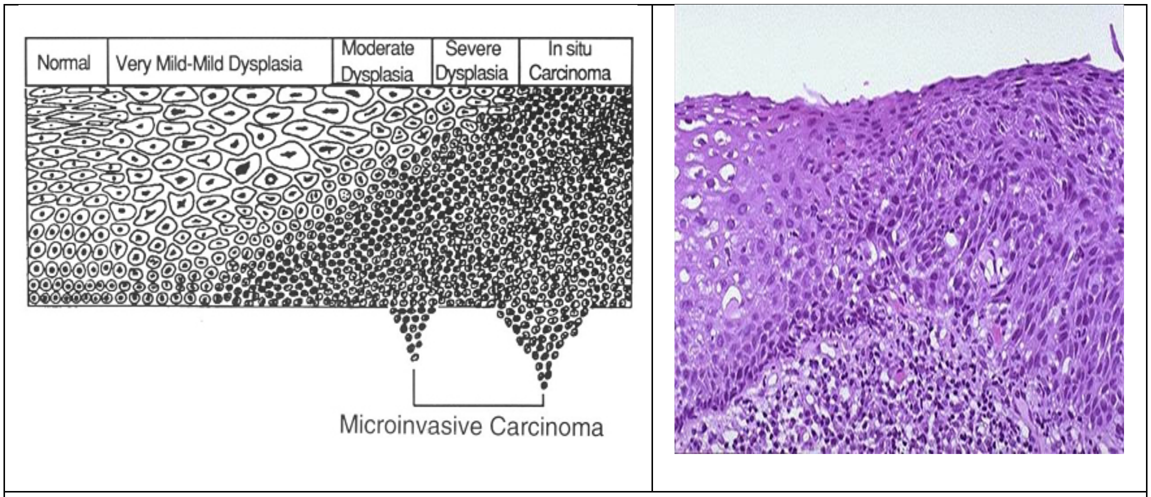

Figure 2.3: Step-wise progression of normal stratified epithelial tissue toward cancer. (a) Illustration. (b) H&E section of epithelium with carcinoma-in-situ on right side.

This progression toward cancer is marked by morphologic changes such as increased nuclear size, increased nuclear size distribution, increased nuclear to cytoplasmic ratio, increased mitotic processes, hyperchromasia, and pleomorphism. A proliferation of cells within the basal layer signals the first step toward malignant transformation. When cell proliferation is less than one third of the epithelium thickness, it is diagnosed as mild dysplasia. Proliferation that includes two thirds of the epithelium is termed moderate-severe dysplasia. Dysplasia that encompasses the full thickness of the epithelium is called carcinoma-in-situ. At this stage, the uncontrolled growth of epithelial cells has not yet penetrated through the basement membrane. Anaplasia, which is the hallmark of malignant transformation, may be present at this stage. It is identified by the loss of differentiation and polarity of cells, causing the tissue architecture to become disorganized and “restless”. Invasion of anaplastic cells through the basement membrane is given the diagnosis of invasive carcinoma. Cells that have broken through the basement membrane are free to infiltrate capillaries and lymph ducts to form distant metastasizes [10].

2.4.1 White Lesions

Most lesions in the oral cavity have the appearance of white patches or “leukoplakia” that cannot be scraped from the mucosal surface and cannot be classified clinically as any other disease. 85 % of precancerous lesions have the clinical appearance of leukoplakia [21]. Figure 2.4 (a) shows an example of leukoplakia of the lateral tongue.

Frequently, leukoplakia is “benign keratosis,” which is due to chronic irritation. The epithelium responds by producing keratin (keratosis), see Figure 2.4 (b), and also thickening the epithelium (acanthosis) [1]. Proliferation of a keratin layer at the surface of epithelium is called “hyperkeratosis.” As its name implies, this malady is benign and can be disappear with removal of the causative irritant.

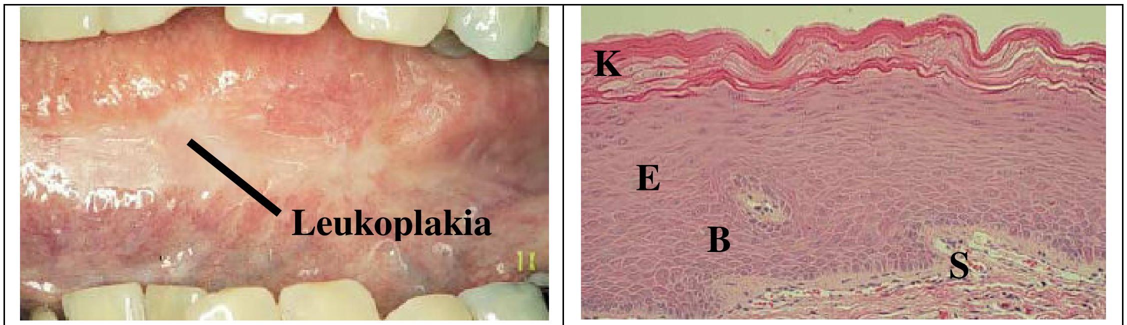

(a) (b)

Figure 2.4: Example of leukoplakia. (a) Clinical appearance of diffuse, homogeneous leukoplakia of the lateral tongue. (b) Histology of leukoplakia revealed benign keratosis. K = keratin, E = epithelium, B = basement membrane, S = stroma. Images modified from ref. [6].

In two studies by Silverman [22, 23], leukoplakia underwent malignant transformation in 6.0 % of 117 cases, and 17.5 % of 257 cases over a mean observation period of 3.5 and 7.2 years, respectively. In the Silverman studies, the rate of transformation increased with time. This conforms with the time evolution of a multi-step development of SCC. This is further supported by the fact that approximately 95 % of SCC occurs in individuals aged 40 years or older.

Another white patch lesion is “lichen planus.” It is mentioned here because it is indistinguishable from leukoplakia. It is a chronic inflammatory disease. Etiology is unknown but it is thought to be an autoimmune disease [15]. Figure 2.5 illustrates the clinical difficulty in diagnosing lesions without biopsy.

Figure 2.5: Lichen planus of the dorsal tongue. Reprinted from ref. [7].

2.4.2 Red and Speckled Lesions

The next clinical category includes lesions that have the appearance of a red patch or "erythroplakia." This type of lesion is nearly always associated with dysplasia or carcinoma at the time of clinical identification [12]. Mixtures of red and white patches, or speckled lesions, are at a higher risk for malignancy compared to leukoplakia alone. Speckled lesions, also called "erythroleukoplakia," have a transformation rate of 23.4 % compared to 6.5 % for homogeneous leukoplakia [15]. Figure 2.6 shows an image of erythroplakia and a speckled lesion.

Table 2.2 summaries the precancerous and cancerous lesions along with their appearance, both clinical and histological.

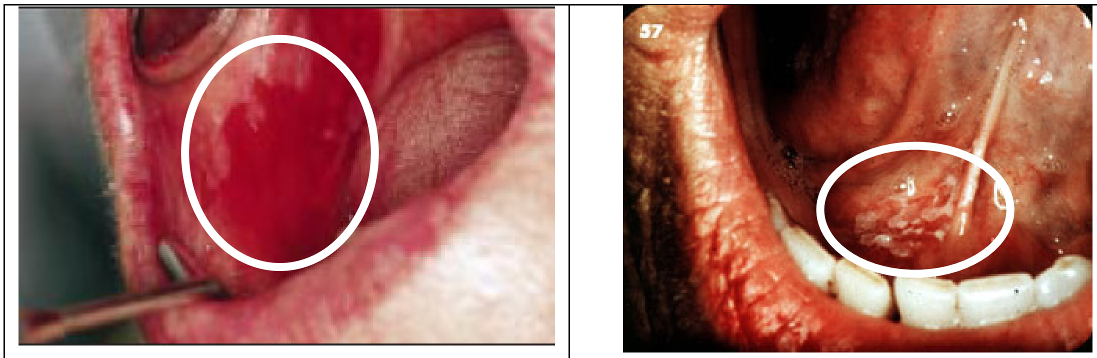

(a) (b)

Figure 2.6: Examples of red lesions. (a) Erythroplakia of the right buccal mucosa. Modified from ref. [7]. (b) Image of a speckled lesion in the floor of the mouth. Modified from ref. [1].

Feature	**Benign Keratosis**	**Mucosal Dysplasia**	**Carcinoma-in-Situ**	**Invasive Squamous Cell Carcinoma**
Etiology	• Chronic trauma • Alcohol • Tobacco	• Chronic trauma • Alcohol • Tobacco	• Chronic trauma • Alcohol • Tobacco	• Chronic trauma • Alcohol • Tobacco
Clinical Features	• White patch	• White patch • Red patch • Speckled patch	• White patch • Red patch • Speckled patch	• White patch • Red patch • Speckled patch
Histopathological Features	• Hyperkeratosis only	• Dysplasia	• Anaplasia	• Invasive squamous cell carcinoma
Treatment	• Elimination of etiology	• Surgical excision • Elimination of etiology	• Surgical excision • Elimination of etiology	• Surgical excision • Radiation
Prognosis	• Excellent	• Excellent	• Good	• Poor

Table 2.2: Precancerous and cancerous lesions of the oral cavity. Modified from ref. [1].

2.5 TECHNIQUES FOR DETECTING ORAL PRECANCER

As the previous sections revealed, many benign lesions have the same or similar appearance as precancerous or cancerous lesions. For example, invasive cancer can appear the same as benign keratosis or mucosal dysplasia. Clearly, methods that can discriminate cancer from benign conditions are needed. In this section, I will give a review of current techniques for screening and detection of oral cancer.

2.5.1 Clinical Observation and Biopsy

Oral cancer is typically found during a dental check-up, or during a routine physical examination [24]. The clinician visually assesses the oral cavity, considering the patient history as to whether a biopsy is required. Microscopic histologic examination of biopsied tissue by a trained pathologist remains the best method for accurate diagnosis. As such it is the gold standard by which all emerging methods are compared.

2.5.2 Toluidine Blue Dye

If after an examination, a clinician determines that a biopsy is needed, a problem can arise as to where the biopsy should be taken. This is a particular dilemma for cases in which the lesion is large (greater than 4 mm), or covers a large extent of the oral mucosa. Where is the optimum, or most abnormal tissue site that should be biopsied? Toluidine blue (TB) dye is a vital stain that can be used to help identify areas with the high grade dysplasia or cancer. A 1 % solution of toluidine blue dye is applied to suspicious areas, followed by a water rinse. A solution of 1 % acetic acid is then applied, followed by a water rinse. The exact mechanism for staining is unknown, but it is believed to be related to the dye's binding affinity to nucleic acids and/or sulfated mucopolysaccharides, both of which are selectively high in dysplastic and malignant tissue [15].

In a recent small study, the sensitivity and specificity of toluidine blue staining was evaluated. Sensitivity is the probability that the test is positive, given that the patient has disease. Specificity is the probability that the test is negative, given that the patient has no disease. TB was found to have a sensitivity of 100 % for the 18 oral cancers studied, and 78 % for 39 oral epithelial dysplasias. The specificity of TB to precancer, however, was found to be only 62.5 % [25]. It remains to be seen if this technique would significantly add to current screening methods.

2.5.3 Brush Biopsy

Another moderately noninvasive technique that can be used as an adjunct to biopsy is a variation of exfoliative cytology. This technique is very similar to the Papanicolaou (Pap) smear. A brush is used to exfoliate the full thickness of the epithelium of a suspicious lesion. The cells on the brush are then transferred onto a microscope slide and fixed. A neural network computer algorithm is used to select cells that are suspicious for precancer or cancer [26]. A pathologist reviews the highlighted cells, then makes the final diagnosis. This technique has 100 % sensitivity and is very useful for cases when the lesion is localized. However, when a lesion or multiple lesions covers a large portion of the oral cavity, this method is not feasible. Additionally, scraping away the full thickness of epithelium is painful, and may be difficult for cases where a thick keratin layer has formed.

2.6 OPTICAL SPECTROSCOPY AND IMAGING

A purely non-invasive, painless technique that is being developed is optical spectroscopy and imaging. It has the potential to bridge the gap between clinical examination and biopsy by providing quantitative information on the biochemical and morphological changes associated with precancer. These biological changes perturb the interaction of light with tissue, which can be monitored using optical methods. Specifically, biochemical changes can be monitored with fluorescence, while morphological changes can be monitored with reflectance. As this dissertation is focused on optical techniques, I will detail the basic physical principles of fluorescence and reflectance, and discuss their application to the oral cavity.

2.6.1 Fluorescence

Fluorescence results from a radiative decay of an electron that has been excited from the ground state, S0, by absorption of a photon. Fluorescence is the radiative decay of the electron from the excited singlet state, S1. Figure 2.7 is a Jablonski diagram of fluorescence.

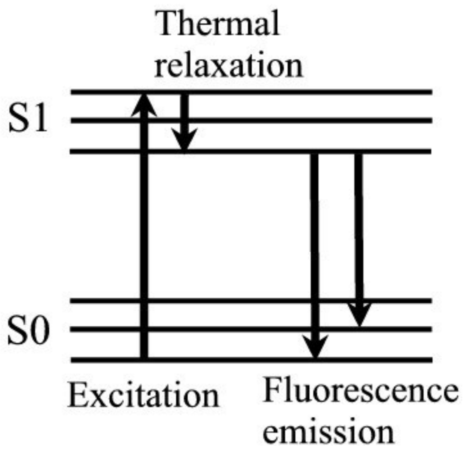

Figure 2.7: Jablonski diagram of fluorescence. Energy levels are indicated by horizontal lines.

The excited electron has a spin with the opposition orientation relative to an electron in the ground state. Typically, the lifetime of fluorescence, or the time that an electron spends in an excited state, is on the order of tens of nanoseconds. During relaxation, the conservation of angular momentum is satisfied by a release of a photon, which has an angular momentum equal to one. The emitted photon will have less energy than the incident absorbed photon. As a result, the emission photon will have a longer wavelength than the excitation photon. This is called a “Stokes shift.” Generally, Stokes shifts are on the order of 50-100 nm from the excitation wavelength. Some common fluorophores found within tissue are listed in Table 2.3.

Fluorophores	**Excitation Maxima (nm)**	**Emission Maxima (nm)**
NADH	290, 340	440, 450
FAD	450	515
Collagen cross-links	325	400
Elastin cross-links	325	400
Collagen powder	280, 265, 330, 450	310, 385, 390, 530
Elastin powder	350, 410, 450	420, 500, 520
Tryptophan	280	350

Table 2.3: Endogenous tissue fluorophores. Adapted from ref. [2].

The contribution from the various intrinsic oral epithelial fluorophores varies according to disease. The fluorescence spectra (wavelength dependence of intensity) within oral cavity tissue has been studied [27-29] and the results applied to vision enhancement of premalignant and malignant *ex vivo* oral mucosa tissue [30]. The best sensitivity and specificity was 91 % and 86 %, respectively, for 400 nm excitation. This is better than the standard white light examination of the same excised tissue, which had a sensitivity and specificity of 75 % and 43 %. The sensitivity and specificity of *in vivo* white light examination of oral mucosa lesions has been reported to be 74 % and 99 %, respectively [31]. More work needs to done in this area to assess the feasibility of fluorescence vision enhancement with respect to *in vivo* tissue. Nevertheless, these results are encouraging. Vision enhancement can be used to direct biopsies and compliment high resolution optical imaging instruments that probe tissue morphology, such as optical coherence tomography (OCT), optical coherence microscopy (OCM), or confocal microscopy. These high resolution instruments probe the scattering properties of tissue using a monochromatic source. The scattering signal is commonly called the reflectance. This is a bit of a misnomer, as reflectance usually brings to mind the specular reflection off a smooth surface. In this dissertation, reflectance will refer to light that is remitted from tissue after some number of scattering interactions.

2.6.2 Reflectance

In clinical biomedical engineering, the term "reflectance" is used to describe light that is scattered or "reflected" back toward the detector after it has interacted with tissue, as shown in Figure 2.8.

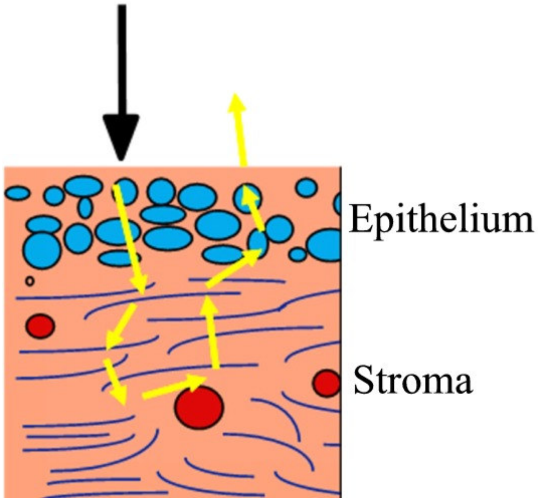

Figure 2.8: Interaction of light with tissue. The black arrow represents incident light. Yellow arrows represent light that is scattered and remitted from tissue.

Photons that penetrate into tissue can undergo elastic scattering and/or absorption events. Within mucosal tissue, cell nuclei are the major scatterers, and blood is the major absorber in the visible wavelength range (400-700 nm). Although less frequently encountered, light can also be absorbed by melanin found in pigmented lesions. In the upper epithelial layer, hemoglobin is not present, so scattering dominates. In the stroma where capillaries are present, absorption modulates the reflectance signal.

The elastic scattering of light from tissue can provide information on the cellular morphology of tissue. It has been demonstrated that the wavelength dependence of elastically scattered photons is sensitive to nuclear size [32-39], and subcellular structures [33, 34, 40-42]. A major prognostic indicator of disease is nuclear size. Obtaining nuclear sizes non-invasively with reflectance spectroscopy can be applied as a diagnostic aid for the early clinical diagnosis of precancerous changes [2, 43-45].

Fluorescence and reflectance spectroscopy are complimentary approaches probing concomitant biochemical and morphological changes with precancer, where reflectance is used to provide tissue morphology information, and fluorescence is used to give biochemical information.

The high resolution devices based on fluorescence or reflectance provide imaging resolution fine enough to resolve cellular and subcellular structures such as cell nuclei. These techniques are limited by their signal to noise and also by their physical size, making it difficult to measure organ sites that are not obviously accessible, such as the skin. Currently, much work is being done in this area to increase signal to noise and to miniaturize the optical components [46, 47].

Spectroscopic methods can be applied to accessible and relatively inaccessible organ sites owing to the ease with which they can be adapted to endoscopic configurations. Comparatively speaking, spectroscopic designs are lower in cost than imaging devices, making them clinically more appealing. Endoscopic spectroscopy is also capable of monitoring large lesions by obtaining many point measurements throughout the lesion or organ site. Fluorescence spectroscopy has been studied extensively in the cervix, colon, bronchus, and bladder [48]. Encouraging studies in the area of reflectance for diagnosing precancer has also been performed [29, 49-51]. This dissertation will focus on reflectance spectroscopy as a non-invasive precancer indicator.

2.6.3 Polarized Reflectance Spectroscopy

Diffuse reflectance from tissue is comprised primarily of two parts: singly scattered photons, and multiply scattered photons. Photons that undergo single scattering events are limited to the epithelial layer of tissue. It has been demonstrated that the singly scattered intensity contributes to approximately 5 % or less of the total detected reflectance spectrum [52]. The majority of the reflectance signal arises from multiply scattered photons that travel deeper into tissue. These photons carry information on both the epithelium and stroma. Since multiply scattered photons are able to reach the stroma, they are likely to interact with capillaries present there, resulting in the reflectance intensity spectrum to be modulated by hemoglobin absorption. Disentangling the effects of scattering and absorption in a turbid medium is a difficult problem. However, the singly scattered signal is unencumbered by absorption, so a more tractable problem is the isolation of this small signal from the diffusive multiply scattered background. The singly scattered signal has the added benefit of being localized to the region where precancerous changes are well documented to begin - the epithelial layer.

Polarized illumination and detection of broadband visible light from tissue has been employed by several groups to isolate the singly scattered component of the reflectance intensity signal [36, 37, 53-56]. The idea behind this technique is quite simple: the electric field vector orientation of a photon, or polarization, is randomized after many scattering events, whereas it remains virtually unchanged after a single scattering event. Figure 2.9 illustrates the general concept.

Using a linear polarizer, the incident beam can be given the desired electric field orientation. An analyzer placed before a detector allows selective detection of the spectral intensity with polarization parallel, $I_{//}(\lambda)$, and orthogonal, $I_{\perp}(\lambda)$, to the incident beam. The definition of unpolarized light requires that the multiply scattered intensity to be comprised of equal parts of parallel and perpendicular polarizations. So, the measured intensity with polarization parallel to the incident beam is given by:

$$I_{//}(\lambda) = 0.5\, I_{MS}(\lambda) + I_{SS}(\lambda) \tag{2.1}$$

where $I_{MS}(\lambda)$ is the intensity of multiply scattered light, and $I_{SS}(\lambda)$ is the intensity of singly scattered light.

Similarly, the measured perpendicular intensity can be written as:

$$I_{\perp}(\lambda) = 0.5\, I_{MS}(\lambda) \tag{2.2}$$

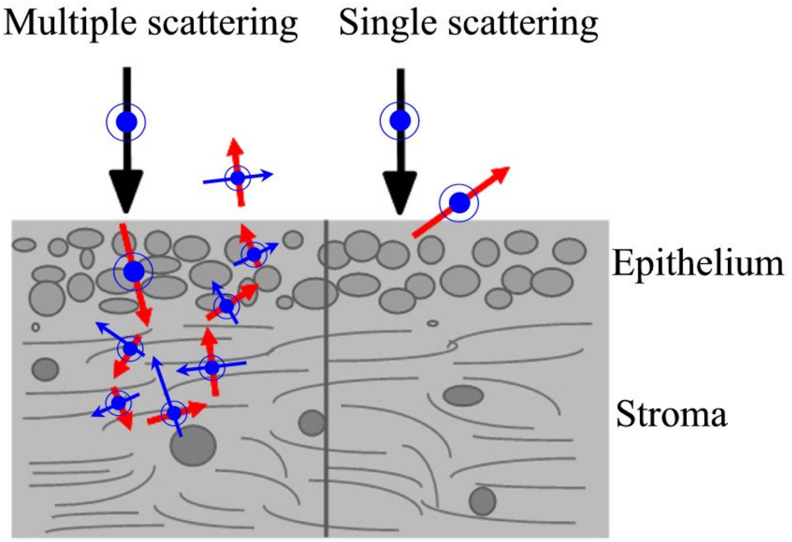

Figure 2.9: Illustration of the scattering of polarized light in tissue. The black arrows indicate the propagation direction of an incident photon, the red arrows indicate the propagation direction of the scattered photon, and the blue circle/arrows indicate the electric field vector orientation. On the left, the depolarization of an incident polarized photon after many scattering events is shown. The right side illustrates the retention of the original incident polarization after a single scattering event.

Subtracting the perpendicular component of the detect intensity from the parallel eliminates the diffusive multiply scattered background and the corresponding modulation due to hemoglobin absorption. Now we can define the depolarization ratio:

$$D(\lambda) = \frac{I_{\parallel}^{(t)}(\lambda) - I_{\perp}^{(t)}(\lambda)}{I_{\parallel}^{(s)}(\lambda) + I_{\perp}^{(s)}(\lambda)} = \frac{(I_{SS} + 0.5I_{MS}) - 0.5I_{MS}}{I_{SS} + I_{MS}} \tag{2.3}$$

where I_{SS} is the intensity due to singly scattered photons, and I_{MS} is the intensity of light due to multiply scattered photons, $I_{\parallel}^{(t)}(\lambda)$ and $I_{\perp}^{(t)}(\lambda)$ are the detected scattering intensity from tissue with polarizations parallel and perpendicular relative to the incident beam, and $I_{\parallel}^{(s)}(\lambda)+I_{\perp}^{(s)}(\lambda)$ is the total (parallel plus perpendicular) scattered light collected from a diffusely scattering substrate. The denominator is a normalization factor that accounts for the spectral characteristics of the lamp, and detection optics. The depolarization ratio can be assumed to be a measure of singly scattered photons, and therefore an indicator for early precancerous changes that occur in the epithelium.

2.7 APPROACHES TO MODELING ELASTIC SCATTERING

Three common approaches that are used to describe the interaction of light with tissue are radiative transfer theory (RTT), Monte Carlo (MC) modeling, and Mie theory. The first two approaches are heuristic in nature, treating the propagation of light as a flow of discrete photons in a medium containing scattering and absorbing particles. The third approach is derived analytically from Maxwell's equations, in which light is treated as an electromagnetic wave traveling through a spatially and temporally varying dielectric medium.

2.7.1 Radiative Transfer Theory

RTT is an empirical approach that has been developed largely without reference to electromagnetic theory. It is based on the transfer of energy through a turbid medium. RTT does not include the effects of interference or diffraction and assumes no correlation between radiation fields. Therefore, intensities rather than amplitudes are measured. This reflects the empirical nature of RTT where the desired formulas relate to measurable quantities, such as power and intensity. The stationary form of the RTT equation can be expressed as follows: [57-59]

$$\hat{s}\cdot\nabla I(\vec{r},\hat{s})+\mu_t(\vec{r})I(\vec{r},\hat{s})=\mu_s(\vec{r})\int_{4\pi}p(\hat{s},\hat{s}')I(\vec{r},\hat{s}')d\vec{\omega}'+S(\vec{r},\hat{s}) \qquad (2.4)$$

where I is the radiance [W/(m^2·sr)], μ_t is the total extinction coefficient [1/m], μ_s is the scattering coefficient [1/m], p is the scattering phase function [1/sr], and S is the source term that corresponds to the power generated at $\vec{r}$ in $\hat{s}$ direction [W/(m^3·sr)]. Detailed descriptions of these components are given in the following sections. A general solution of this equation for tissue is not available. Approximate yet descriptive solutions can be found, as in the case of diffuse scattering. Numerical techniques are also employed to approximate solutions. The next section details a robust computational technique called Monte Carlo modeling.

2.7.2 Monte Carlo

Monte Carlo method is a rigorous statistical approach where light is described semi-classically as photon particles. In this approach, the "random walk" of photons through tissue is simulated. It is less computationally intensive than full Maxwell representations, and it is able to adequately model light scattering from tissue. As a result, MC has been used extensively in biomedical applications to describe light-tissue interactions.

The two key parameters in MC are the scattering angle, and the mean free path for a photon-tissue interaction. The mean free path for a single scattering event is given by the reciprocal of the scattering coefficient, μ_s. Classically, the scattering coefficient can be written in terms of the effective cross-sectional area, σ_s:

$$\mu_s = \rho_s \sigma_s \tag{2.5}$$

where ρ_s is the volume density [cm^{-3}], and σ_s is the effective cross-sectional area [cm^2]. The relationship between the geometrical area of a spherical scatterer and the effective cross-sectional area is shown in Figure 2.10. Depending on the dielectric properties of the sphere, the effective cross-sectional area may be larger or smaller than the geometrical shadow cast by the sphere.

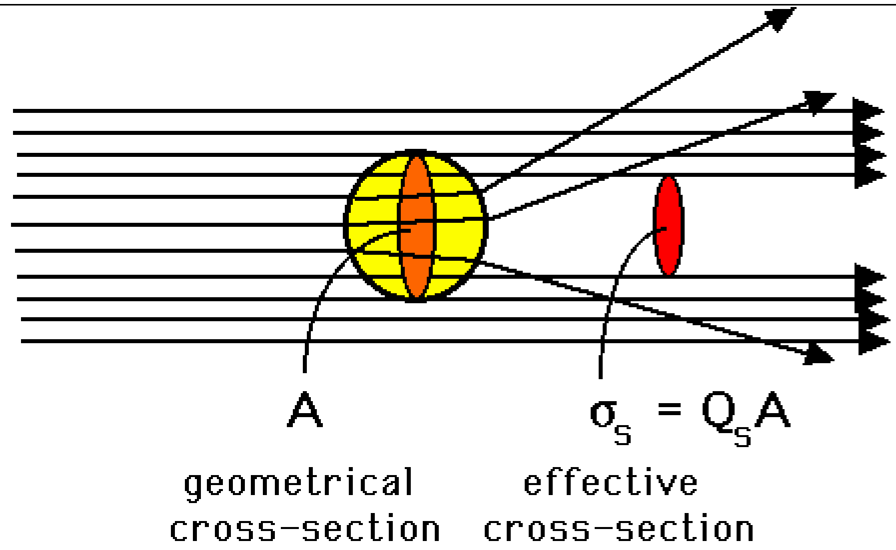

Figure 2.10: Illustration of scattering by a single sphere. The geometrical cross-sectional area is given by A, the effective cross-section by σs, the efficiency of scattering by Qs. The effective cross-section can be greater or less than the geometrical shadow cast by the sphere, depending on its dielectric properties. Adapted from ref. [8].

If the medium is absorbing, the mean free path for interaction is defined by the reciprocal of the total attenuation coefficient, μ_t. The attenuation coefficient can be represented by the sum of the scattering coefficient, μ_s, and the absorption coefficient, μ_a:

$$\mu_t = \mu_s + \mu_a \tag{2.6}$$

The scattering angle, or deflection angle, is defined as the angle between incident photon direct, $\hat{s}'$, and the scattered photon direction, $\hat{s}$. Figure 2.11 illustrates the basic geometry for a single photon scattering event. The angular coordinates are given by the deflection angle, θ, and the azimuthal angle, φ.

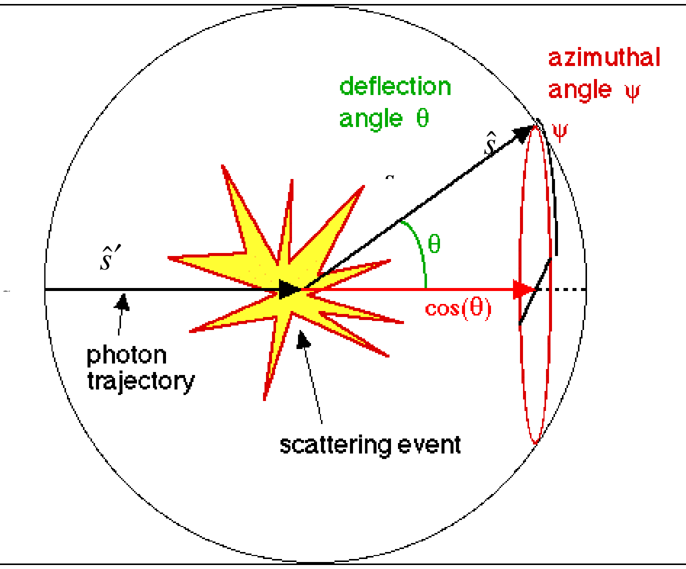

Figure 2.11: Deflection of a photon after a single scattering event. θ is the scattering angle, and φ is the azimuthal angle. Modified from ref. [8].

In MC, the parameters of mean free path and scattering angle are described with probability distribution functions. In this formalism, the scattering and absorption coefficients are defined by their probabilities for scattering and absorption, respectively.

For example, the probability for scattering in an infinitesimal distance ds is given by $\mu_s ds$. Similarly, the probability for absorption in an infinitesimal distance ds is given by $\mu_a ds$.

The probability density function for the mean free path is given by:

$$p(s) = \mu_t \exp(-\mu_t s) \tag{2.7}$$

where *s* is distance. This density function describes the probability associated with each possible value of *s*. The probability that *s* will be in an interval $[a,s_1]$ is given by the area under the curve of *p(s),* otherwise known as the probability distribution function for the mean free path:

$$F(a \le s_1) = \int_a^{s_1} p(s)ds \tag{2.8}$$

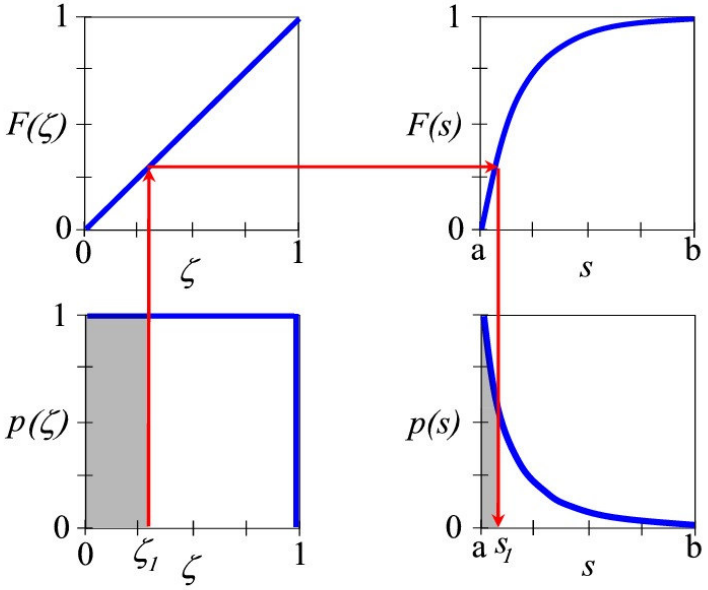

Figure 2.12: Diagram for mapping a random number, ζ_1, onto the mean free path probability density function, *p(s)*.

Ultimately, we want to sample the probability density function using computer generated random numbers, ζ, uniformly distributed and bounded by [0,1]. Figure 2.12 illustrates the mapping from random numbers to the mean free path probability density function that we want to achieve.

As can be seen in Figure 2.12 the probability density function for uniformly generated random numbers is a constant equal to one. The corresponding probability distribution function can then be written:

$$F(\zeta_1) = \int_0^{\zeta_1} p(\zeta)d\zeta = \zeta_1 \tag{2.9}$$

The randomly generated numbers, ζ, can now be mapped to the probability distribution function for mean free path as follows:

$$\zeta = F(s) \tag{2.10}$$

$$s = F^{-1}(\zeta) \tag{2.11}$$

Substituting equations (2.7) and (2.8) into the above equation yields the mean free path or step size used to propagate photons through tissue in MC:

$$s = \frac{-\ln(\zeta)}{\mu_t}, \qquad \zeta \in [0,1] \tag{2.12}$$

Propagation of a photon through tissue also requires that the probability density function for the scattering angle be determined. In a similar manner as above, random numbers are used to sample the probability density function for the scattering angle, also known as the scattering phase function, $p(\cos\theta)$. The scattering function describes the angular distribution of scattering from unit direction s' to unit direction s.

In tissue, scattering is not isotropic, but highly forward directed. Consequently, the scattering angle probability density function is not uniform. Henyey and Greenstein proposed a scattering phase function that approximates Mie scattering from particles that are comparable in size to the wavelengths of light. Their function is used extensively in biomedical optics to approximate the scattering phase function in tissue:

$$p(\cos\theta) = \frac{1-g^2}{2(1+g^2-2g\cos\theta)^{3/2}} \tag{2.13}$$

where *g*, the anisotropy factor, is the average cosine of the scattering angle.

We want to sample this function using random numbers, as we did before for the mean free path. So, we can write the angular probability distribution function as follows:

$$F(p(\cos\theta)) = \int_{-1}^{\cos(\theta)} p(\cos(\theta))d(\cos(\theta)) = \zeta \tag{2.14}$$

For the sake of convenience, everything is written in terms of *cos*(*θ*), such that it is bounded by [-1, 1]. We can now write the scattering angle to propagate photons after a scattering event in terms of randomly generated numbers:

$$\begin{aligned} \cos\theta &= \frac{1}{2g}\left[1+g^2-\left(\frac{1-g^2}{1-g+2g\zeta}\right)^2\right] \qquad &, g \neq 0 \\ \cos\theta &= 2\zeta - 1 \qquad &, g = 0 \end{aligned} \tag{2.15}$$

Given equations (2.12) and (2.15), MC can model light propagation in tissue by incrementally propagating a statistically large number of photons through a 3D grid of tissue. The refractive index *n,* and μ_s, μ_a, and *p* are specified at each grid location. After each interaction event, a new mean free path, scattering and azimuthal angles, and photon weight are updated.

In chapter 4, a three dimensional MC is used to model carcinogenesis in a two layer tissue. The MC results are compared with results of a pilot clinical trial. For a more detailed overview of the Monte Carlo method in modeling light scattered in tissue, the reader is referred to ref. [59].

2.7.3 Mie Theory

Mie theory is an exact analytical solution to Maxwell's equations for the case of spherical scatterers of arbitrary size and homogenous index of refraction. The sensitivity of the wavelength dependence of the forward and backward Mie scattering intensities to nuclear size and size distribution can be exploited to elucidate cellular morphology. Therefore, I will briefly overview the solution to Maxwell's equations that give Mie theory.

Consider a plane monochromatic wave in vacuum, impinging on a spherical particle of radius, *a*, and homogenous refractive index, n. Figure 2.13 diagrams the scattering geometry. Maxwell's equations for this case are:

$$\begin{aligned}
\vec{\nabla} \bullet \vec{E} &= 0 \\
\vec{\nabla} \bullet \vec{B} &= 0 \\
\vec{\nabla} \times \vec{E} &= i\omega\mu\vec{H} \\
\vec{\nabla} \times \vec{H} &= -i\omega\mu\vec{E}
\end{aligned} \tag{2.16}$$

where $\vec{E}$ is the electric field vector, $\vec{H}$ is the magnetic field vector, $i = \sqrt{-1}$, ω is the angular frequency, μ is the permeability, and ε is the permittivity.

At the boundary of the sphere we impose the condition that the tangential components of $\vec{E}$ and $\vec{B}$ be continuous:

$$\left(\vec{E}_i + \vec{E}_s - \vec{E}_1\right) \times \hat{r} = \left(\vec{H}_i + \vec{H}_s - \vec{H}_1\right) \times \hat{r} = 0 \tag{2.17}$$

where the subscript *(i)* denotes the incident field, *(s)* the scattered field, *(1)* the field inside the sphere, and $\hat{r}$ is a unit vector in the radial direction.

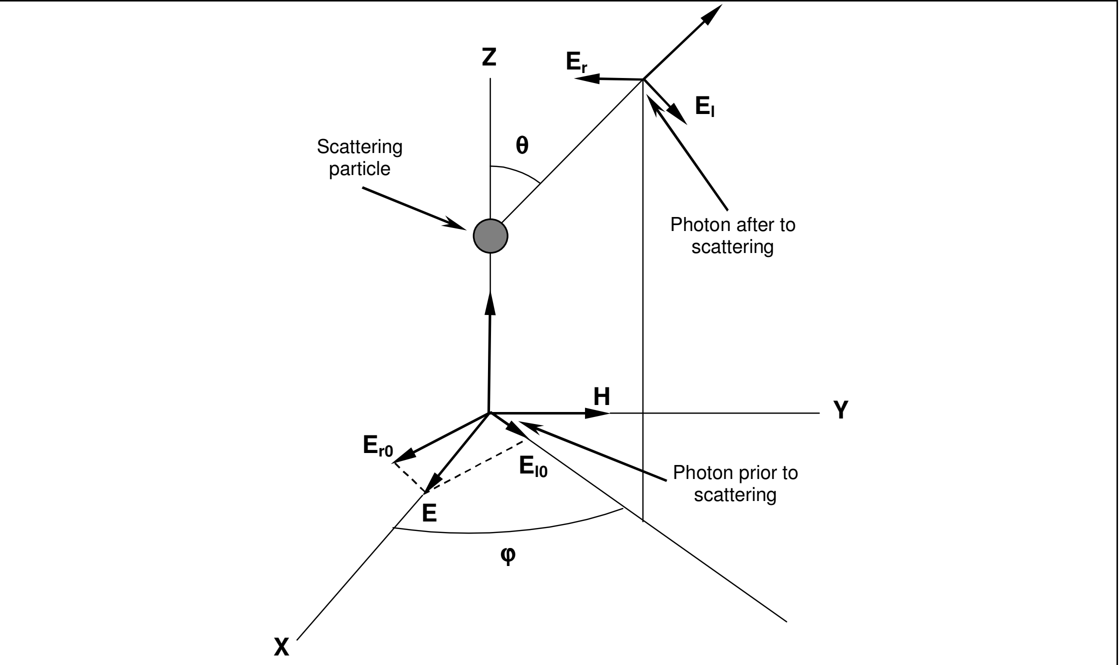

Figure 2.13: Geometry for scattering of a plane monochromatic wave from a spherical particle. The scattering plane is defined by the propagation vectors of the incident and scattered wave.

Using Maxwell's equations and the boundary condition at the surface of the sphere, the scattered electric field can be written as an infinite sum of vector spherical harmonics, $M_{01n}^{(3)}$ and $N_{e1n}^{(3)}$:

$$
\begin{aligned}
&\vec{E}_s = \sum_{n=1}^{\infty} \vec{E}_n (i a_n N_{e1n}^{(3)} - b_n M_{01n}^{(3)}) \\
&M_{01n}^{(3)} = \cos\varphi \frac{P_n^1(\cos\theta)}{\sin\theta} h_n^{(1)}(kr)\hat{\theta} - \sin\varphi \frac{dP_n^1(\cos\theta)}{d\theta} h_n^{(1)}(kr)\hat{\varphi} \\
&N_{e1n}^{(3)} = \cos\varphi n(n+1)\sin\theta \frac{P_n^1(\cos\theta)}{\sin\theta} \frac{h_n^{(1)}(kr)}{kr}\hat{r} + \cos\varphi \frac{dP_n^1(\cos\theta)}{d\theta} \frac{\left[krh_n^{(1)}(kr)\right]'}{kr}\hat{\theta} \\
&- \sin\varphi \frac{P_n^1(\cos\theta)}{\sin\theta} \frac{\left[krh_n^{(1)}(kr)\right]'}{kr}\hat{\varphi} \\
&k = \frac{n_{medium} 2\pi}{\lambda}
\end{aligned}
\tag{2.18}
$$

where a_n and b_n are the scattering coefficients, and $M_{01n}^{(3)}$ and $N_{e1n}^{(3)}$ are written in terms of the scattering angles θ and φ, Legendre polynomials $P_n^1(\cos\theta)$, and spherical Hankel functions $h_n^{(1)}(kr)$; n_{medium} is the refractive index of the medium, and λ is the wavelength. Equation (2.18) tells us that, in general, the scattered field is a superposition of the normal modes of the particle given by the spherical harmonic functions, $M_{01n}^{(3)}$ and $N_{e1n}^{(3)}$, each weighted by a scattering coefficient a_n or b_n. If we assume the permeability, μ, of the particle and medium are the same, then we can write the scattering coefficients as:

$$
\begin{aligned}
a_n &= \frac{m\psi_n(mx)\psi_n'(x) - \psi_n(x)\psi_n'(mx)}{m\psi_n(mx)\xi_n'(x) - \xi_n(x)\psi_n'(mx)} \\
b_n &= \frac{\psi_n(mx)\psi_n'(x) - m\psi_n(x)\psi_n'(mx)}{\psi_n(mx)\xi_n'(x) - m\xi_n(x)\psi_n'(mx)} \\
x &= ka = \frac{n_{medium} 2\pi a}{\lambda}, \qquad m = \frac{n_{particle}}{n_{medium}}
\end{aligned}
\tag{2.19}
$$

where ψ_n and ξ_n are the Ricatti-Bessel functions, x is the size parameter, and m is the relative refractive indices of the particle to the medium

At this point, I'd like to take a moment to describe an interesting phenomenon that occurs in the scattering spectra of monodisperse scatters, such as polystyrene beads that arises because of the equation (2.19). As will be seen in Chapter 3, a "ripple structure" is overlaid on the scattering intensity versus wavelength for polystyrene beads. The underlying mathematics for this so-called "ripple" pattern is complex, and so an accepted physical interpretation is not available. One physical interpretation is that the ripples are a result of interference between diffracted waves and surface waves on the sphere [60]. Mathematically, the ripple structure has been generally attributable to the denominators of a_n and b_n approaching zero, causing the corresponding normal mode to dominate the scattering spectra. In tissue, the scatters are polydisperse in size, therefore this ripple structure is not seen.

Continuing with our derivation of the scattered fields, we want to get the form of the electric fields in the far-field, $kr >> d/\lambda$. We assume that the series is convergent so that we may truncate it after a large number of terms. We can now write the equation for the electric field components parallel (l) and perpendicular (r) to the scattering plane as:

$$\begin{pmatrix} E_l \\ E_r \end{pmatrix} = \cdot \frac{e^{-ikr+ikz}}{ikr} \begin{pmatrix} S_2 & 0 \\ 0 & S_1 \end{pmatrix} \cdot \begin{pmatrix} E_{l0} \\ E_{r0} \end{pmatrix} \tag{2.20}$$

where S_1 and S_2 are the scattering amplitudes:

$$S_2(\theta)=\sum_{n=1}^{\infty}\frac{2n+1}{n(n+1)}\left\{b_n\frac{P_n^1(\cos\theta)}{\sin\theta}+a_n\frac{d}{d\theta}P_n^1(\cos\theta)\right\}$$
$$S_1(\theta)=\sum_{n=1}^{\infty}\frac{2n+1}{n(n+1)}\left\{a_n\frac{P_n^1(\cos\theta)}{\sin\theta}+b_n\frac{d}{d\theta}P_n^1(\cos\theta)\right\} \tag{2.21}$$

which are truncated after a large number of terms. Thus for an incident wave with arbitrary polarization, the scattered field components are:

$$\begin{pmatrix}|E_l|^2\\|E_r|^2\end{pmatrix}=\frac{1}{k^2r^2}\begin{pmatrix}|S_2|^2 & 0\\0 & |S_1|^2\end{pmatrix}\cdot\begin{pmatrix}|E_{l0}|^2\\|E_{r0}|^2\end{pmatrix} \tag{2.22}$$

For an incident wave with a defined polarization, the relation between incident and scattered Stokes vectors is given by:

$$\begin{pmatrix}I_s\\Q_s\\U_s\\V_s\end{pmatrix}=\frac{1}{k^2r^2}\begin{pmatrix}S_{11} & S_{12} & 0 & 0\\S_{12} & S_{11} & 0 & 0\\0 & 0 & S_{33} & S_{34}\\0 & 0 & -S_{34} & S_{33}\end{pmatrix}\cdot\begin{pmatrix}I_i\\Q_i\\U_i\\Vi\end{pmatrix} \tag{2.23}$$

where

$$\begin{aligned}S_{11}&=\frac{1}{2}\left(|S_2|^2+|S_1|^2\right)\\S_{12}&=\frac{1}{2}\left(|S_2|^2-|S_1|^2\right)\\S_{33}&=\frac{1}{2}\left(S_2^*S_1+S_2^*S_1\right)\\S_{34}&=\frac{i}{2}\left(S_1S_2^*-S_2S_1^*\right)\end{aligned} \tag{2.24}$$

Mie theory is used in this dissertation to model the scattering of light from cell nuclei in oral mucosa. The measured depolarization ratio, given in equation (2.3), is modeled as a linear combination of forward and backward Mie scattering intensities, given the illumination and collection angles of our instrument. The purpose of this was to give a very brief overview of Mie theory to better aid in the understanding of the rest of this dissertation. For more extensive treatments of Mie theory, the reader is referred to refs. [61, 62].

2.8 LITERATURE REVIEW

This section gives a review of the literature on which the method of polarized reflectance spectroscopy is based. The use of scattered light to size particles has been used for many years in flow cytometry [63, 64]. Application of this technique to tissue for extracting cellular morphology is complicated by the large diffuse scattering, hemoglobin absorption, and the large distribution of scatterer sizes and scatterer types such as organelles, proteins, and cell nuclei. Each cellular substructure can contribute to the total scattering signal. Distinguishing the relative amount of scattering from individual components is a difficult task. Indeed, there is much debate as to which cellular structure is the major scatterer in tissue. In this dissertation, I will attempt to convince the reader that the major scatter for the scattering geometry probed herein is the cell nucleus, and that the average size of nuclei in tissue can be obtained from polarized reflectance spectroscopy measurements.

2.8.1 Origin of Light Scattering in Tissue

The origin of light scattering in tissue is of intense interest for noninvasive optical imaging and spectroscopy. There is much debate as to the contribution various cell substructures have on the detected scattered intensity. Extensive finite difference time domain measurements have been performed at a single wavelength by Dunn *et al* that show small organelles play a significant role in the light scattering from cells, especially for large scattering angles [32, 65]. Small angle scattering was found to be influenced by nuclear size. Theoretical work by Drezek *et al*, have revealed that the scattering pattern from single cells over a broad wavelength range is greatly influenced by the choice of cell model [66]. Drezek tested four models: scattering from a single cell nucleus, cell cytoplasm alone, a cell with cytoplasm and a nucleus, and finally a cell containing a nucleus and multiple heterogeneous organelles. High angle scattering was found to increase in a heterogeneous model for a dysplastic cell relative to a normal cell of the same size. The question then naturally arises, "what is the appropriate cell model?" It seems that this choice is highly dependent on the probing geometry – particularly on the collection scattering angles.

Mourant *et al* have performed extensive experiments to elucidate the origin of the angular light scattering within cells. In one experiment, suspensions of rat embryo fibroblasts cells, both normal and tumorigenic, demonstrated that the cell membrane does not contribute significantly to the angular distribution of light scattering [67]. Mourant did further experiments on the angular distribution of scattering intensity, and showed that small angle scattering can be attributed to large structures within a cell, such as the cell nucleus [34]. Large angle scattering was found to be more sensitive to smaller organelles the size of mitochondria [34]. Scattering at angles greater than 110 degrees was correlated to the DNA content within nuclei [68]. Over all angles, small particles on the order of 10's of nanometers in size are the dominant contributors [54]. This is not a completely unexpected result if one considers the sheer number of proteins within a cell. Thus, the scatterer size probed can be chosen with the appropriate collection geometry and model. For example, large scattering angles would probe small structures within the cell, and therefore the model should be one that included heterogeneous organelles. Conversely, a collection geometry that probed small scattering angles would preferentially probe scattering from large structures such as a cell nuclei. The corresponding model would simulate scattering from this major scatterer. In this dissertation, the nuclear size is the cell structure investigated.

Now that it has been established that nuclear size can be selectively probed, another question arises as to whether the nuclear texture, or refractive index variations, affects the scattering pattern. Drezek *et al* recently showed nuclear atypia does in fact influence the scattering pattern observed, and that as nuclear atypia increases with dysplasia, so does the scattered intensity [40]. The authors submit that modeling strategies that treat the nucleus as a homogeneous object, such as Mie theory models, would be appropriate when the collected scattered light is over a reasonable range such that the scattering cross-section variation with wavelength provided a reasonable approximation of the measured scattering.

Chen *et al* also examined the effect of refractive index variation on the total scattering cross-section using FDTD [69]. They varied the refractive index within a 5 µm sphere and compared it to Mie calculation for a 5 µm sphere with a volume average refractive index. Their results indicate that total scattering cross-section spectra for spheres with varying refractive index very closely resemble their Mie volume average refractive index counterparts.

The literature on polarized light scattering spectroscopy has shown that this method is capable of: 1.) separating the singly scattered epithelial signal from the diffuse multiply scattered stromal signal, and that 2.) the epithelial signal can be attributed to scattering from cell nuclei, 3.) nuclei can be modeled as homogenous spheres, and 4.) nuclear sizes can potentially be used as a diagnostic aid. The rest of this dissertation is devoted to the experimental validation of these points.

2.8.2 Extraction of Nuclear Size in Tissue

Fairly recently, Perelman *et al* successfully determined the average size of nuclei from normal and T84 tumor human colonic cell monolayers and *in vivo* from normal and dysplastic esophageal tissue [52]. Perelman developed an analytic model for the wavelength dependence of diffuse reflectance, based on an approximate solution to the radiative transport equation and subtracted their predicted reflectance signal from their measured values. The residual reflectance signal was attributed to single scattering from nuclei within epithelium. This single scattering spectral signal was then fit with Mie theory where the nuclear size and size distribution was varied. The best fit yielded the average nuclear size and size distribution within the tissue area probed. The *in vitro* measurements of the colonic cell monolayers yielded larger nuclear sizes and size distributions for the tumor cells. Similarly, the *in vivo* measurements of a human esophagus revealed larger nuclear sizes and size distributions for dysplastic tissue. They conclude that non-invasive determination of morphological information such as nuclear size has the potential for diagnostic discrimination of normal and dysplastic tissues.

2.8.3 Polarized Imaging: Separation of Singly and Multiply Scattered Photons

The method employed by Perelman *et al* shows great promise for non-invasive measurement of tissue morphology. However, their approach is strongly dependent on an accurate analytical model for the diffuse scattering within tissue. A simple way around this issue is to physically separate the epithelial single scattering from the diffuse stromal scattering using linearly polarized illumination and detection. This is a modification of an imaging approach first applied by R.R. Anderson in 1991 [56]. Anderson imaged skin with various benign conditions such as Rosacea, actinic and seborrheic keratosis, and inflammation [56]. The co-polarized images revealed an enhancement of surface details, and the cross-polarized images gave an enhancement of vasculature and underlying structures within pigmented lesions. The author suggests that the origin of the co-polarized images is from Fresnel reflection at the air/tissue surface and also “glare”, which can be interpreted as single scattering from within the tissue. The cross-polarized images are attributed to multiply scattered light which traveled deeper with in tissue.

Further evidence that the superficial single scattering component can be isolated from the multiply scattered component arising from deeper regions within tissue was given by S.G. Demo and R.R. Alfano in 1997 [70]. They measured the temporal profiles of a 6.5 ps pulsed laser backscattered from bovine gray matter and found that the perpendicular component arrived approximately 4 ps later than the parallel component. Again, this difference is attributed to the longer interaction time, and hence depth, that the perpendicular component has within tissue. Demos and Alfano point out that a portion of the signal that makes up the co-polarized image will be due to photons that have traveled deeper within the tissue. This is due to the fact that half of the cross-polarized signal contributes to the co-polarized image, as unpolarized light is comprised of equal parts co- and cross-polarizations. To illustrate this point, they imaged the palm of a hand and showed that the surface structure contrast can be enhanced if the perpendicular image is subtracted from the parallel image.

S.L. Jacques *et al* used this approach to image human skin with freckles and benign pigmented nevi, commonly known as moles, using a white light source [55, 71]. He showed that by taking the depolarization ratio image, superficial pigmentation, such as that found in a freckle, can be completely removed. For melanosomes not isolated to the superficial layer, as is the case for pigmented nevi, some residual absorption will remain in the depolarization images. Jacques *et al* also performed a series of monochromatic experiments with polystyrene microspheres, chicken muscle, chicken liver, porcine muscle, and porcine skin to study the transition of the initial polarization state of light after propagation through tissue. The change in the initial state of polarization was described heuristically in terms of a diffusion constant, whose value was sample dependent. Their results were consistent with the hypothesis that birefringent tissue randomizes the initial polarization state faster than non-birefringent tissues.

2.8.4 Polarization Spectroscopy for the Determination of Nuclear Size

Sokolov *et al* used polarized reflectance spectroscopy to extract the scatterer sizes and refractive indices from tissue phantoms consisting of suspensions of polystyrene beads and suspensions of SiHa cervical cancer cells. The scattering spectra were described as a linear combination of forward and backward scattering components determined from Mie theory. The bead sizes and the nuclear sizes obtained from the fits to the measured spectra corresponded with direct microscopy measurements. Indices of refraction of the cytoplasm and nuclei, also derived from their spectroscopic measurements, corresponded with phase contrast microscopy measurements. In addition, polarized reflectance spectra were obtained from a cervical tissue biopsy. Comparison to tradition reflectance measurements, without polarizers, showed a dramatic decrease in the hemoglobin absorption originating from the stroma. They conclude that this technique allows selective detection of size-dependent Mie scattering of epithelial nuclei *in vivo* for detection of epithelial neoplasia.

Backman *et al* used polarized light scattering spectroscopy (LSS) to quantitatively determine the scatter size distribution of polystyrene microspheres, normal and malignant intestinal cells, and fresh *ex vivo* biopsies of normal and tumorous human colon tissue [53]. Their approach differs from that used by Perelman et al, where the diffuse scattering from deeper structures was modeled analytically. Backman *et al* use polarized illumination and detection to directly separate the single scattering signal from the large diffusive background. The single scattering spectral signal was then fit using Mie theory. The size distributions that they extracted were in good agreement with light microscopy measurements of their samples. They conclude that polarization LSS has the potential to be used endoscopically as a diagnostic aid to detect precancerous changes *in vivo* and in real time.

Myakov *et al* presented an *in vivo* fiber optic probe for selective detection of the size-dependent scattering signatures within tissue based on polarized scattering spectroscopy [36]. They studied several phantoms modeling epithelial tissue *in vitro*, an *ex vivo* cervical biopsy, and oral mucosa *in vivo*. They showed that polarized elastic scattering spectroscopy dramatically reduces the background signal due to both diffuse stromal scattering and hemoglobin absorption. They also showed that the resulting depolarization ratio spectra can be described as a linear combination of forward and backward scattering components determined from Mie theory. The nuclear sizes and refractive indices extracted by fitting the experimental depolarization ratio spectra to this model agreed well with previously published values obtained using quantitative histopathology.

Johnson and Mourant describe a fiber optic probe for polarized spectroscopic measurements from suspensions of polystyrene beads, chicken breast, and chicken liver [72]. They qualitatively compared polarized and unpolarized measurements and found that polarized spectroscopy measurements were less affected by absorption than unpolarized measurements, as was seen by others in polarized imaging experiments. They also note that their results support earlier work in which smaller source-detector separations were shown to be more sensitive to scatterer sizes, and therefore more conducive to Mie theory fitting [73]. They hypothesize that polarized spectroscopy measurements could be used for determination of the internal morphology of cells.

2.8.5 Depolarization

The ability of the depolarization ratio, given by equation (2.3), to isolate epithelial scattering depends on two assumptions: 1.) retention of the initial polarization state after a single scattering event, and 2.) the efficiency of the lower stromal layer to depolarize incident polarized light, such that the multiply scattered signal arising from this lower layer can be effectively eliminated. In this section I will review literature in which single scattering from spheres, or particles very near spheres, is shown to have negligible depolarization of an incident polarized wave. I will also review literature which demonstrates that highly scattering media, such as stroma, depolarize linearly polarized light quickly.

The depolarization of a plane wave depends on its initial polarization, its wavelength, and the size, shape, and concentration of the scattering particles. In the epithelial layer of tissue, cells and their substructures are often modeled as spheres, even though in reality they may not be strictly spherical. Asano and Sato demonstrated that the maximum depolarization occurs for spheroids with an aspect ratio of 2 [74]. However, for spheroids with relative refractive index near 1, such as cell nuclei, the depolarization is very small. Asano and Sato also showed that the forward scattering of randomly oriented spheroids, except for thin oblate spheroids, can be approximated as spheres as their scattering is very close to that of the area equivalent spheres. In cell suspension studies by Mourant *et al,* it was shown that biological cells do not strongly depolarize linearly polarized light [41]. Hence, we can assume the scatterers within epithelial cells are approximately spherical.

Bicout *et al* demonstrated that the characteristic length for the degradation of polarization within a turbid medium, such as stroma, depends on the size of the scattering particle [75]. For spherical particle sizes small compared to the wavelength of light, which is in the Rayleigh scattering regime, incident circularly polarized light depolarizes faster than incident linearly polarized light. In the Mie scattering regime, where the particle size is greater than the wavelength of light, incident linearly polarized light depolarizes faster. These results were confirmed by Sankaran *et al* and Jarry *et al* [76-78].

Jarry went further and studied the characteristic length for which the ballistic, or single scattering, regime is valid and also explored its transition to the diffusion, or multiple scattering, regime [78]. He found that for spherical particles in the Rayleigh regime, depolarization of linearly polarized incident light occurs after 30 scattering mean free paths (SMFP). In the intermediate region between Rayleigh and Mie, the depolarization SMFP was found to be 27-35. In the Mie regime, 50 SMFP's were needed to depolarized light. Their results corresponded with those of Bicout, who found the SMFP's for Raleigh, intermediate, and Mie scattering to be 15, 25, and 65, respectively. Their Mie results also match work done by Demos and Alfano who found the depolarization to occur after 50 SMFP's [79]. Within epithelium, photons undergo on average 1 – 3 scattering events. We can therefore assume that the photons scattered from the upper layer of tissue maintain their original polarization. Within the stroma, the scattering coefficient is much larger (~ 190 cm^{-1}), and photons will accordingly undergo many more scattering events. However, Jarry *et al* concluded that there is a transitional region between pure ballistic and diffusive regimes of scattering where the photon retains some memory of its incident polarization state. The extent of this transitional regime within tissue is unknown. It can be hypothesized that within the stromal layer of tissue the transitional regime is smaller than what is predicted for polystyrene and fat emulsion tissue phantoms, because stroma is composed of a dense matrix of collagen fibrils and not spheres. The shape of collagen fibrils can be approximated as oblate spheres or as cylinders. The main point is that the depolarization from these shapes is much more efficient than spheres. Kim *et al* recently demonstrated using polystyrene bead suspensions that light can be completely depolarized after only two scattering events [80]. Within stroma, the depolarization is expected to be much more pronounced, since it is composed primarily of non-spherical collagen fibers.

CHAPTER 3

Optical sectioning using a fiber probe with an angled collection geometry: evaluation in engineered tissue phantoms and in normal volunteers*

3.1 ABSTRACT

In this chapter, I will discuss a fiber optic probe that combines polarized illumination/detection with an angled distal probe geometry to detect the size-dependent scattering at a specific depth within epithelium. Analysis of the scattering signal using Mie theory allows the extraction of scatterer size and size distribution - key parameters for precancer detection. The probe was evaluated in two tissue phantoms: polystyrene beads atop of collagen gel and multiple layers of cancer cells atop of collagen. In this chapter, I also present *in vivo* measurements in the oral cavity of normal volunteers. The sizes of scatterers extracted from the scattering spectra corresponded to independently measured values.

3.2 INTRODUCTION

Elastic light scattering spectroscopy is an optical modality that has been intensively explored for biological applications [2, 49]. It has been shown that the wavelength dependence of the elastic scattering is sensitive to morphological features of the scatterers, such as scatterer size and refractive index [52, 73, 81]. One of the

---

* The work contained in this chapter has been published in Applied Optics **43** (6), 1308-1319 (2004).

promising applications of elastic light scattering is early detection and monitoring of epithelial pre-cancers [2, 43, 49, 52, 55, 71, 73, 81-83]. It was demonstrated that during epithelial carcinogenesis there are concomitant changes in the epithelium and the underlying stromal layers [18, 19]. The morphological changes of epithelial cells associated with pre-cancer are well characterized and include increased nuclear size, increased nuclear/cytoplasmic ratio, hyperchromasia, and pleomorphism [10]. The biochemical and morphologic changes in the stromal layer are less well understood. However, their importance has been recognized, [83-85] and the changes in morphology and optical properties of stroma associated with pre-cancer were demonstrated both *ex vivo* and *in vivo* [18-20]. It was shown that the scattering cross-section of epithelial cells increases with pre-cancer [40] and the scattering of the stroma decreases with pre-cancer [86]. Characterization of morphological changes in both the epithelial and stromal layers could result in a more accurate and earlier diagnosis of pre-cancers.

Recently, a number of approaches have been proposed to separate optical signals originating in the epithelial and stromal layers. Perelman *et. al.* [52] used a combination of diffuse reflectance spectroscopy and a physical model for scattering of stroma to extract scattering of epithelial cell nuclei. Perelman *et. al.*used an analytical model for stromal scattering to extract a periodic structure, attributed to single scattering by epithelial cell nuclei, from the diffuse reflectance spectroscopic measurements of epithelial tissue. Mie theory was subsequently used to approximate scattering of epithelial cells and to obtain nuclear size distribution.

Alternative approaches that were developed to separate the signals from epithelium and stroma at the instrumentation level include polarized illumination/detection and optimization of the distal probe geometry. The first technique exploits the fact that light undergoes single scattering events in the upper epithelial layer and is multiply scattered in the underlying stroma. Photons that undergo single scattering events in the epithelium retain the polarization of the incident beam, whereas multiply scattered photons from the stroma have random polarization [36, 37, 53, 55, 56, 71]. The perpendicular component of the scattered light is subtracted from the parallel component to eliminate the large diffusive background and the hemoglobin absorption originating in the stromal layer [36, 37, 53]. The resulting spectra represent the scattering from epithelial cells that can be used to analyze the morphology of epithelial nuclei [36, 37, 53].

Approaches which vary distal probe geometries such as the separation between the illumination and collection fiber, window thickness and fiber diameter have been evaluated as means for depth specific targeting of fluorophores in epithelial tissue [87-89]. A rigorous Monte Carlo simulation study showed that window, or spacer thickness, and the collection/illumination fiber separation can be optimized to select for fluorophores at specific depths [88]. The results of another Monte Carlo study, showed that a variable-aperture method could also be used to provide depth distribution of fluorophores in layered epithelial tissue [87].

This chapter describes a novel integrated approach that combines the advantages of polarized illumination/detection with an optimized distal fiber probe geometry to selectively collect size-dependent scattering at various depths within epithelial tissue. In this design, the collection fibers of the probe are tilted, causing their acceptance cones to cross; this permits the collection of scattered photons from a specific volume at a selected depth. This approach was evaluated in engineered phantoms of increasing complexity. First, a two-layer phantom consisting of 6.25 μm polystyrene beads on top of a collagen matrix was used. Then, a biologically relevant tissue phantom consisting of multiple layers of cervical cancer (SiHa) cells atop a collagen matrix was prepared. Simple algorithms based on the geometrical overlap of the illumination and collection acceptance cones and the scattering properties of the phantom were developed to model the experimental data. The fiber probe was then used to measure polarized reflectance spectra from the oral cavity mucosa of 6 normal volunteers. The nuclear sizes obtained from the measurements are in excellent agreement with previously published values [90]. Nuclear morphology is one of the key histological parameters in cancer diagnosis, which currently can only be assessed using a painful and invasive biopsy. The fiber based optical approach can potentially provide the same information as histological analysis non-invasively and in real-time. With the distal probe design presented in this chapter, this information can also be obtained from depth specific sites within tissue.

3.3 METHODS

3.3.1 Probe Fabrication

Figure 3.1 illustrates the design concept of our optical fiber probe for polarized reflectance measurements *in vivo.* The probe consists of a central fiber delivering polarized illumination to the tissue site of interest and two independent fibers for simultaneous collection of the scattering components with polarizations parallel and perpendicular to the incident light.

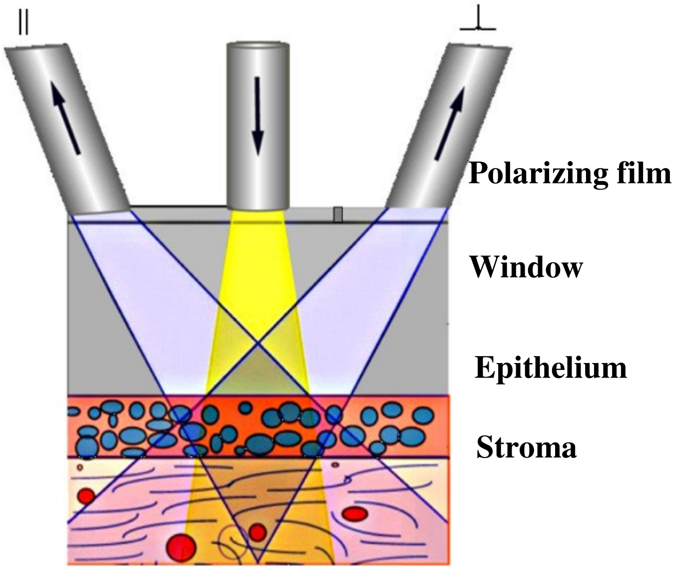

Figure 3.1: Schematic of *in vivo* probe design. The center fiber delivers linearly polarized light to the tissue. The outer fibers collected the scattered light with polarization parallel and perpendicular to the incident polarization. Tilting the collection fibers allows overlap of illumination and collection acceptance cones within the epithelial layer.

A MATLAB code was developed to model the two-dimensional cross-section of the illumination rays with the collection acceptance cones on a layered sample. All parameters such as fiber separation, collection fiber tilt, and window thickness could be varied. The collection fibers of the constructed probe are tilted 37 degrees with respect to the illumination fiber. This angle was chosen to give maximum overlap of the illumination and collection acceptance cones in the epithelium.

Tilting the collection fibers with respect to the illumination fiber allows detection of scattered photons from the same location within a sample. Fiber separations within the probe were chosen so that Fresnel reflections from interfaces within the distal end of the probe and at the tissue would be outside of the acceptance angles of the collection fibers. With an angled geometry, however, total internal reflection (TIR) from any of the various interfaces must be considered. We performed calculations that show TIR will not occur for the collection fibers tilted less than 51 degrees.

Two probes were constructed: one for experiments with tissue phantoms, another for *in vivo* measurements. Both probes were built using three 200 μm core diameter fibers with 0.22 NA. The fibers were glued inside a stainless steel disk to give the desired geometry. The holes in the steel disk were made at the desired angle by electrical discharge machining (Norman Noble, Inc.). The disk with fibers was placed inside a stainless steel tube, with an outer diameter of 9.5 mm to accommodate the long-term bending radius (~ 44 mm) of the fibers. The long-term bending radius is the minimum fiber bend that can be applied over a long period without significant stress fractures occurring. The tube was filled with glue (EPO-TEK 301-2, Epoxy Technology) to further reinforce the fibers against breakage.

After drying, the end of the assembly was polished to a 100 nm finish. Two pieces of polarizing film (3M) were then glued onto the disk. The transmission axes of the polarizing films were orthogonal to one another, as shown in Fig. 3.2 (a). Finally, a protective fused silica window was glued atop the polarizing film. The finished distal end of the probe is shown in Fig 3.2 (b). The glue used throughout was an optically transparent biocompatible glue (EPO-TEK 301-2, Epoxy Technology).

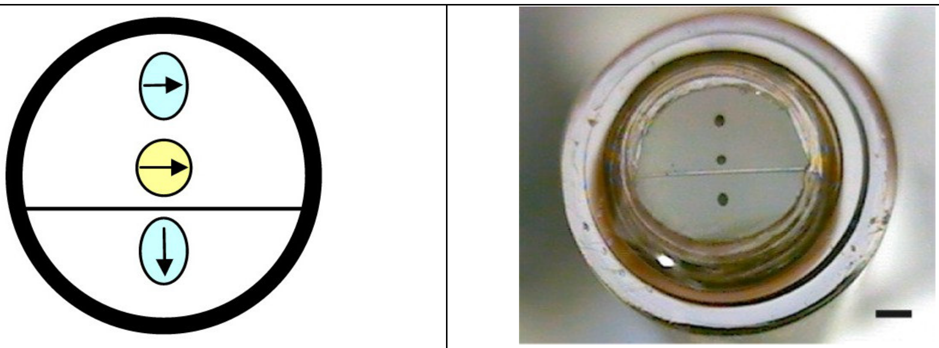

(a) (b)

Figure 3.2: (a) Illustration of the orientation of the polarizing film on the distal end of the probe. The transmission axes of the polarizing film are indicated by arrows. (b) Picture of the distal end of the probe. Scale bar is 1 mm.

Figures 3.3 (a) and (b) show the distal end of the probe in a fluorescing medium. In Fig. 3.3 (a), light is channeled through the two collection fibers and in Fig. 3.3 (b) light is also channeled through the illumination fiber. The depth at which the collection acceptance cones overlap can be controlled with the appropriate choice of window thickness. For the phantom measurements, a thin protective window was chosen so that the overlap region would be deep within a sample. For *in vivo* measurements, a window thickness was chosen so that the overlap would coincide with the epithelial layer of oral mucosa.

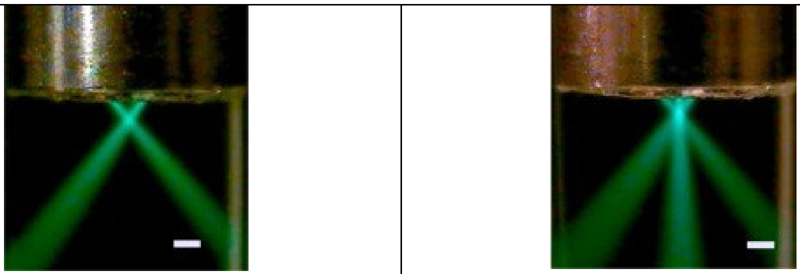
(a) (b)

Figure 3.3: (a) Picture of the distal end of the probe in a fluorescing medium. Overlap of the collection acceptance cones is clearly seen when light is channeled through the collection fibers. (b) Overlap of the illumination cone and the collection acceptance cones when light is delivered through all three fibers. Scale bar is 1mm.

3.3.2 Probe Sampling Volume

The axial extent of the sampling volume of the probe was determined by measuring the intensity of scattered light collected by a single collection fiber from a diffusely scattering white substrate (SRS 99, Labsphere) for a series of probe-substrate separations. The substrate is opaque, so the collected signal is acquired only from the substrate surface. The measurement procedure is described in detail in section 3.5.1. The dependence of the intensity of the scattered light versus probe-substrate distance is shown in Figure 3.4.

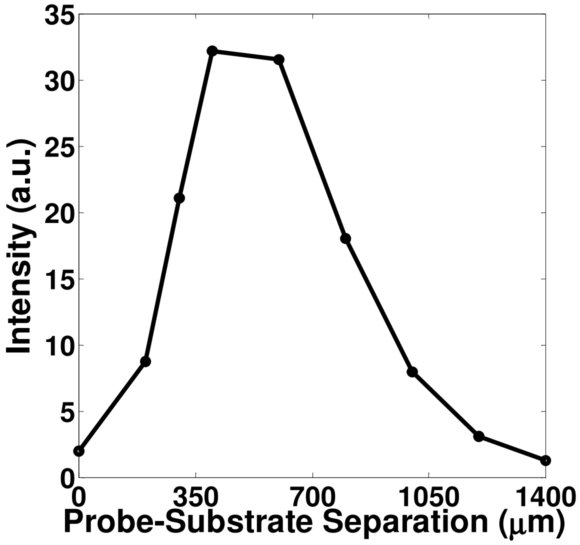

Figure 3.4: Intensity of scattered light collected by a single collection fiber from a diffusely scattering substrate as a function of probe-substrate separations.

3.4 PHANTOMS

3.4.1 Two Layer Bead Phantoms

Figure 3.5 (a) illustrates the design concept for the phantom: approximately 330 μm thick layer of 6.25 μm +/- 0.05 μm polystyrene beads (Bangs Labs) embedded in collagen matrix on top of a thick layer of collagen type I gel. The size and distribution of the beads were determined by the manufacturer using optical microscopy and an Elzone particle analyzer. The upper bead layer models epithelial nuclei and the bottom layer models stroma. First, collagen gels were prepared from type I collagen (Roche) in standard 24-well ELISA plates using a modification of the manufacturer's protocol.[91] Briefly, lyophilized collagen was dissolved in 0.2% acetic acid to 3 mg/mL. Phosphate

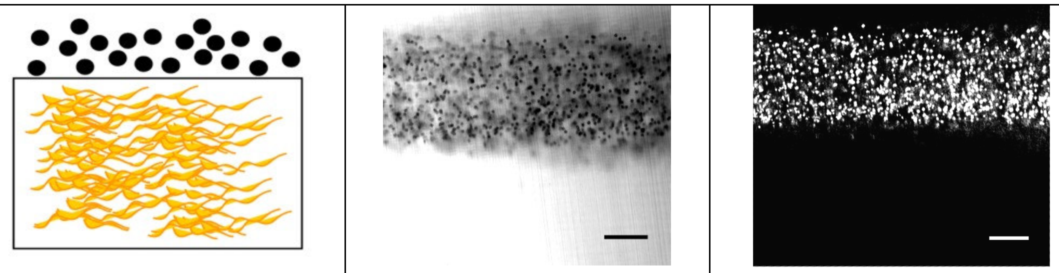

(a) (b) (c)

Figure 3.5: (a) Illustration of a two-layer bead phantom. The upper layer is composed of 6.30 μm polystyrene beads embedded in a collagen gel. The lower layer is a collagen gel. (b) Transmittance image of a transverse section of the phantom. Beads are seen as black dots. (c) Corresponding reflectance image. Beads are seen as white dots. Scale bars are 100 μm.

buffered saline and 0.2M HEPES solutions were added to provide physiological pH, ionic strength and buffering capacities. The collagen was allowed to gel at 37°C for 20-30 minutes. To prepare the top layer, polystyrene spheres were suspended in a prepared collagen solution to a dilution of 28 times the original 10% (w/w) solution of the beads. The packing fraction of the beads at this dilution is 0.0034, which is well within the independent scattering regime. The bead layer was placed on top of the collagen gels prepared in the first step and allowed to gel, resulting in a two-layer phantom. The lower collagen gel layer was ca. 0.5 cm thick.

After polarized reflectance measurements, the phantoms were removed from the wells, transversely sectioned with a Krumdieck tissue slicer, and placed on microscope slides for confocal imaging. A Zeiss Leica inverted epi-fluorescence/reflectance laser scanning confocal microscope, equipped with a Kr/Ar mixed gas laser, was used for image acquisition. A transmittance image was acquired with 488 nm wavelength light, and a corresponding reflectance image was taken with 647 nm illumination (Fig. 3.5, b and c).

3.4.2 Two Layer Cell Phantoms

A two-layer biologically relevant tissue phantom was constructed using SiHa cervical cancer cells (Fig. 3.6). The top layer was composed of densely packed SiHa cells to mimic epithelium and the bottom layer was a collagen gel to model the underlying stroma.

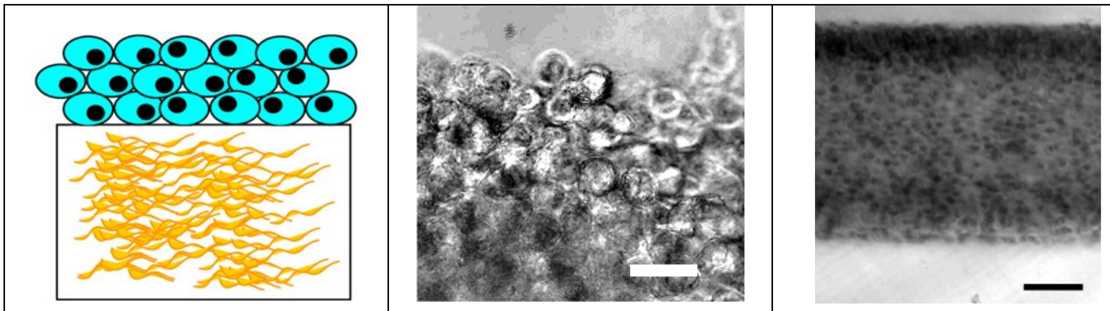

(a) (b) (c)

Figure 3.6: (a) Illustration of a two-layer cell phantom: the upper layer is composed of densely packed SiHa cervical cancer cells and the lower layer is a collagen gel. (b) Transmittance image illustrating the dense packing of SiHa cells. Scale bar is 30 μm. (c) Transmittance image of the cell phantom at a lower magnification. Scale bar is 100 μm. A distinct boundary can be seen between the cell and collagen layers.

To prepare multiple layers of densely packed epithelial cells, a suspension of SiHa cells was spun down and a very small amount of buffered collagen type I was added to the pellet. The concentration of the cells in the pellet was 60-100 million cells/ml. Then a small volume of this mixture was added on top of a prepared collagen gel. The volume of the added epithelial cells was controlled so that the thickness of the upper layer would be ca. 400 μm. The collagen in the upper layer was allowed to gel resulting in multiple layers of separated epithelial cells embedded in diluted collagen matrix. The construct was kept in DMEM (Dulbecco) plus 5% FBS (HyClone) for approximately 24 hours. During this time, the cells in the upper layer kept growing and filled up the space between them, resulting in the formation of a highly dense cellular layer of controlled thickness on top of the bottom collagen layer. Transmittance images of the resulting phantoms are shown in Fig. 3.6 (b) and (c).

A series of experiments were conducted to compare cell tissue phantoms with real biological squamous epithelium. The density of cells in the upper layer of cell phantoms was compared with density of cells in cervical biopsies using a confocal fluorescence microscope. The confocal microscopy images showed that the density of cells in the cell tissue phantom is very similar to that of real biological tissue. The thickness of the upper cell layer was constructed to be comparable to that of oral epithelium (~300 μm). Using UV-Vis spectrophotometry, the scattering coefficient of the cell layer was determined to be ca. 71 cm $^{-1}$ at 800 nm as shown in Figure 3.7. Absorption of cells at this wavelength was neglected. This agrees well with 69 cm^{-1} at 810 nm reported for cervical

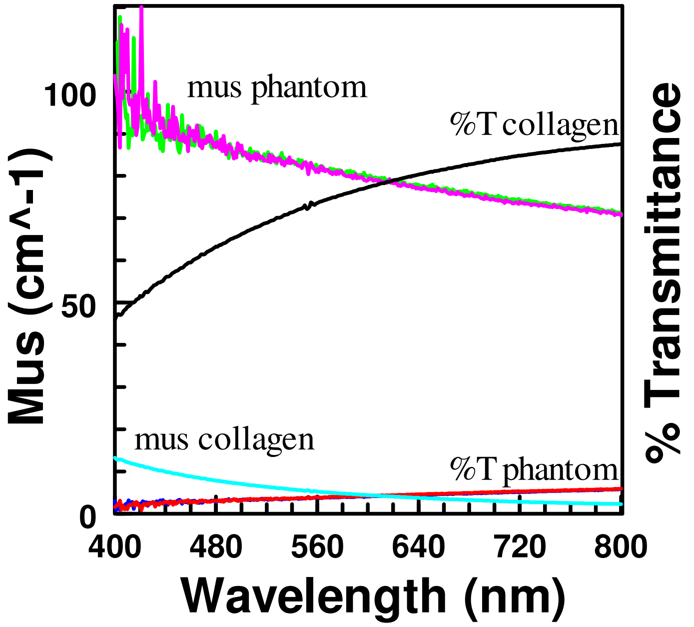

Figure 3.7: Scattering coefficient and percent transmittance of SiHa cell phantom. Pink and green curves are the measured scattering coefficient for SiHa cell phantom measurements. The cyan curve is the measured scattering coefficient for collagen alone. The red and blue curves are the measured transmittance of the SiHa cell phantom. The black curve is the transmittance of collagen alone.

precancerous epithelium [92]. The thickness of the lower collagen layer was significantly greater (~0.5 cm) than the axial overlap between the collection and illumination acceptance cones such that it could be assumed as a semi-infinite medium. Previous work has also demonstrated that the depolarization ratio spectrum of collagen gel is very similar to that of the stromal layer of cervical biopsy.

Stacks of confocal fluorescence images of the phantoms were acquired so that their nuclear sizes could be directly measured (excitation wavelength: 488 nm, emission wavelength: 505 nm). In the fluorescence images, a nucleus appears as a dark sphere surrounded by bright fluorescent cytoplasm. This allowed measurement of the average diameter of cell nuclei. The stacks were analyzed using NIH ImageJ software. For a given cell, the nuclear diameter was measured for the largest nuclear cross-section within a stack. This was repeated for all cells visible within a stack of images.

3.5 MEASUREMENTS

3.5.1 Depth Resolved Polarized Reflectance in Phantoms

Optical sectioning was accomplished by placing prepared phantoms on a translation stage that allowed vertical positioning via a fine pitch screw. The probe was placed inside a holder in a second translation stage and placed directly over the phantom. Water was added to the well containing the phantom for index matching. The displacement of the probe was controlled using a differential micrometer (Newport, DM 17-25). The sample was brought up toward the probe into direct contact using the fine pitch screw and the first measurement was taken. Then, the probe was withdrawn in 100 - 200 μm increments away from the phantom using the differential micrometer, and the intensity of elastically scattered light with polarizations parallel and perpendicular relative to the polarization of the illumination light was measured at each position.

The illumination fiber was connected to a CW broadband lamp (Dolan-Jenner Industries, Inc, Fiber-Lite Series 160). The collected scattered light was focused onto a

250 μm entrance slit of a single grating spectrograph (f/3.6, 300 lines/mm grating, 5 nm spectral resolution, Monospec 16, Jarrel Ash) coupled to a photodiode array detector (IRY-700, Princeton Instruments). The data acquisition was controlled by a computer. A mercury lamp (ORIEL) was used for wavelength calibration of the spectrometer. All spectra were normalized using the signal from a diffusely scattering white substrate (SRS 99, Labsphere).

3.5.2 In Vivo Measurements

For *in vivo* measurements, the fiber probe that had optimal overlap of the epithelium with the collection and illumination acceptance cones as illustrated in Fig. 3.1 was used. *In vivo* measurements were taken from normal volunteers at The University of Texas at Austin. Informed consents were obtained and the study was reviewed and approved by the Internal Review Board of The University of Texas at Austin. The probe was disinfected before and after each volunteer in an activated dialdehyde solution (Cidex, Johnson & Johnson). To mimic a clinical environment, measurements were taken under room light illumination. Figure 3.8 shows the detection schematic for polarized reflectance measurements. To reduce the room light contribution to a negligible level, the illumination fiber was connected to a Xe pulsed lamp (Hamamatsu L7685), which provides ca. 4 μs pulses at a repetition rate of 30 Hz. Excitation light from the Xe pulsed lamp was coupled into a 200 μm core diameter fused silica optical fiber (NA 0.22, Fiberguide Industries). The excitation light passed through a 320 nm long band-pass filter (Oriel Instruments) to eliminate UVC and UVB radiation from the

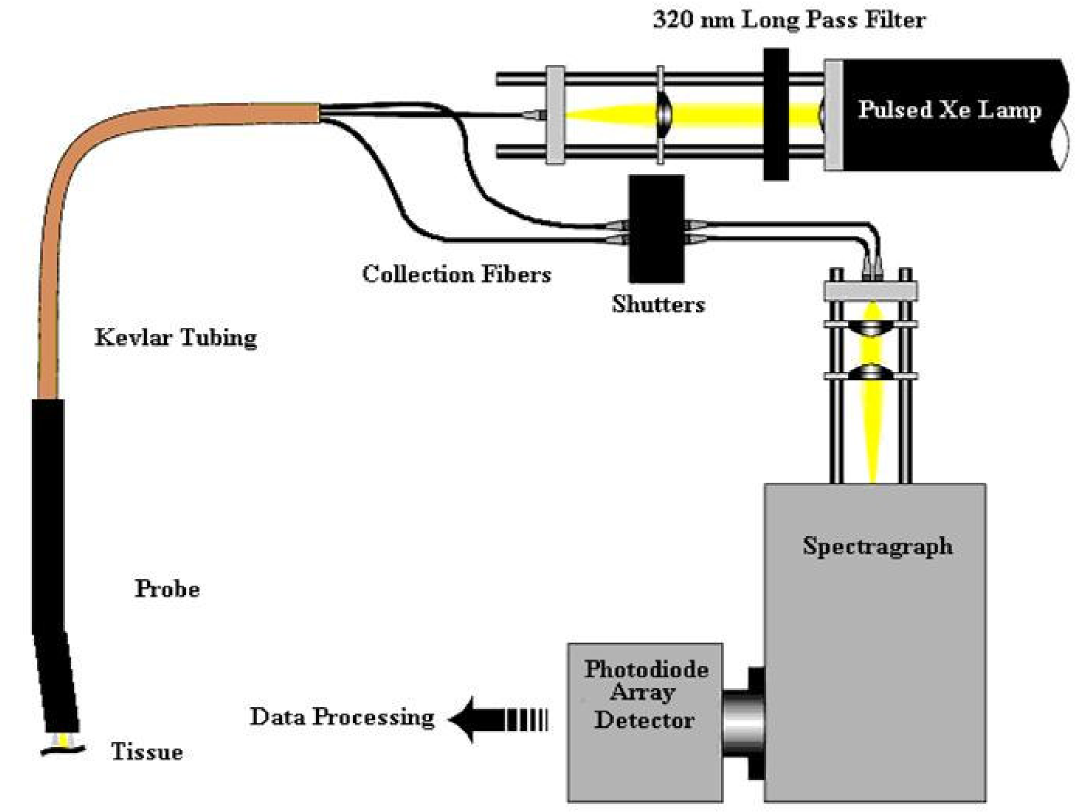

Figure 3.8: Schematic of polarized reflectance spectroscopy instrument for measurements *in vivo*.

lamp. The collected light passed through shutters (one shutter for each collection fiber) and was focused on the 250 μm entrance slit of a single grating spectrograph (f/3.8, 300 lines/mm grating, Monospec 18, Jarrel Ash) coupled to an intensified photodiode array detector (IRY-700, Princeton Instruments). The detector worked in gated mode and was open only for the duration of a pulse from the Xe lamp (ca. 3.5 μs). The shutters worked in an alternative mode – when one shutter was open the other one was closed, allowing independent detection of the components of scattered light with polarization parallel and perpendicular to the polarization of the excitation light. The shutters alternated with a frequency of 15 Hz which was synchronized to every pulse of the Xe lamp. The spectra collected from two orthogonal polarizations were stored in two different files on a PC computer, which controlled data acquisition and processing. The total collection time was ca. 1 minute, corresponding to 1800 pulses of the Xe lamp.

3.6 THEORETICAL MODELS

In the following sections, two theoretical models are presented. In section 4.6.1, the computational procedure and the Mie theory based model used to extract nuclear size and size distribution from the fit of measured depolarization ratio spectra are described. In section 4.6.2, the algorithms that were used to model the dependence of the total integrated intensity of light scattering from bead and cell phantoms as a function of phantom/probe separation are detailed.

3.6.1 Extraction of Scatterer Sizes

For each sample, light which is elastically scattered was measured with polarization parallel and perpendicular relative to the polarization of the illumination light. Dark current was recorded and subtracted from all measured spectra. The following depolarization ratio (*D*) was calculated:

$$D(\lambda) = \frac{I_{II}(\lambda) - I_{\perp}(\lambda)}{I_{II}^{S}(\lambda) + I_{\perp}^{S}(\lambda)} \qquad (3.1)$$

where $I_{II}(\lambda)$ is the component of the light scattered by the sample with polarization parallel to the incident light, $I_{\perp}(\lambda)$ is the component with polarization perpendicular to the incident light, and λ is the wavelength of the light. The normalization term in the denominator is the total intensity of light (the perpendicular plus the parallel component) collected from a diffuse scattering substrate (Labsphere, SRS-99). This normalization accounts for the spectral characteristics of the excitation lamp and the spectrometer. The ratio $D(\lambda)$ is called the depolarization ratio spectrum throughout this dissertation.

Previously, it has been demonstrated that the following equation for the depolarization ratio spectrum can be derived for a distal probe geometry with all fibers parallel [36, 37]:

$$D(\lambda) = a(\rho)B(\lambda) + b(\rho)S(\lambda)F(\lambda) + cS(\lambda) + DC \tag{3.2}$$

where $a(\rho)$, and $b(\rho)$ are empirical parameters dependent on the number of nuclei per unit volume ρ; $F(\lambda)$ and $B(\lambda)$ are the wavelength dependent forward and backward scattering from nuclei in the epithelial layer, respectively; $S(\lambda)$ is the wavelength dependent depolarization ratio of collagen matrix, c is an empirical parameter determining the contribution of $S(\lambda)$, and DC is a constant offset. Analysis revealed that this equation can be extended to an angled distal probe geometry by appropriately adjusting the scattering angles for the Mie calculation of $F(\lambda)$ and $B(\lambda)$. The epithelial nuclei were modeled as a Gaussian distribution of polydisperse spheres with an average refractive index. Therefore, Mie theory was used to calculate forward and backward scattering components. The details of this theoretical model and the fitting of the depolarization ratio spectra are described extensively in refs. [36] and [37]. Briefly, the measured depolarization ratio spectra were fit by varying the scatterer size and size distribution with fixed refractive index. For each diameter and size distribution, $F(\lambda)$ and $B(\lambda)$ were calculated. Then, a standard non-negative least squares algorithm was used to fit the experimental data using equation (3.2) and to obtain the coefficients $a(\rho)$, $b(\rho)$, c, and DC. The standard sum of the squared error (SSE) between the experimental spectrum and the fit was determined for each set of parameters. The fit with the smallest SSE was selected as the best fit.

The following values of refractive index were used in the fitting procedure: $n_{beads} = 1.59$, $n_{collagen} = 1.35$, $n_{nuclei} = 1.4235$, $n_{cytoplasm} = 1.374$. The bead refractive index was given by the manufacturer (BangsLabs, Inc). The nuclear and cytoplasmic refractive indices used were obtained from previously reported measurements described in refs. [36] and [37]. All refractive indices were assumed to be nondispersive. For epithelium and tissue phantoms, absorption is significantly lower than scattering in the visible wavelength range. Therefore, it is assumed that all refractive indices are real.

3.6.2 Modeling of Depth Resolved Polarized Reflectance Measurements

In this section, algorithms used to model the depth resolved polarized reflectance measurements which are described in section 4.5.1 are presented. The algorithms model the total integrated scattering signal as a function of probe-sample separation. The theoretical simulations used for both bead and cell phantoms is based on geometry considerations relating to the volume of overlap of the illumination and collection acceptance cones within the phantoms, as well as Mie theory calculations of the scattering properties of beads and cells.

3.6.2.1 Bead Phantom

The major goal of the theoretical simulation was to describe the relative changes in the total integrated intensity of backscattering by polystyrene beads as a function of probe-sample separation. It is assumed that the intensity of the collected backscattered signal was proportional to the volume of overlap of the illumination and collection acceptance cones within the bead layer. For each probe-sample separation the overlap volume was divided into parallel *en face* planes. Then for every *en face* plane, 10,000 random points were generated in a square area, whose side length was determined by the diameter of the illumination circle. Each random point that was inside the overlap of the illumination circle and the collection ellipse was counted as a scatterer and was given a weight factor. The factor was given by the multiplication of the solid angle subtended by the scatterer to the collection fiber and the Henyey-Greenstein phase function. The phase function was calculated using the anisotropy factor, which was determined from Mie theory. The scattering angle was defined as the angle between a ray drawn from the center of the illumination fiber to the scatterer and a ray drawn from the scatterer to the center of the collection fiber. The sum of weighted scatterers from all *en face* planes yielded a value proportional to the intensity of the total backscattering signal at a particular probe-sample separation. This procedure was performed for each probe-sample separation and the resulting curve was compared with the experimentally measured dependence of the total backscattering intensity of beads on probe-sample separation.

3.6.2.2 Cell Phantom

The forward scattering component from the cell phantoms was extracted from the best fit of the measured depolarization ratio spectra, as described in section 4.6.1. Calculations showed that forward scattering is the major component in scattering of cell phantoms. Therefore, the dependence of the forward scattering on probe-sample separation was explored. For each probe-sample separation the forward scattering component was integrated over the wavelength range of 450 – 650 nm. The dependence of the total integrated forward scattering on probe-sample separation was simulated as described below.

The results that are presented in this chapter suggest that the detected forward component arrives at the collection fiber after undergoing two scattering events (term $b(\rho)S(\lambda)F(\lambda)$ in Equation (3.2): forward scattering by nuclei in the upper cellular layer and another at the stromal layer where the light is redirected toward the collection fibers (Fig. 3.9). The scattering at the stromal layer can occur due to: (1) diffuse reflectance at the interface between the collagen and the cellular layers because of the index mismatch between the two layers (Fig. 3.9, a and b), which will be called the *interface* effect, and (2) single backscattering events from within the lower collagen layer which does not significantly change the original polarization of the illumination light – a *volume* effect (Fig. 3.9, c and d).

A MATLAB program to model the contributions of these two sources to the total integrated intensity of the forward scattering component of nuclei as a function of probe-phantom separation was implemented. In the model, it is assumed that: (1) both sources

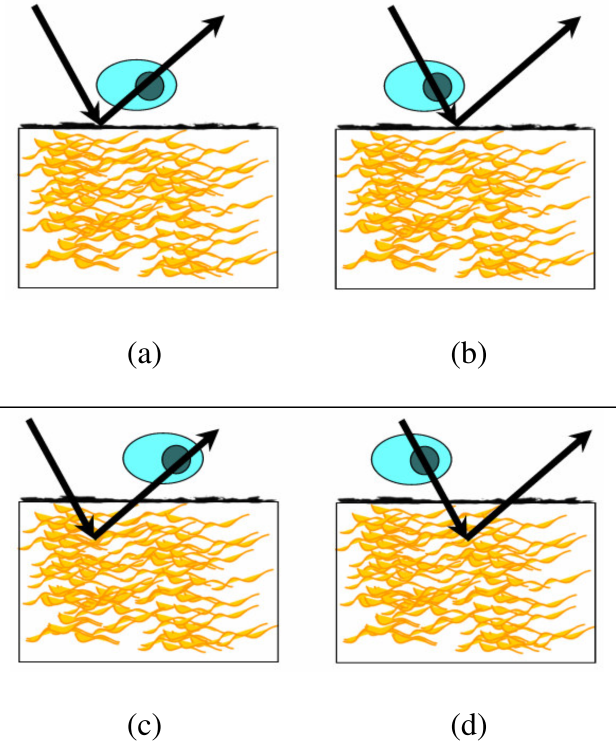

Figure 3.9: Illustration of the mechanisms for detection of forward scattering in epithelial tissue for a backscattering collection geometry: (a) and (b) represent the “interface” effect, and (c) and (d) represent the “volume” effect. (a) A photon undergoes diffuse reflection at the cell/collagen interface due to the refractive index mismatch, then is forward scattered by a cell nucleus. (b) A photon is first forward scattered by a cell nucleus, then is reflected back toward detector at the cell/collagen interface. (c) A photon is backscattered inside the collagen layer, then is forward scattered by a cell nucleus. (d) A photon is first forward scattered by a cell nucleus, then is backscattered in the collagen layer toward the detector.

contribute independently to the collected forward scattering; (2) the intensity of the forward scattering component of nuclei that reaches the detector is directly proportional to the amount of light that is “redirected” at the cell-collagen interface and the collagen layer. First, the dependence of the total intensity of forward scattering as a function of probe-sample separation for the “interface” and the “volume” effects was independently simulated. Then, the obtained profiles were used to fit the experimentally measured dependence of the integrated forward scattering component on probe-sample separation. A non-negative least squares fit was used and the results were plotted as a function of probe-sample separation.

To model the contribution from the index mismatch at the cell/collagen interface (Fig. 3.9, a and b) it was assumed that: (1) diffuse reflectance occurs at the rough surface of the interface; (2) the reflected light is distributed over a 2π solid angle; and (3) only the portion of the reflected light within the acceptance angle of the collection fiber contributes to the detected forward scattering by epithelial nuclei. The calculations were similar to those performed for the bead phantom. For each probe-sample separation, 10,000 random points were generated at the cell/collagen boundary in a square area with a side length given by the diameter of the illumination circle. Each point within the area of overlap between the illumination circle and the collection ellipse was considered a scatterer. Each point was weighted by the solid angle subtended by the source to the collection fiber and the Henyey-Greenstein scattering phase function. The scattering angle used in the calculation of the phase function was defined as the angle between a ray drawn from a source point to the center of the collection fiber, and a ray drawn from the same source point to a random location within the en face area of the collection fiber. For a single source point, 1000 random points were generated at the collection fiber; hence 1000 angles were calculated. The sum of weighted scatterers yielded a value proportional to the total intensity of the forward scattering at a particular probe-sample separation. This procedure was performed for each probe-sample separation resulting in the dependence of the integrated forward nuclear scattering component on the separation for the “interface” effect.

To simulate the contribution to the integrated forward scattered signal owing to single backscattering events inside the collagen layer (Fig. 3.9, c and d) it was assumed that at each probe-sample separation the forward scattering is proportional to the volume of overlap of the illumination and the parallel collection cones within the collagen matrix. Therefore, to obtain the dependence of intensity of the total integrated forward scattering as a function of probe-phantom separation, the volume of overlap between illumination and collection cones for each separation was calculated. The linear combination of the theoretical curves was used to fit the experimentally obtained dependence of the integrated forward scattering signal on probe-sample separation.

3.7 RESULTS

Fig. 3.3 (a) and (b) provide a visual illustration of the probe design and also demonstrate that the optimum distance from the distal probe end for a targeted tissue layer is in the region where all three beams intersect. The curve in Figure 3.4 shows the dependence of light intensity collected from a diffusely scattering white substrate as a function of probe-substrate separation. The FWHM of this curve is ca. 560 μm, which is an experimental measure of the sampling volume of the fiber probe in the axial direction. The performance of this fiber probe design in two types of engineered tissue phantoms that resemble the morphology of epithelial tissue was evaluated.

First, a two-layer phantom where 6.30 μm polystyrene beads mimic epithelial nuclei as shown in Fig. 3.5 (a) was used. Figures 3.5 (b) and (c) are transmittance and confocal reflectance images of the two-layer phantom, respectively. The beads are seen as black dots in the transmittance image because they attenuate the transmittance light due to scattering. In contrast, the beads appear as white dots in the reflectance image because of strong backscattering from the beads. The images demonstrate that the layer with polystyrene beads is uniform in thickness and density.

Figure 3.10 (a) shows the depolarization ratio spectra obtained from the bead phantom for a series of probe-sample separations. When the probe is in direct contact with the phantom (probe-sample separation = 0 μm, curve (v)), the region of overlap between the illumination and collection fibers is below the bead layer of the phantom, therefore only the lower collagen layer should be effectively sampled by the probe. Indeed, the spectrum for this depth is relatively flat and does not have the high frequency components which are characteristic for backscattering from polystyrene beads. As the separation between the probe and the sample increases, the backscattering contribution from the beads becomes apparent as high frequency oscillations [curve (iii)]. The amplitude of the oscillations increases and peaks at a probe-sample separation of

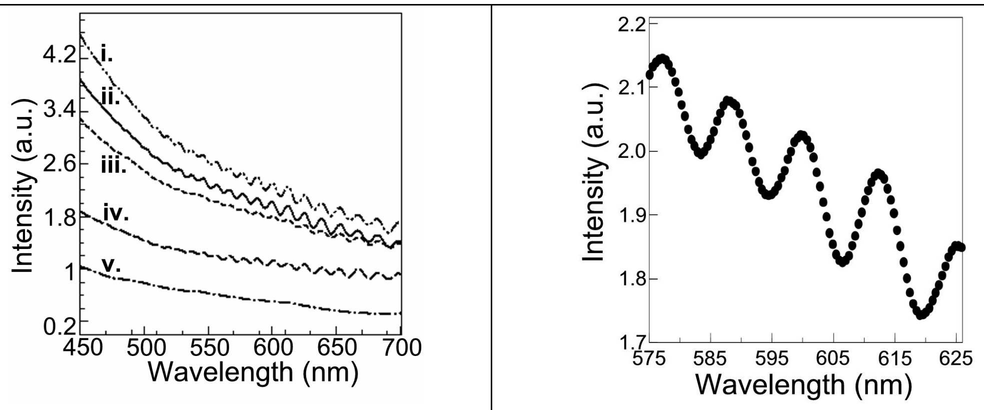

(a) (b)

Figure 3.10: Depth resolved polarized reflectance measurements in two-layer bead phantom. (a) Depolarization ratio spectra for a series of probe-sample separations: i.) 800 μm, ii.) 500 μm, iii.) 400 μm, iv.) 1000 μm, v.) 0 μm. (b) Close-up of the depolarization ratio curve (ii). Each measured point is indicated by a black dot.

approximately 500 μm [curve (ii)]. Figure 3.10 (b) is a close-up of the depolarization ratio spectrum for a probe-sample separation of 500 μm. It shows that the spectral sampling of the system is well above the ca. 10 nm oscillation frequency of the spectrum. For each probe-sample separation, the mean diameter of the beads based on the polarized reflectance measurements was calculated. The fitting consistently yielded 6.25 μm for the bead diameter and corresponded well with the manufacturer value of 6.30 μm.

The total integrated intensity of light scattering from the lower collagen layer and the total integrated backscattering signal from the beads are plotted in Fig. 3.11 as a function of probe-sample separation. Both profiles are normalized to one at their

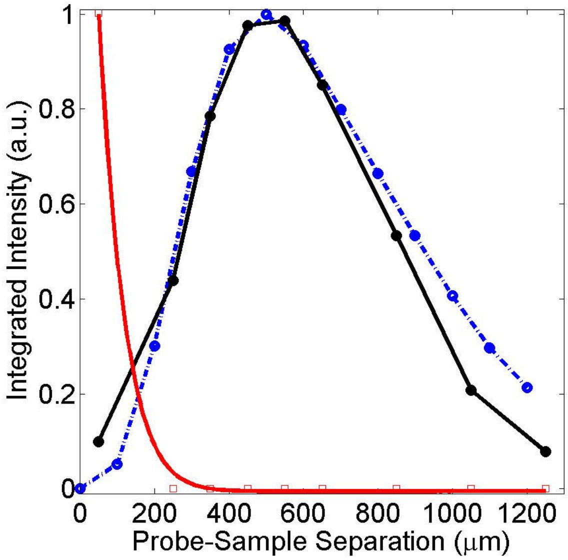

Figure 3.11: Dependence of the total integrated backscattering signal from beads and scattering from the lower collagen layer on probe-sample separation: the integrated bead backscattering signal and the integrated collagen scattering obtained from the measured depolarization ratio spectra are shown as the solid and dashed curve, respectively. The theoretical simulation of the bead scattering is plotted as a dashed-dot line.

respective maximum values. The integrated backscattering from beads, shown as a solid curve in Fig. 3.11, is in very good agreement with the theoretically predicted intensity profile, shown as a dashed-dot curve in Fig. 3.11. The integrated signal from collagen sharply decreases as the overlap region is moved out of the bottom collagen layer and into the upper bead layer.

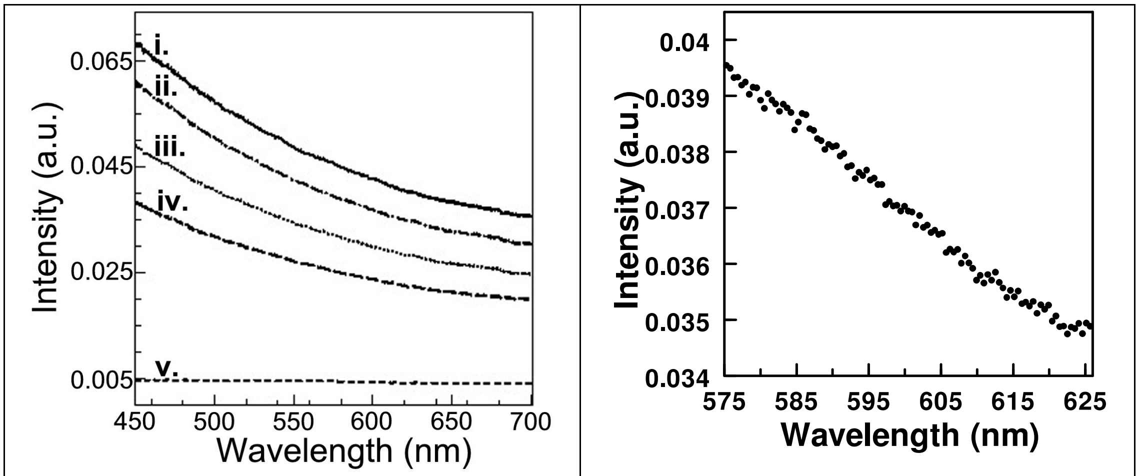

(a)

(b)

Figure 3.12: Depth resolved polarized reflectance measurements in a two-layer cell phantom. (a) Depolarization ratio spectra for a series of probe-sample separations: i.) 800 μm, ii.) 600 μm, iii.) 400 μm, iv.) 200 μm, v.) 0 μm. (b) Close-up of depolarization ratio curve (ii) showing the spectral sampling. Each measured point is indicated by a black dot.

Similar depth resolved reflectance measurements were performed on a biologically relevant two-layer tissue phantom where multiple layers of densely packed SiHa cervical cancer cells formed the upper portion of the phantom (Fig. 3.6). Figure 3.12 (a) shows that, contrary to the bead phantom, there is not a high frequency component in the depolarization ratio spectra of the cell phantom. For each spectrum, depolarization ratio spectra were modeled as described in section 4.6.1 to determine nuclear diameter and size distribution. The minimum in the SSE gives the best fit values for nuclear morphology.

The average nuclear size and distribution extracted from these depolarization ratio spectra using Mie theory calculations were 7.5 μm and 0.7 μm, respectively. These values are in good agreement with the size and the distribution of 7.9 μm and 0.8 μm extracted from direct confocal microscopy measurements of the phantom.

The total integrated forward component of scattering from cell nuclei is plotted as a function of probe-sample separation in Fig. 3.13 (b, solid curve). In section 3.6.2.2, the mechanism for detection of forward scattering events using an inherently backscattering probe geometry is described as arising from a "volume" and an "interface" effect (Fig. 3.9). The contribution to the integrated forward scattering due to the "volume" effect monotonically decreases as the probe-sample separation increases (Fig. 3.13, b, dot-square curve), while the contribution due to light scattering at the interface between cellular and collagen layers exhibits a peak similar to the experimental curve (Fig. 3.13, b, compare solid and dot-diamond curves). This peak corresponds to the maximum area of overlap between the interface and the acceptance cones of the collection/illumination fibers. A linear combination of the obtained theoretical profiles describes the main features observed in the experimental data (Fig. 3.13, b).

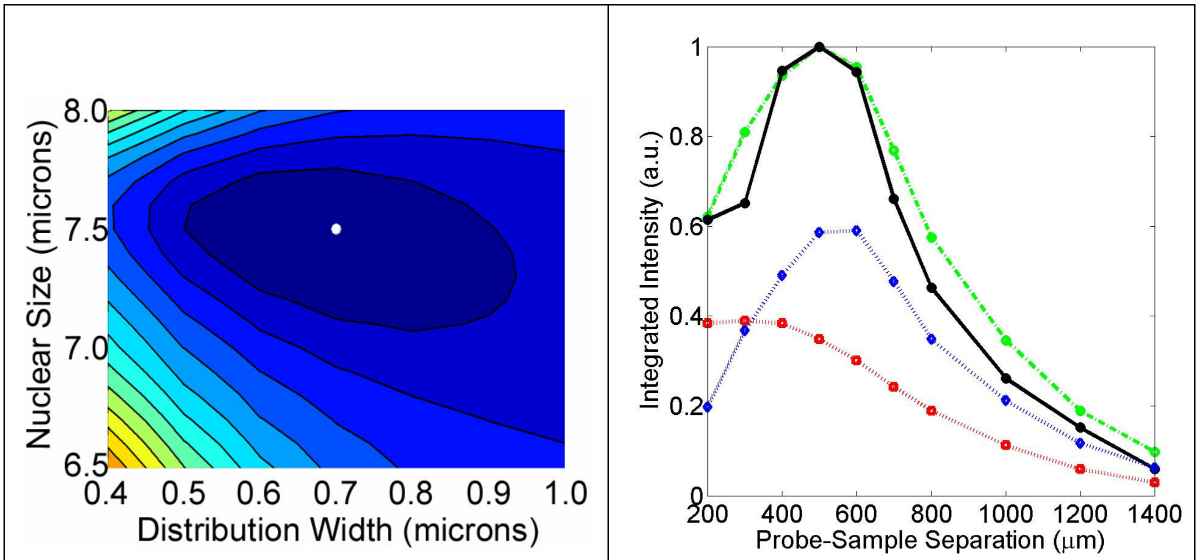

(a)

(b)

Figure 3.13: (a) Contour plot of the sum square error of the fit for the morphologically important parameters of nuclear size and nuclear size distribution. A single distinct minimum is shown as a small white circle. The extracted average nuclear size and nuclear size distribution is 7.5 μm and 0.7 μm, respectively. (b) Dependence of the total integrated forward scattering signal from cells on probe-sample separation: integrated forward scattering signal from SiHa obtained from experimental depolarization ratio spectra (solid curve) and theoretically predicted curve (dash-dot-circles curve). The theoretical curve was obtained using a linear combination of scattering from two sources: the cell/collagen interface (dot-diamonds curve) and scattering from the lower collagen layer (dot-squares curve).

To evaluate the proposed probe design for *in vivo* measurements, the oral mucosa was studied in a group of 6 normal volunteers at The University of Texas at Austin. Three sites in the oral cavity were measured for each volunteer: inner lip, left buccal mucosa, and right buccal mucosa. Figure 3.14 (a) shows an example of one of the measurements and the corresponding fit. Figure 3.14 (b) shows the average nuclear

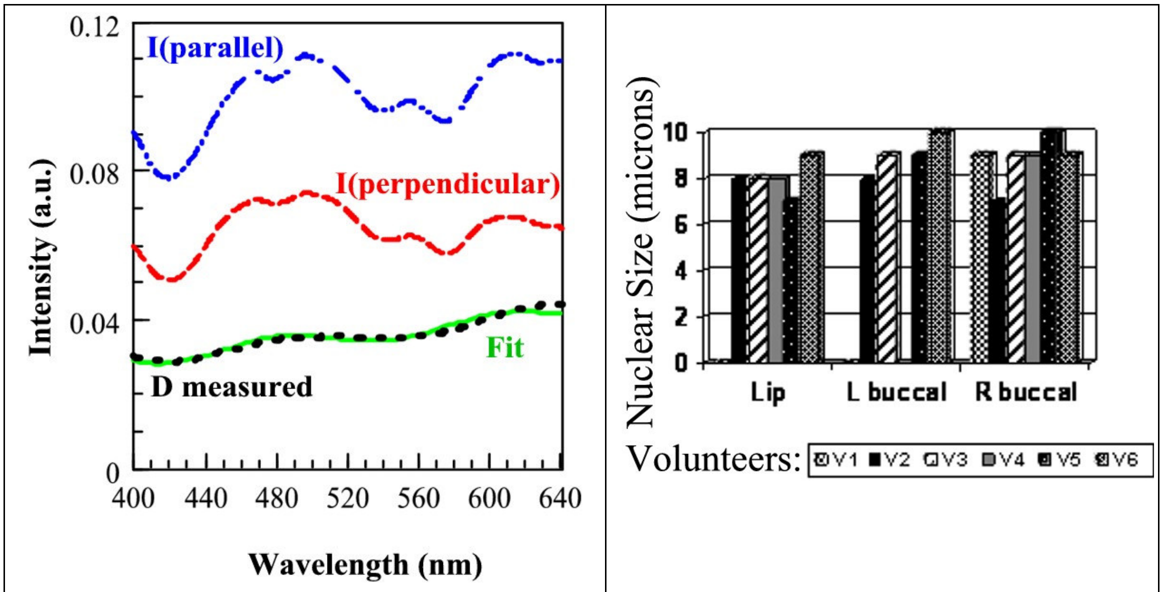

(a)

(b)

Figure 3.14: *In vivo* polarized reflectance measurements: (a) experimental depolarization ratio spectrum (dotted curve), corresponding fit (solid curve), and parallel (dash-dot-dot curve) and perpendicular (dashed curve) spectra obtained from a normal volunteer. (b) Bar graph of nuclear sizes calculated for 6 normal volunteers. Three sites within the oral cavity were measured for each volunteer: lower lip, right buccal, and left buccal mucosa. The average nuclear size calculated for all sites is 8.6 μm.

diameters extracted from the fitting of the depolarization ratio curves. A total of eighteen sites were measured. Three measurements that had very low signal intensity were discarded. The low intensity observed in these measurements was attributed to improper positioning of the fiber probe relative to the tissue. The average nuclear size for all sites measured was 8.6 µm, which corresponded well with a literature value of 8.9 µm obtained for oral epithelium using *in vivo* confocal reflectance microscopy [90]. These results are very promising, because both types of measurements were performed *in vivo* and, therefore, are not subject to potential changes that can occur during tissue removal and fixation associated with histological characterization.

3.8 DISCUSSION

The performance of the new fiber probe design was evaluated using an integrated approach that combines well defined tissue phantoms and theoretical modeling. The first phantom was composed of polystyrene beads embedded in collagen atop a collagen matrix (Fig. 3.5). In this model, the backscattering component contributes significantly to the collected scattering due to the large relative refractive index of beads inside collagen (1.59/1.35). Therefore, this phantom is an ideal model for studying the collection of backscattering events using the proposed fiber probe design. The results demonstrate that the probe is capable of optical sectioning the phantom (Fig. 3.11). Theoretical simulations showed that the maximum integrated backscattered signal detected from the bead layer corresponds to the maximum overlap between the illumination/collection acceptance cones within the bead layer. The FWHM of the dependence of the normalized backscattering intensity of the bead layer on probe-sample separation is approximately 600 µm (Fig. 3.11). This width corresponds well to the axial sampling distance of ca. 560 µm of the fiber probe (Fig. 3.4). However, it is larger than the actual thickness of the bead layer, which is ca. 330 µm. The axial resolution of the probe can be drastically reduced by decreasing the diameter of the fibers, their NA, and the separation between the collection and illumination fibers. For example, using 100 µm core diameter fibers with 0.12 NA would give an axial extent of overlap between collection and illumination acceptance cones of approximately 150 µm, which is less than the thickness of squamous epithelial tissue in the oral cavity or cervix.

Next, a tissue construct consisting of multiple layers of densely packed cervical cancer cells atop a collagen I matrix (Fig. 3.6) was examined. Analysis of depolarization ratio spectra obtained from the tissue constructs showed that nuclear scattering is dominated by the forward component. The nuclear sizes obtained from Mie theory calculations (7.5 ± 0.7 µm) agreed very well with independent measurements of nuclear diameters using microscopic measurements (7.9 ± 0.7 µm). These results demonstrate that nuclear sizes can be accurately extracted using the proposed fiber probe geometry.

It was also demonstrated that mean nuclear diameters can be obtained from analysis of *in vivo* polarized reflectance measurements. However, size distribution of nuclear diameters, which was reliably obtained in the case of cellular tissue constructs, was not consistently retrieved from *in vivo* polarized reflectance measurements. I believe that this problem is associated with a small amount of residual hemoglobin absorption that is sometimes present in the depolarization ratio spectra. This residual hemoglobin can be seen as small dips around 420 and 550 nm in the depolarization ratio curve shown in Fig. 3.14 (a). The source of this residual hemoglobin is most likely due to light that reaches capillaries in the stromal layer and is scattered back toward the surface before its polarization is randomized. It is known that for cells to survive and to be metabolically active they must be within approximately 100 μm from a blood supply. Therefore, small blood vessels are present within the first 100 μm beneath the basal epithelial layer. Preserving the original polarization allows this portion of the light to remain in the depolarization ratio spectrum. This problem can be solved by two approaches: (1) optimizing probe design to minimize the overlap between the collection acceptance cones and the stromal layer, and (2) incorporating the hemoglobin absorption into the model describing the depolarization ratio spectra. Currently, both solutions are being explored.

The results presented in this chapter suggest that the distal geometry of the proposed fiber probe can be tailored to preferentially to detect forward or backward scattering events within the epithelial layer or backscattering from the stromal layer. Confining the overlap of the illumination and collection acceptance cones within the epithelial layer will result in predominant collection of nuclear backscattering, whereas centering the overlap at the epithelium/stroma interface will preferentially probe the forward nuclear scattering component. Forward and backward scattering components can potentially provide complimentary information about nuclear morphology of epithelial cells. It has been shown that forward scattering is sensitive to scattering from large cellular organelles such as whole cell nuclei, [32-35, 92] whereas, backward scattering is more sensitive to scattering from smaller particles and the heterogeneity within larger organelles [33, 34, 40-42]. Increased nuclear heterogeneity and increased nuclear chromatin content are also very important indicators of earlier premalignant changes [93].

Moreover, there is a growing body of evidence showing significant optical changes occurring in the stromal layer at the earliest stages of carcinogenesis [18-20]. These changes occur as a result of dynamic communication processes between the epithelium and stroma [84, 85]. Focusing the overlap area of illumination/collection acceptance cones under the boundary of the epithelial and stromal layers would result in predominant collection of stromal scattering that would be modified by blood absorption. Scattering and absorption components can be separated using physical models of tissue scattering similar to an approach described by Zonios, *et al.*[51]. This scattering component could provide diagnostically useful information about stromal morphology such as density of collagen fibers and the changes in blood absorption that are related to angiogenesis.

The possibility to obtain diagnostically useful morphologic information from different areas within epithelium and underlying connective tissues suggests new multiple fiber probe designs that can potentially simultaneously probe epithelium and stroma at different depths. This can be achieved by using a single illumination fiber and multiple collection fibers with overlap areas of illumination/collection cones at different levels within epithelial and stromal layers. Simultaneous collection of morphologic information at different depths within tissue would allow a more accurate diagnosis of disease progression noninvasively.

3.9 SUMMARY

In this chapter I have shown the design and construction of a fiber optic probe that is capable of selective collection of scattered light from a target region within tissue. The design combines the principles of polarized illumination/detection and a tilted collection fiber geometry to isolate single scattering events at a targeted depth within epithelial tissue in the presence of a large diffuse background that usually originates from the stromal layer. To evaluate the performance of the new fiber design, an integrated approach that combines engineered tissue phantoms and theoretical simulations was implemented. It was demonstrated that the probe is capable of collecting backscattering events at a selected depth within a two-layer tissue model consisting of polystyrene beads atop a collagen matrix. Also in this chapter, the mechanism for detection of forward scattering of epithelial cells using a backscattering probe geometry was proposed and evaluated. It was suggested how the results of these studies could be used in development of endoscopic fiber probe based optical approaches for earlier detection of epithelial precancers.

3.10 ACKNOWLEDGEMENTS

Financial support from the Whitaker Foundation is gratefully acknowledged.

CHAPTER 4

Clinical Pilot Study

4.1 INTRODUCTION

Elastic scattering spectroscopy is sensitive to scatterer size, refractive index, and other morphological cell features. A promising application of this optical technique is the noninvasive detection and monitoring of precancers. Elastic scattering spectroscopy combined with polarized illumination and detection (polarized reflectance spectroscopy) allows selective probing of the epithelial layer of tissue, where most cancers originate. Separation of the epithelial signal from the stromal signal is an important step toward disentangling the wealth of information contained within a scattering spectrum. The stromal signal contains information primarily on collagen structure and oxygen content within hemoglobin found in stromal capillaries, whereas the epithelial signal contains information on cell morphology such as nuclear size, a key precancer diagnostic indicator. Polarized reflectance spectroscopy has the potential to provide clinicians with a non-invasive, real-time *in vivo* morphological analysis that can be extended to many other organ sites.

In this chapter, I present the results of a pilot clinical trial in collaboration with The University of Texas M.D. Anderson Cancer Center, Department of Head and Neck Surgery. The goal of this pilot clinical study was to determine the feasibility of polarized reflectance spectroscopy as a tool for non-invasive detection of early precancerous changes. The results of this study show that a polarized reflectance spectroscopic approach can effectively discriminate normal and severe dysplasia within the oral cavity and dramatically reduce the number of unnecessary biopsies, the associated health care cost, and the number of follow-up visits.

4.2 METHODS

4.2.1 Clinical Measurement

This pilot clinical study was conducted on 21 patients over the age of 18 that were referred to the Head and Neck clinic at MD Anderson Cancer Center with oral mucosa lesions suspicious for dysplasia or carcinoma. Informed consent was obtained from the participating patient, indicating that the patient was aware of the nature of the pilot clinical study. A standard oral cavity examination was performed by a medical doctor. Spectroscopic measurements were performed on 1 – 2 abnormal sites and 1 normal site. Biopsies were taken of all measured sites. The biopsied tissue was sectioned into 4 micron transverse slices and mounted onto microscope slides. The microscope slides were divided into two groups: 1.) slides prepared with a hematoxylin and eosin (H& E) stain for histological analysis, and 2.) slides prepared with a Feulgen-thionin stain that binds stoichiometrically to deoxyribonucleic acid (DNA) for quantitative histopathology [94, 95]. Paired normal and abnormal slides from group 1 were reviewed by a pathologist at MD Anderson Cancer Center. Detailed descriptions were made of each slide indicating the extent of dysplasia, inflammation, keratinization, and hyperplasia. Paired normal and abnormal slides from group 2 were sent to collaborators at the

Department of Cancer Imaging, British Columbia Cancer Center in Vancouver, Canada. Regions with the worst diagnosis were imaged and analyzed using their semi-automatic in-house image analysis system [95]. Nuclear segmentation was automatically carried out and nuclear feature statistics were subsequently calculated.

4.2.2 Instrumentation

The instrumentation used for the pilot clinical trial was the same as that used in Chapter 3. The schematic for the polarized reflectance spectroscopy instrument is shown in Figure 3.8. A picture of the instrument and fiber optic probe is shown in Figure 4.1.

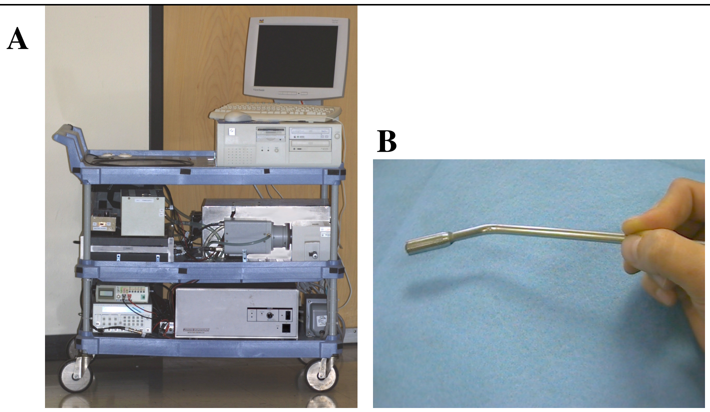

Figure 4.1: A.) Picture of the polarized reflectance spectroscopy instrument used for pilot clinical studies. B.) Distal end of fiber optic probe.

The instrument is compact and portable for transportation to the Head and Neck Clinic and to the operating room. The distal end of the fiber optic probe was also compact and angled to allow access and visualization of lesions.

4.2.3 *Monte Carlo Modeling*

The results of the pilot clinical trial were compared to a three dimensional Monte Carlo (MC) model of carcinogenesis, that is comprised of three layers: 1.) a semi-infinite epithelial layer, 2.) a semi-infinite precancerous layer, and 3.) a semi-infinite stromal layer with a fixed thickness of 5 cm. Figure 4.2 illustrates the concept for the MC model, where the precancer layer thickness is varied from zero to the full thickness of the epithelium. The combined thickness of the epithelium and precancer layer is held constant at 300 microns. This model is consistent with the development of precancer, where germinative cells at the basement membrane excessively proliferate upward toward the tissue surface [10]. The amount of epithelium that these undifferentiated cells cover is used in the staging of precancer [10].

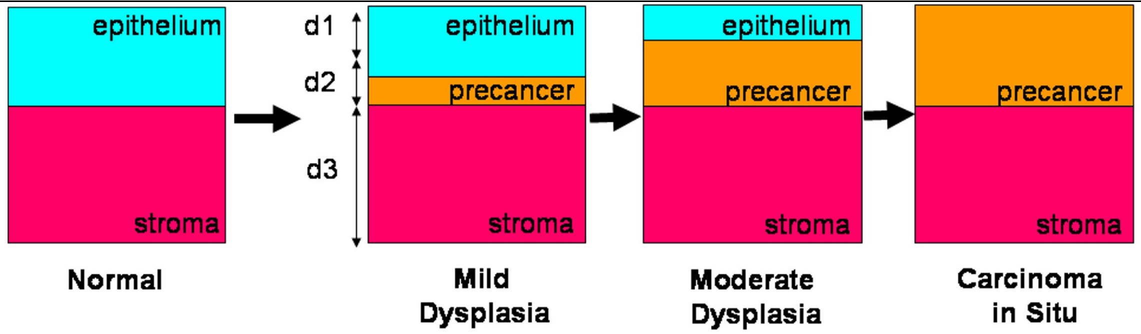

D = d1 + d2
D = 300 microns

d2 = D – d1
d3 = constant

Figure 4.2: Monte Carlo modeling of dysplasia.

The values for the optical parameters used in the MC calculation are shown in Table 4.1. All values are taken at 550 nm. The scattering coefficient of normal and precancerous epithelium, and normal and cancerous stroma was taken from the literature [20, 29, 38, 92]. Previously, it was believed that precancerous changes occur only at the epithelial layer of tissue, however, growing evidence suggests that there are simultaneous changes in the optical properties of both the epithelium and stroma with dysplasia due to biochemical communication processes [18-20, 29]. The scattering coefficient of stroma for mild dysplasia and moderate dysplasia was obtained by assuming a linear decrease in the scattering coefficient from published values of normal tissue to published values of carcinoma in situ [20, 29], then extrapolating the scattering coefficient for mild dysplasia and moderate dysplasia given that mild dysplasia encompasses one-third of the epithelial thickness, and moderate dysplasia encompasses two-thirds of the epithelial thickness, as shown in Figure 4.2.

Layer	*g*	μ_a (cm^{-1})	*Thickness (cm)*	***Normal*** μ_s (cm^{-1})	***Mild Dysplasia*** μ_s (cm^{-1})	***Moderate Dysplasia*** μ_s (cm^{-1})	***Carcinoma in Situ*** μ_s (cm^{-1})
Epithelium	0.95	1.60*	d1	32.4	32.4	32.4	-
Precancer	0.95	1.60*	d2	-	83.1	83.1	83.1
Stroma	0.88	1.61†	5	200.0	176.9	153.8	130.0

Table 4.1: Optical parameter values used in the Monte Carlo model of carcinogenesis. All values are taken at 550 nm. *g* = anisotropy factor, μ_a = absorption coefficient, d1 = epithelial thickness (varies from 0 – 300 μm), d2 = precancer thickness (varies from 0 – 300 μm), μ_s = scattering coefficient.

---

* μ_a for epithelium includes contributions from chromophores NADH and FAD

† μ_a for stroma includes contributions from collagen cross-links, but neglects hemoglobin contribution

In the MC model, the number of scattering events and depth at which photons interact with tissue was tracked. Using this information, and by making simple assumptions about the polarization state of photons, the total detected co-polarized and cross-polarized photons can be estimated and compared to clinical measurements. First, it is assumed that photons that have scattering events in the epithelium will retain the initial polarization. This is a reasonable assumption if one considers that the mean free path for scattering, $1/\mu_s$, is approximately 120 - 300 μm for epithelium, and that the typical thickness of oral epithelium is also 300 μm. Therefore, we can safely assume that photons traversing normal or precancerous epithelium will undergo 1 – 2 scattering events. It has been shown by Myakov that a few scattering events do not significantly alter the polarization state of photons for a fiber optic probe design in which all the fibers are parallel to each other [37]. This calculation was repeated for the angled fiber geometry used in the pilot clinical trial. The polarization ratio is calculated according to the following equation:

$$P = \frac{I_{\parallel} - I_{\perp}}{I_{\parallel} + I_{\perp}} = -\frac{S_{12}}{S_{11}} \tag{4.1}$$

where S_{12} and S_{11} are the scattered field amplitudes, given in Chapter 2, equation (2.24). If P is positive, then the scattered polarization is parallel to the incident polarization. If P is negative, then the scattered polarization is perpendicular to the incident polarization.

The results, shown in Figure 4.3, indicate that the mean change in polarization for a single scattering event for the angular range of our probe is 2.26 % for backward scattering (theta = 137 – 150 degrees, phi = 0 – 9 degrees), and 1.71 % for forward scattering (theta = 0 – 9 degrees, phi = 0 – 9 degrees). Thus, we can assume that scattering in the epithelium does not significantly alter the original polarization state.

In the stromal layer, the situation is very different as the stroma composition differs from epithelium. Stroma is comprised primarily of structural proteins and collagen fibers. The scattering coefficient of stroma is approximately ten times greater than that of epithelium. As a result, photons within the stroma will undergo many more interactions. The angular polarization change can be viewed as a diffusion process where depolarization increases with increasing optical depth [55]. ,

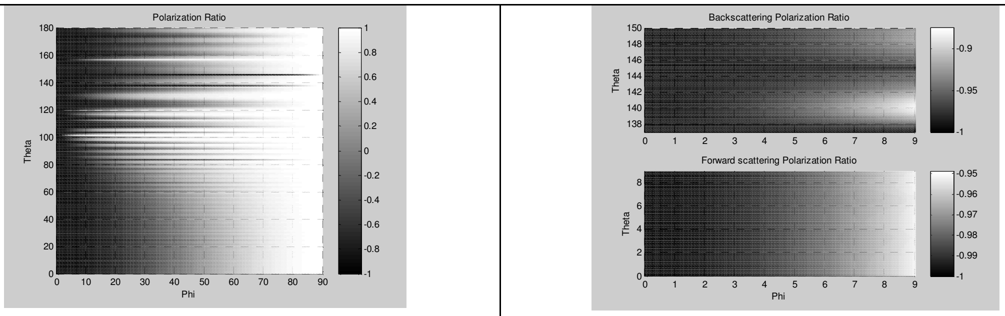

A

B

Figure 4.3: Mie theory calculations of polarization change after a single scattering event. A.) Contour plot of the polarized ratio as a function of the polar angle, theta, and the azimuthal angle, phi. B.) Contour plot of polarization ratio for the forward and backward scattering intensities for the theta and phi angles of our fiber optic probe. The mean polarization change in the backward direction was -0.9774, and the mean change in the forward direction was -0.9829.

Within mucosal tissue the main component of stroma are collagen fibers and its cross-links, which are randomly oriented and birefringent, adding to their ability to depolarize light [96]. In the MC model used here, all photons having two or more scattering events within the stroma are assumed to be depolarized. This assumption is consistent with recent findings by Kim which show that spherical polystyrene beads can depolarize light after only two scattering events [80]. Additionally, the birefringent collagen fibers in stroma are expected to depolarize light more efficiently than spheres, further supporting our assumption that two or more scattering events within the stroma are sufficient to completely depolarize light.

The MC results presented in this chapter are an average of three separate runs, each with 100,000,000 photons. The boundary between the epithelium, precancer layer, and stroma was index matched. Two separate cases were explored: 1.) the stroma scattering coefficient was fixed, while the precancerous layer thickness was increased, and 2.) the stroma scattering coefficient was decreased with increasing precancer thickness.

4.3 RESULTS AND DISCUSSION

Table 4.2 summarizes the distribution of sites from the oral cavity that were measured, then subsequently biopsied. A total of 21 patients and 44 sites were measured. Nine sites from 3 different patients were removed from the analysis because of improper handling of the fiber optic probe or malfunctioning of the clinical device. Table 4.2 is divided into two categories based on the clinician’s visual impression at the time of biopsy: (1) Normal, (2) Abnormal. The clinically appearing "abnormals" are further subdivided into three categories according to their histological diagnosis: (2a) Normal (A/HN) - sites that were classified as abnormal during visual examination, but were diagnosed as histologically normal (A/HN), (2b) Mild dysplasia and (2c) Severe dysplasia.

	Clinical Appearance		**Diagnosis for Abnormals**		
Location	**Normal**	**Abnormal**	**Normal (A/HN)**	**Mild Dysplasia**	**Severe Dysplasia**
Tongue	7	11	5	4	2
Buccal	13	6	3	3	0
Floor of Mouth	0	3	0	2	1
Gingiva	1	2	1	0	1
Soft Palate	1	1	1	0	0
Total measured	22	23	10	9	4
Excluded from study	4	6	1	4	1
Total used in analysis	**18**	**17**	**9**	**5**	**3**

Table 4.2: Biopsy site distribution. This table is divided into two categories according to visual impression at the time of biopsy: (1) Normal clinical appearance, (2) Abnormal clinical appearance. The abnormals are subdivided according to their histological diagnosis: (2a) Normal, (2b) Mild dysplasia, (2c) Severe dysplasia.

Nuclear sizes were extracted from the fits to the depolarization ratio spectra, using the Mie theory based algorithm described in Chapter 3. In Figure 4.4, the mean nuclear diameters extracted from spectroscopic measurements for each diagnostic category are compared with results from quantitative histopathologic analysis. As expected, nuclear size increases with dysplasia. The spectroscopic measurements for nuclear size give slightly lower values than quantitative histology. The difference arises because the nuclear sizes obtained from quantitative histopathogy are direct measurements of nuclei in epithelium, whereas polarized reflectance spectroscopy measurements are indirect volume averaged measurements of scatterer size

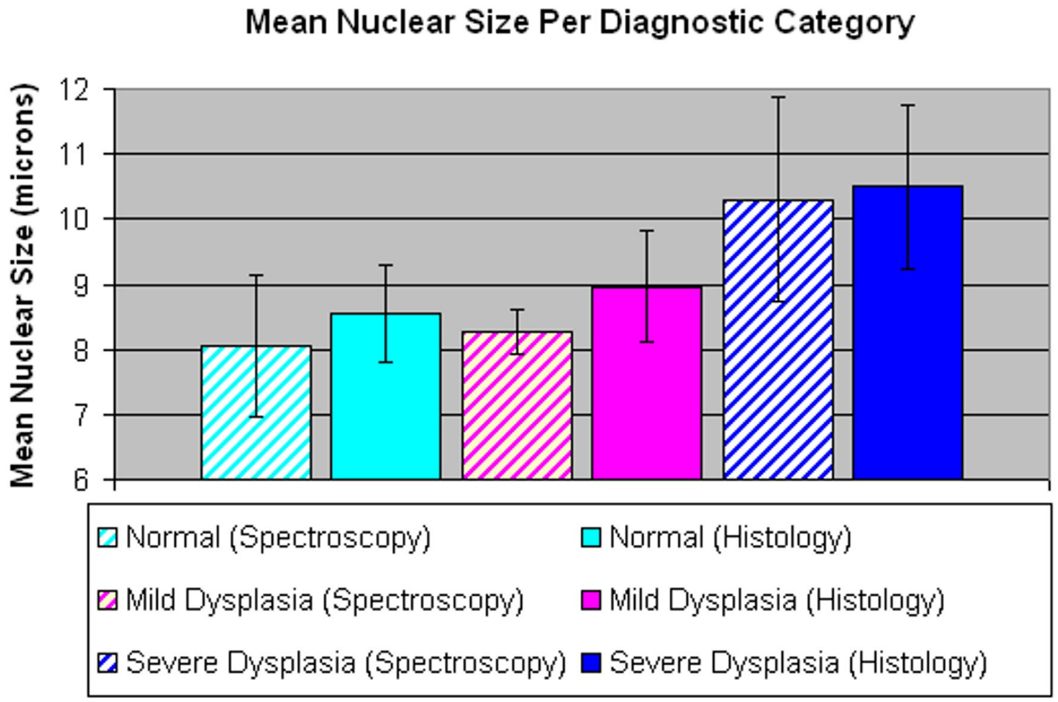

Figure 4.4: Mean nuclear size per diagnostic category.

. Therefore many smaller structures such as inflammatory cells, which are commonly found in benign and cancerous tissue, can influence the extracted "nuclear size," causing systematically smaller values to be measured.

Complete separation of normal tissue from severe dysplasia was found when the ratio of integrated intensity of the scattered light collected with polarizations parallel ($I_{//}$)

and perpendicular ($I_\perp$) to the incident beam was plotted against spectroscopically derived nuclear size. The data points shown in Figure 4.5 are from all measured sites within the oral cavity that include: buccal mucosa, tongue, gingiva, floor of mouth, and soft palate.

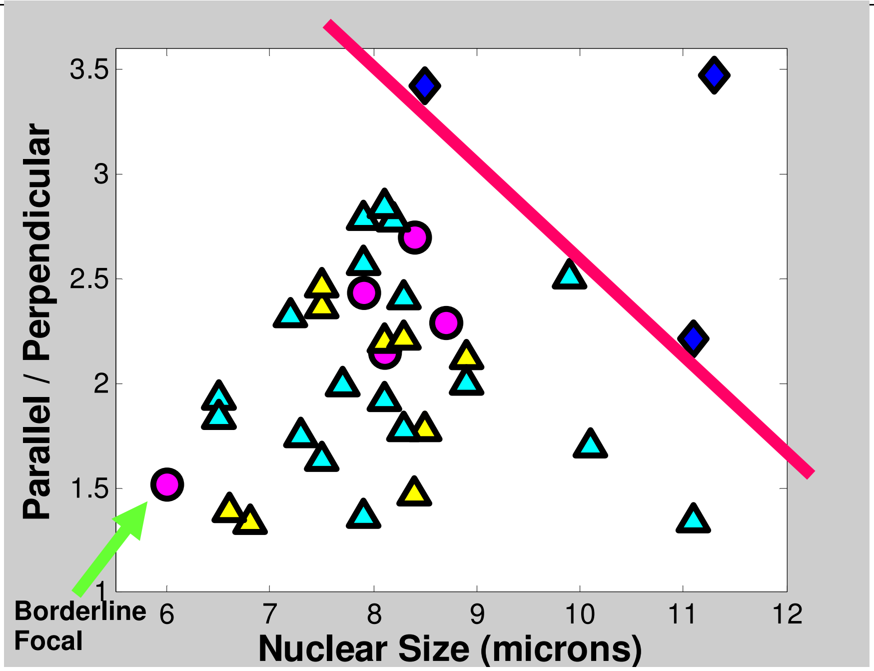

Figure 4.5: Binary decision plot to discrimate severe dysplasia from normal and mild dysplasia. The ratio of the integrated parallel to perpendicular intensity is shown as a function of nuclear size. Blue diamonds represent severe dysplasia, pink circles indicate mild dysplasia, yellow triangles indicate sites that appeared clinically abnormal, but were discovered to be normal by histopathology, and the light blue triangles represent normal measurements.

The points above the pink line are severe dysplasia, and those below are normal or mild dysplasia. All points that were misdiagnosed as abnormal during visual examination by a clinician (yellow triangles) and were later determined to be normal by histopathology, are correctly clustered with the normals (light blue triangles). Discrimination of severe dysplasia from normal and mild dysplasia is of important clinical interest, as the treatment for severe dysplasia is surgical removal. Detection of mild dysplasia is less critical than severe dysplasia. For low risk patients, mild dysplasia is not treated, but observed over time.

In Figure 4.5, all the mild dysplasias cluster together, except for an outlier indicated by the green arrow. When the tissue from this outlier was examined by a pathologist, the area of mild dysplasia was found to be very small and surrounded by normal tissue. It is very likely, then, that the spectroscopic measurement was actually on normal tissue. Focalization of abnormal tissue is an inherent problem with point probe techniques. Local abnormalities can potentially be missed for focal lesions that are less than or equal to 1 mm^2. This problem can be minimized by taking multiple measurements of the abnormal site. Between each measurement, the probe can be removed from the tissue, then placed back over the site of interest. For each measurement, the probe placement will be slightly offset. With multiple measurements, the probability of encompassing the abnormal region within the sampling volume increases.

The physical meaning of the parallel / perpendicular scattering intensity is clear if one considers the following equation:

$$\frac{I_{\parallel}}{I_{\perp}} = \frac{I_{\parallel} - I_{\perp}}{I_{\perp}} + 1 \tag{4.2}$$

where $I_{\parallel}$ is light collected with polarization parallel to the incident illumination, and $I_{\perp}$ is light collected with polarization perpendicular to the incident illumination. The term $I_{\parallel}$ contains "singly" scattered light from the epithelium, and half of the depolarized light from the stroma. The term $I_{\perp}$ contains the other half the depolarized light from the stroma. By subtracting these two quantities, the epithelial scattering signal can be isolated. So, the ratio $I_{\parallel} / I_{\perp}$ represents the ratio of epithelial to stromal scattering, plus a constant:

To further illustrate the general trend of increasing nuclear size and increasing parallel / perpendicular integrated scattering intensity with the progression of normal tissue to severe dysplasia, data points from the same diagnostic category shown in Figure 4.6, were averaged together and shown in Figure 4.5 The focal mild dysplasia data point was excluded in the averaging.

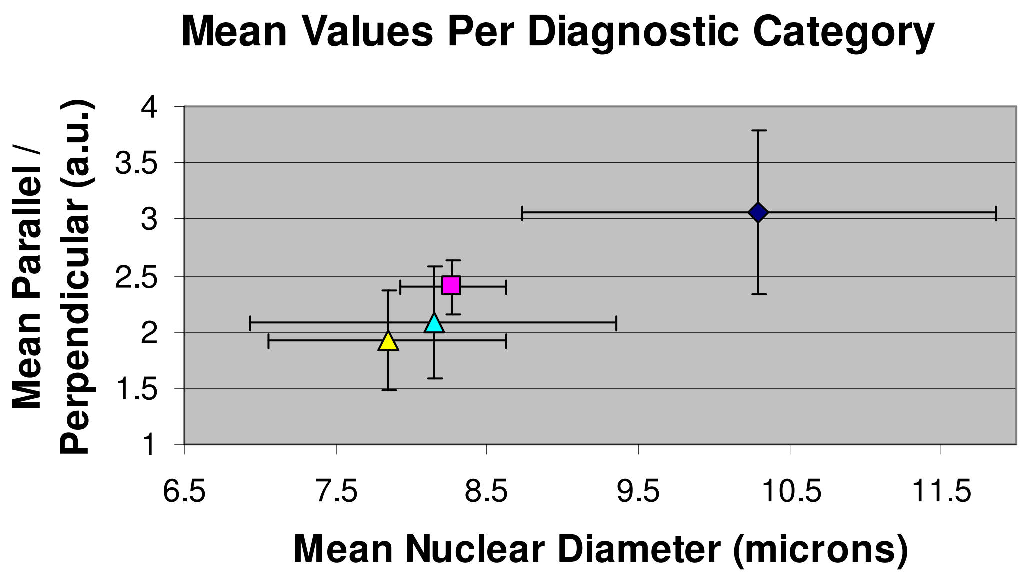

Figure 4.6: Mean values per diagnostic category for the measured values shown in Figure 4.5. Light blue triangle – clinically appearing normal, yellow triangle –normal (A/HN), pink square – mild dysplasia, blue diamond – severe dysplasia. This plot shows that there is a trend toward increasing nuclear size and increasing parallel / perpendicular integrated scattering intensity with dysplasia.

The clinical data shown in Figure 4.6 was compared to a Monte Carlo (MC) simulation of carcinogenesis, illustrated in Figure 4.2. Two cases were studied: 1.) the scattering coefficient of stroma remains constant, and 2.) the stroma coefficient decreases linearly with dysplasia. Figures 4.7 and 4.8 show the histograms of the MC output, which contain information on the number of photons collected and their maximum axial depth of penetration. Two categories are studied: 1.) single scattering and 2.) multiple

Single Scattering	**Multiple Scattering**
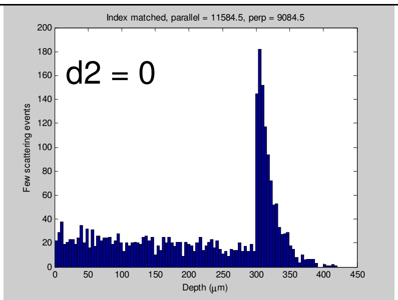	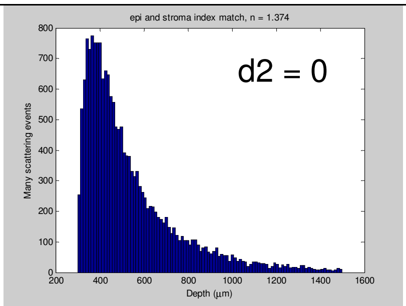
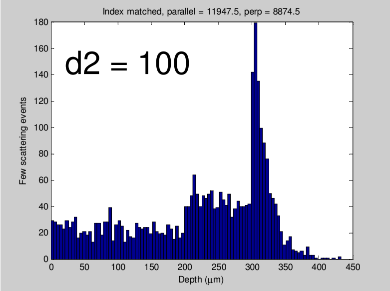	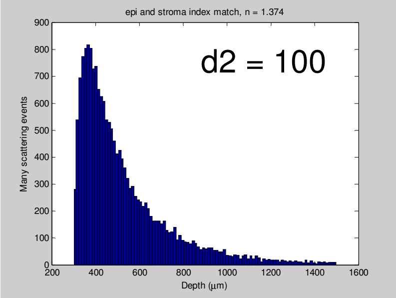
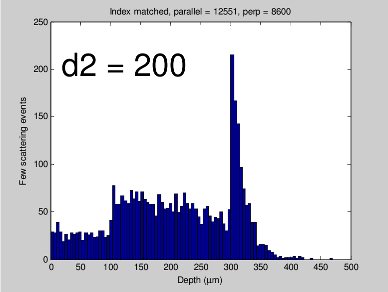	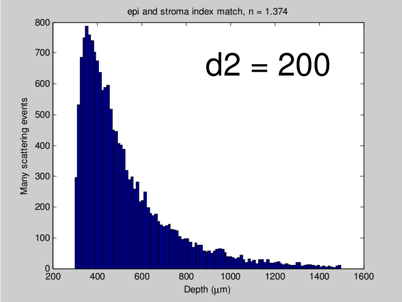
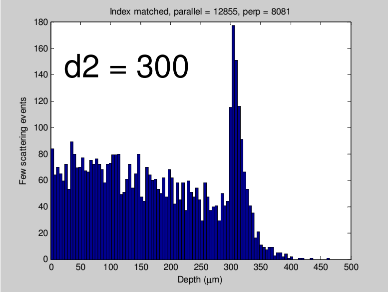	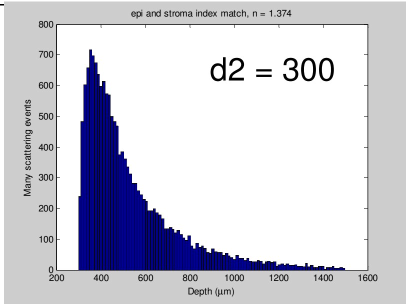

Figure 4.7: Output histograms to MC simulation for the case when the stroma scattering coefficient is held constant. Precancer layer thickness in microns is indicated by d2.

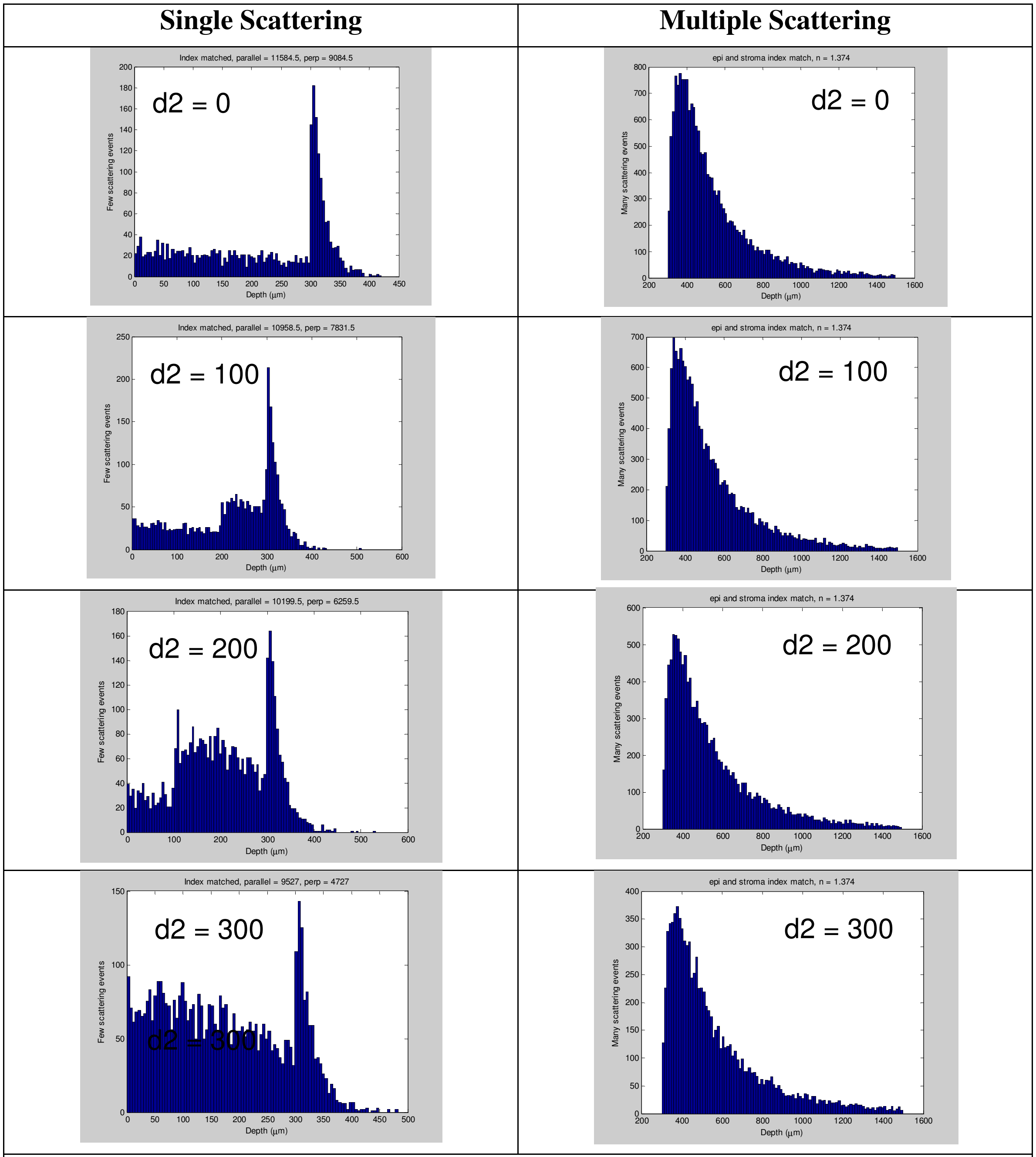

Figure 4.8: Output histograms to MC simulation for the case when the stroma scattering coefficient is decreased with increasing precancer layer thickness.

scattering. Single scattering was defined as photons that have had scattering interactions within the epithelium and precancer layer, and one or less scattering event in the stroma. Multiple scattering was defined by all other photons which have had epithelial and precancer layer scattering interactions, and multiple scattering interactions within the stroma.

The first column of Figures 4.7 and 4.8 clearly show the increase in the amount of singly scattered light with increasing precancer layer thickness. The large diffusive stromal signal, shown in the second column of Figures 4.7 and 4.8, illustrate the difficulty that traditional (unpolarized) reflectance spectroscopy encounter when attempting to isolate the epithelial signal.

Excellent agreement is found between the MC results to the clinical data, shown in Figure 4.9. The clinical data was normalized to the MC results at a precancer thickness equal to zero. The MC results suggest that the case where the stroma scattering coefficient is decreasing (red curve) more closely corresponds to the clinical data. The percentage increase of the parallel / perpendicular scattering signal is 58 % and 50 % for the MC model (stroma decreasing) and the experimental clinical data, respectively. These results lend weight to the hypothesis that there are concomitant changes in the stroma and epithelium with dysplasia.

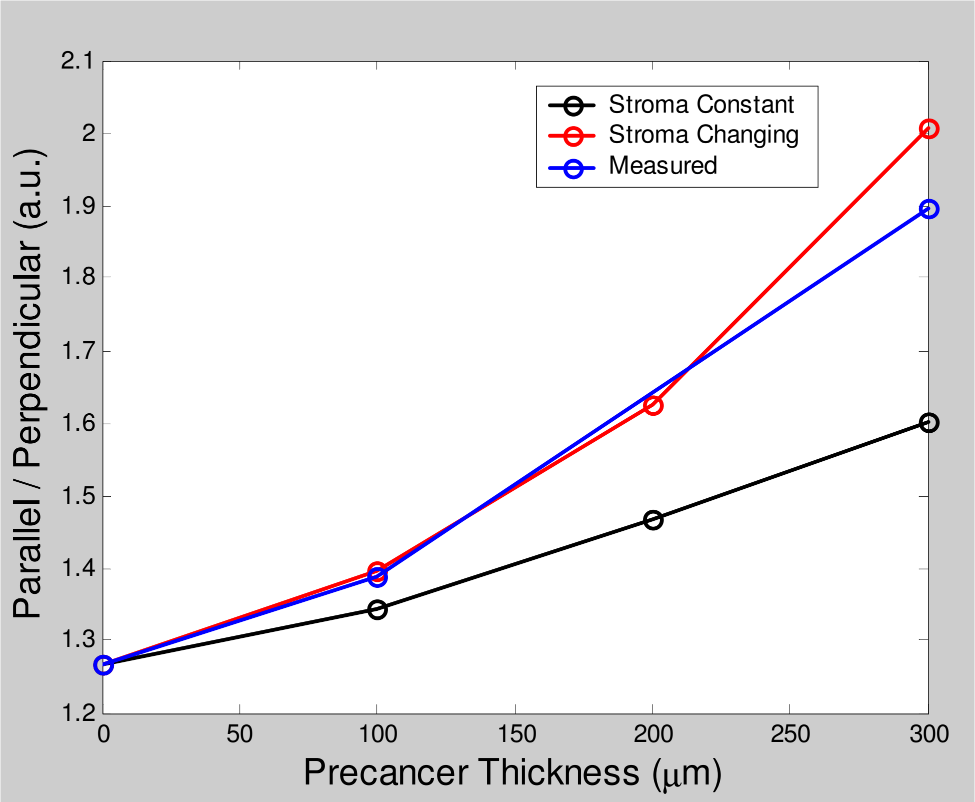

Figure 4.9: Comparison of MC modeling with pilot clinical measurements. The MC results for two models of carcinogenesis are shown: black curve – stromal scattering coefficient constant, red curve – stromal scattering coefficient decreasing with dysplasia. The experimental result for the pilot clinical study is shown as the blue curve.

The ability of polarized reflectance spectroscopy to discriminate normal tissue from severe dysplasia is remarkable, especially if one considers that the data includes inter-patient variability and that each of the measured tissue sites can exhibit very different tissue architecture. In addition, the lesions measured had varying degrees of hyperkeratinization, hyperplasia, and inflammation, which can complicate spectroscopic diagnosis [29].

4.4 SUMMARY

The results of this pilot clinical trial show that polarized reflectance spectroscopy can be used as a cost-effective and robust tool for identifying severe dysplasia for multiple sites within the oral cavity that is insensitive to patient to patient, and site to site variability. These promising results support future work to compare the sensitivity and specificity of polarized reflectance spectroscopy to existing diagnostic technologies in a large statistically significant clinical trial.

4.5 ACKNOWLEDGEMENTS

Many thanks to Dizem Arifler for use of her MC code. Financial support from Whitaker Foundation is gratefully acknowledged.

CHAPTER 5

Summary and Conclusions

5.1 SUMMARY OF RESULTS

The work in this dissertation focused on the assessment of polarized reflectance spectroscopy as a non-invasive optical tool to detect and diagnose precancerous lesions in the oral cavity. Such a tool would augment the gold standard of biopsy to diagnose precancerous lesions. For example, detection of cancerous lesions is complicated by tissue architecture variety within the mouth and by the numerous benign lesions that can be indistinguishable from cancer. Even for the most experienced clinicians, discrimination of severe dysplasia from benign lesions is difficult. A biopsy must be taken for a definitive diagnosis. However, biopsy is not an ideal solution when a large extent of the oral cavity is covered in lesions. This problem is also seen in the operating room during tissue excision, where the resection margin demarcating the boundary between normal and severe dysplasia is determined subjectively by palpation of the lesion. A more quantitative method for distinguishing normal tissue from severe dysplasia is needed to minimize the amount of tissue excised and to reduce the incidence of follow-up surgeries that are necessary when the extent of tumor is underestimated. Polarized reflectance spectroscopy also has the potential to be used as a monitoring method during the non-invasive treatment of precancerous lesions, where multiple biopsies are not feasible.

Chapter 3 demonstrated that the single scattering signal from the epithelium can be effectively separated from the diffuse stromal signal using a combination of polarized illumination / detection and a tilted collection fiber geometry, and that the singly scattered signal could be modeled using a Mie theory based model to extract epithelial nuclear size. Other approaches that separate the epithelial and stromal scattering signals are heavily model dependent. The approach presented in Chapter 3 permits this to be accomplished at the instrumentation level. The fiber optic probe presented in Chapter 3 was tested in multilayer bead and cell phantoms that mimicked the two-layer structure of epithelial tissue. In both cases the epithelial scattering signature could be isolated from the diffuse background signal originating in the stromal layer. In addition, the scatterer size and size distribution was accurately extracted using a Mie theory-based model. Polarized reflectance spectroscopy measurements were also taken in the oral cavity of normal volunteers. Extracted nuclear sizes corresponded well with literature values for normal oral mucosa using *in vivo* confocal reflectance microscopy.

Chapter 4 presents the results of a pilot clinical trial in the oral cavity conducted on 21 patients at the MD Anderson Cancer Center, Department of Head and Neck Surgery. Complete separation of severe dysplasia from normal and mild dysplasia was achieved using the combination of two parameters: 1.) the ratio of the integrated intensities for light collected with polarizations parallel and perpendicular to the incident illumination, and 2.) nuclear sizes obtained from fits to the depolarization ratio. The parallel / perpendicular scattering intensity represents the epithelial / stromal scattering signal. This ratio was found to increase with dysplasia, which is consistent with an increasing body of evidence that shows that epithelial scattering increases with dysplasia, whereas stromal signal decreases. The average values for nuclear sizes extracted from spectroscopic measurements obtained for each diagnostic category - normal, mild dysplasia, and severe dysplasia – corresponded with quantitative histology measurements of the same tissue site. The mean nuclear size for each diagnostic category was found to increase with dysplasia, as is seen in the literature.

The results of Chapters 3 and 4 provide very promising evidence for the use of polarized reflectance spectroscopy with an angled collection fiber geometry to detect and diagnose precancer. These results suggest that a more extensive clinical trial be conducted to determine the sensitivity and specificity of polarized reflectance spectroscopy so that this method can be compared to current diagnostic technologies. Further studies should also concentrate on improved probe design, elucidation of the scattering properties of the various substructures within cells, other than nuclei, and also improvements to the Mie theory based model to extract other morphological features such as nuclear density, nuclear to cytoplasmic ratio, and index of refraction. In the next section, I will outline some of these future projects.

5.2 FUTURE DIRECTIONS

5.2.1 New Fiber Optic Endoscope Design

Chapter 3 demonstrated that an angled collection fiber geometry could physically isolate the epithelial scattering signal by overlapping the illumination and collection cones within the first 300 μm of tissue. However, the axial extent of the overlap volume for the probe used in this dissertation work was fairly large, 560 μm – 600 μm. As a consequence, some residual stromal scattering remained in the depolarization ratio spectra. Improvement of this probe design would incorporate multiple 100 μm core fibers with 0.12 NA. This design is illustrated in Figure 5.1.

Using multiple small collection fibers permits more selective depth profiling to be performed. Signal from the superficial, intermediate, and basal layer of epithelium can be probed. It has been shown by Collier that the most diagnostically relevant region is the superficial epithelium [97]. Collection of the scattering signal from multiple depths would also correct for thickening of the epithelium, which is often exhibited by lesions, benign and precancerous. This approach will also provide more information on the relative contributions of forward and backward scattering as a function of axial depth. It has been shown that forward scatter is more sensitive to larger particle sizes, such as cell nuclei, whereas backscatter is more sensitive to smaller structures such as mitochondria and nuclear heterogeneity [32-35, 40-42, 68]. Recently, Arifler has shown using FDTD calculations that the scattering cross-sections of cells at different depth change with dysplasia [98]. The probe design in Figure 5.1 would give experimental evidence to support or contradict this finding.

With this geometry, a separate stromal profile could also be measured for each patient. This would greatly increase the sensitivity of the Mie theory based fitting model, which has a fixed stromal profile. Probing the stroma separately would allow study of the biochemical and structural changes that occur within the stroma with the progression of precancer.

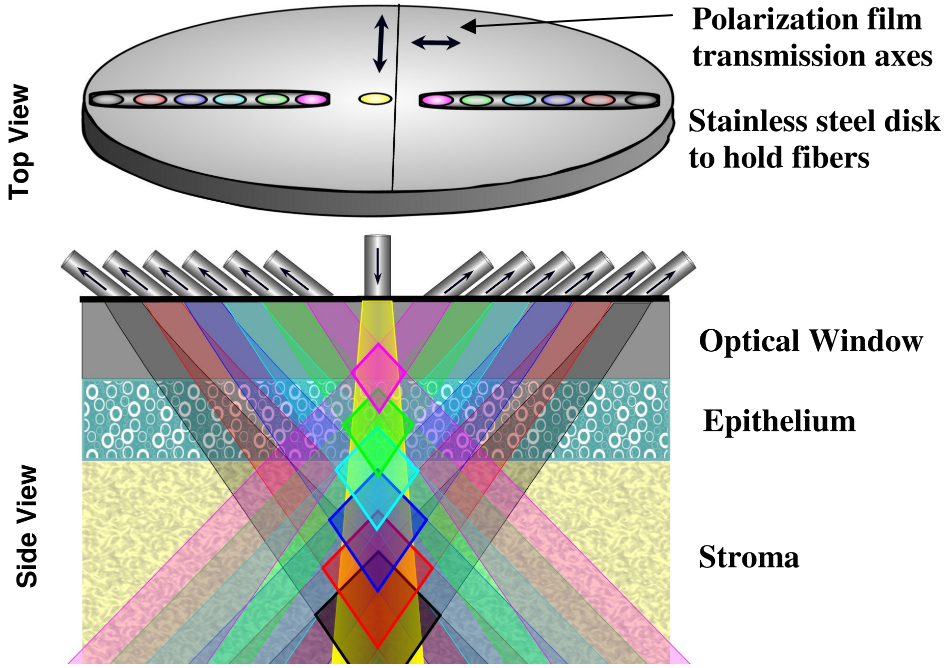

Figure 5.1: Schematic of new probe design. A central fiber delivers polarized light to tissue (middle fiber with yellow cone). Multiple fibers symmetrically placed on either side of illumination collect scattered light co-polarized and cross-polarized with respect to incident illumination.*

5.2.2 Hyperspectral Dark-Field Imaging

The great benefit and promise of elastic scattering spectroscopy is that it is a relatively simple technique for probing tissue morphology. However, the difficulty with such a wealth of information is in separating the various components. For example, epithelial tissue contains a large variety of structures such as cell nuclei, mitochondria, lysosomes, peroxisomes, and various proteins. The measured scattering spectra will contain information on all particles within the volume probed. The contribution of each

*Detailed AutoCad drawings of the new probe design are given the Appendix.

cellular substructure will not necessarily be proportional to its volume fraction within a cell. The question then naturally arises as to which of the various cellular components dominate the scattering spectrum. Future studies should attempt to separate the various scattering signatures from the subcellular components to establish a better understanding of the light scattering from these constituent parts. The results of these studies will further elucidate the elastic scattering spectra obtained *in vivo* from normal and precancerous lesions.

In the following sections I will detail the experimental procedure for studying the light scattering properties of cell and tissue using a hyperspectral darkfield imaging microscope. I will then present a few preliminary results on SQCC oral cancer cells, and tissue slices obtained from oral cavity biopsies.

5.2.2.1 Material and Methods

The hyperspectral imaging system is shown in Figure 5.2. It is composed of two major components: 1.) an upright Leica DM6000M microscope, and 2.) a SpectraCube imaging detector. The configuration of the microscope is unique in that it permits transmittance *and* reflected darkfield studies to be performed in addition to brightfield, phase contrast, and fluorescence. The SpectraCube imaging detector mounted on the Leica microscope permits monochrome images to be acquired that contain wavelength dependent intensity information at each pixel. The combination of the Leica DM6000M microscope with the SpectraCube imaging detector form a truly unique system in which the forward and backward scattering signals can be independently measured. This system was used in a preliminary study focusing on the scattering from cell suspensions and tissue slices, thus providing information on the scattering signatures from specific regions within tissue and cells.

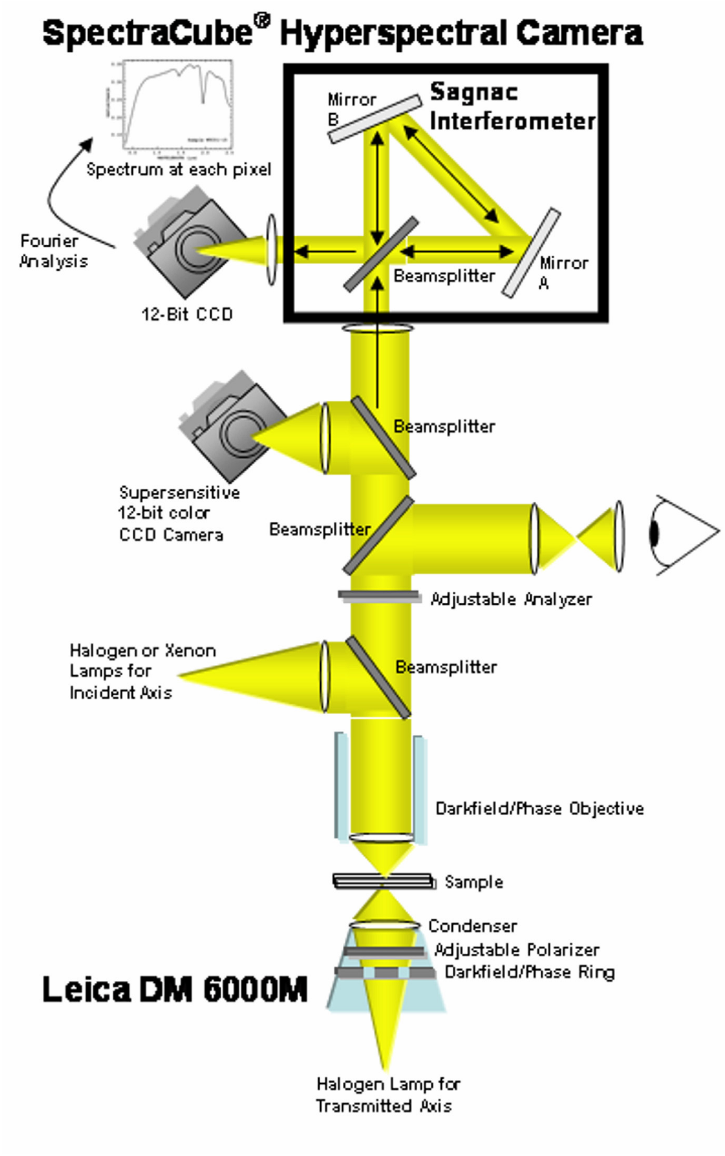

Figure 5.2: Diagram of hyperspectral imaging system. Consists of an inverted Leica DM6000M microscope and an Applied Spectral Imaging SpectraCube detector that is capable of hyperspectral imaging.

5.2.2.2 Hyperspectral SpectraCube Detector

The SpectraCube detector generates a spectrum at each pixel from hundreds of black and white images. Figure 5.3 illustrates the basic principle of operation of the SpectraCube detector. The hyperspectral detector head contains a Sagnac interferometer.

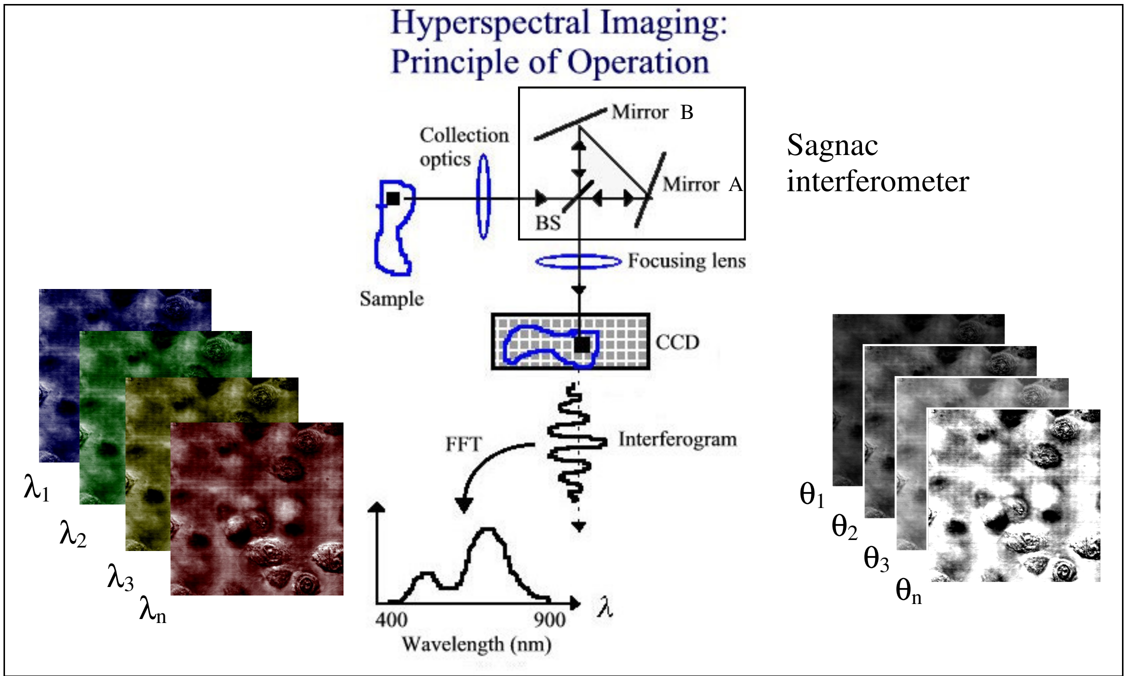

Figure 5.3: Schematic of the principle of operation for the SpectraCube imaging detector. Adapted from Applied Spectral Imaging.

Figure 5.4 shows the beam path within a Sagnac interferometer. The beam splitter (BS) splits the beam so that half the beam goes to Mirror A, and the other half is directed toward Mirror B. The two beams propagate the same path, but in opposite directions. In the modified Sagnac interferometer of the hyperspectral system, the BS is rotated in small angular increments causing the optical path length of the two beams to differ. When the two beams are combined, the intensity will be function of their optical path difference

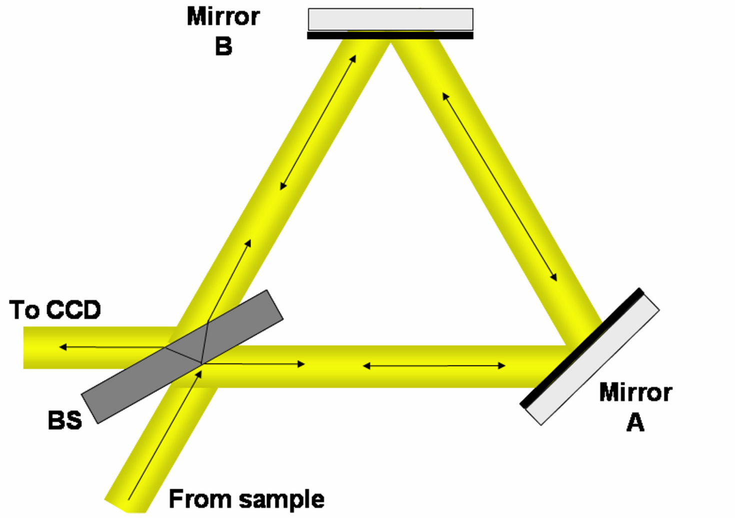

Figure 5.4: Beam path within a Sagnac interferometer.

(OPD). An interferogram image, or frame, is acquired at each angular position of the beamsplitter. After acquisition of all frames, a fast Fourier transform is performed to convert the stack of angle dependent interferograms into wavelength dependent images. The result is a stack of multiple images of the sample, where each image represents the scattering at a single wavelength.

5.2.2.3 Darkfield Microscopy

Darkfield microscopy (DF) is a great tool for observing scattering from small structures. Figure 5.5 illustrates the basic concept behind DF microscopy. Instead of illuminating a sample with a cone of light, as is traditionally done in brightfield microscopy, a hollow cone of light is used to illuminate the sample. The NA of the collection optics is typically 0.2 NA smaller than the illuminating optics. Thus, if there isn't a scattering sample in the illumination path, as in Figure 5.5 A, then no light will enter the collection optics. However, if the scattering sample is moved into the illumination focus, then light will be scattered into the collection optics, as shown in Figure 5.5 B. Figures 5.5 A and B illustrate transmittance DF. Figure 5.5 C is an illustration of reflectance DF. These objectives are larger than standard objectives to accommodate two light paths: an illumination path along the outer portion of the barrel, and a collection path along the central axis of the objective barrel.

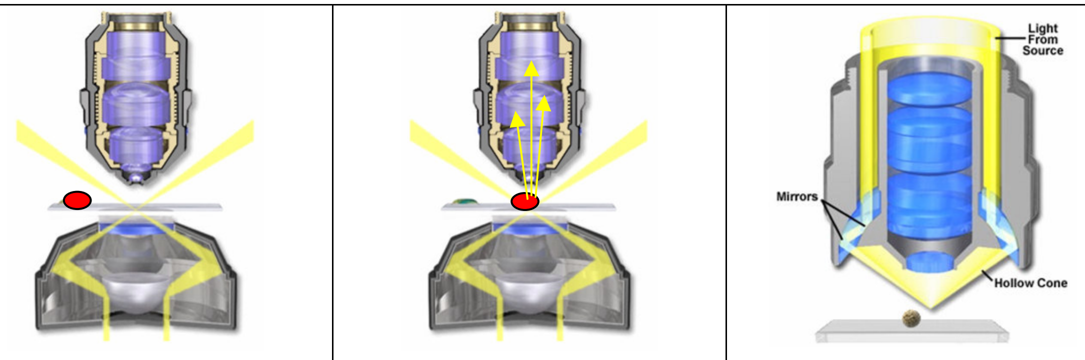

A **B** **C**

Figure 5.5: Illustration of darkfield microscopy. A.) transmittance DF, where the scattering sample is not in the illumination path. B.) transmittance DF, where the sample is in the illumination path, scattering photons up into the collection optics. C.) Schematic of a reflectance DF objective. Images adapted from ref. [9].

5.2.2.4 Preliminary Results – Oral Cancer Cells

In this section I will present some preliminary results using the darkfield hyperspectral imaging system. The first experiments were performed on a monolayer of SQCC/Y1 oral cancer cells grown on a coverslip. Figure 5.6 A is a phase contrast image of the cells. The bright cell boundaries are believed to be due to keratinization at the cell periphery. Cell nucleoli are clearly visible in this picture. Red arrows point to a nucleolus of interest. The increased scattering from smaller particles within cellular cytoplasm is clearly seen in the reflectance DF (RDF) image in Figure 5.6 B. The transmittance DF (TDF) shows less scattering from the cellular cytoplasm, but increased contrast of the nucleoli in Figure 5.6 C, and also in the hyperspectral images at 595.7 nm in Figure 5.6 D. The wavelength dependent scattering spectra were obtained from this nucleolus and are shown in Figure 5.6 E and F. The shape of the RDF spectrum is characteristic of smaller particles. Further studies would model the scattering spectrum to extract scatter size.

A. 40X Phase Contrast	B.) 50X Reflectance DF	C.) 50X Transmittance DF
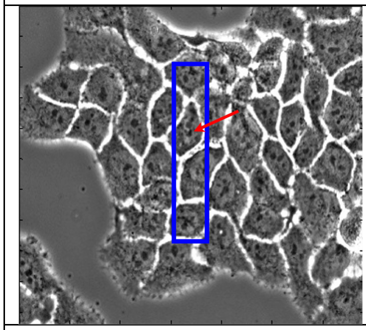	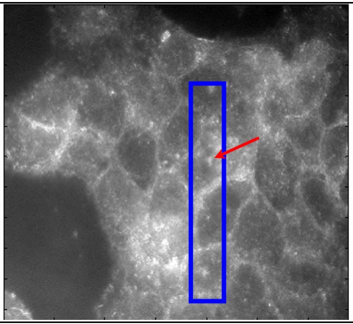	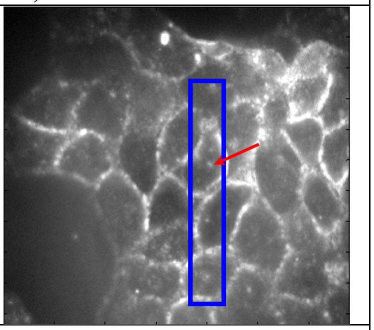
D.) Region of interest: phase (left), RDF (middle), TDF (right)	E.) RDF spectrum from nucelolus	F.) TDF spectrum from nucleolus
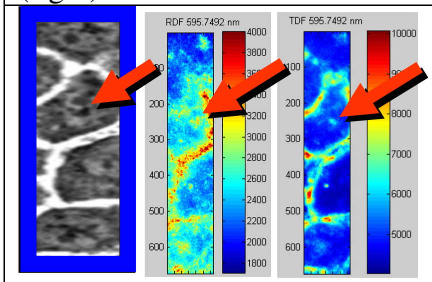	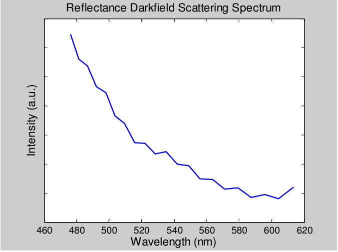	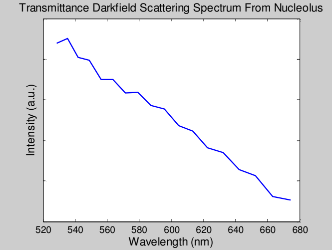

Figure 5.6: Hyperspectral DF images of a monolayer of SQCC/Y1 cells.

5.2.2.5 Preliminary Results – Human Tissue Slices

Images were also obtained on human tissue slices obtained from biopsied tissue that were taken at MD Anderson Cancer Center, Department of Head and Neck Surgery. The boundary between the epithelium and stroma is clearly seen in the phase, reflectance darfield (RDF), transmittance darkfield (TDF) images in Figure 5.7 A, B, and C.

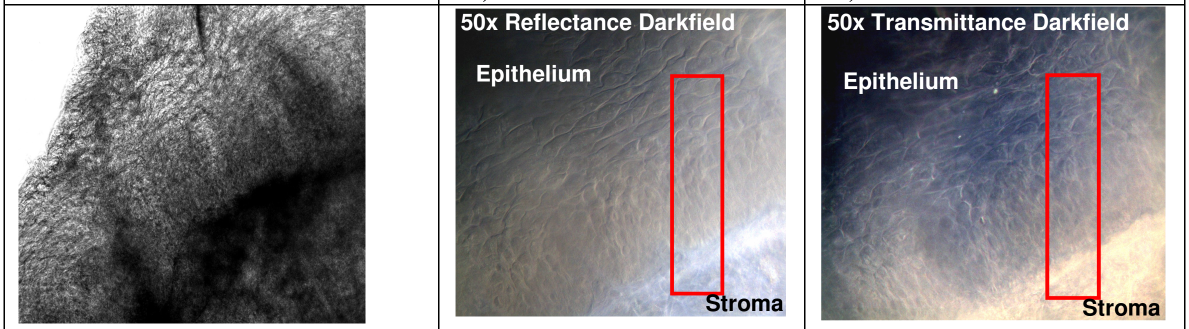

A. 40X Phase Contrast

B.) 50X Reflectance DF

C.) 50X Transmittance DF

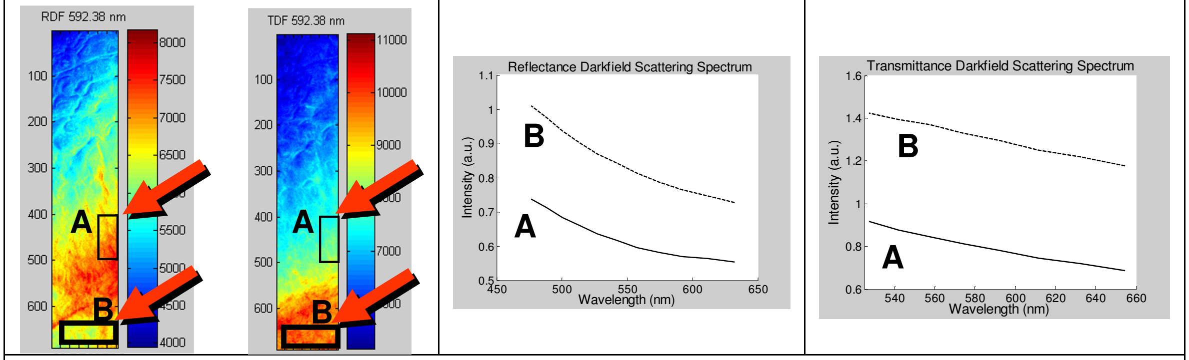

D.) Region of interest at 592 nm: RDF (left), TDF (right)

E.) RDF spectrum

F.) TDF spectrum

Figure 5.7: Hyperspectral DF images of a human tissue slice from the oral cavity.

Individual cell nuclei are clearly visible in the DF images. Scattering spectra were obtained from a region of interest, indicated by the red arrows. Two regions of interest were considered, a region in the epithelium (A), and a region in the stroma (B). The spectra show that stromal scattering is approximately 33 % and 56 % greater for RDF and TDF, respectively. This is consistent with the fact that the scattering coefficient of stroma is much larger than epithelium. Further studies would focus on the extraction of morphological information such as scatter size from the scattering spectra of tissue, and would incorporate the effects of polarized illumination and detection. Ultimately, a library of scattering spectra could be gathered with scattering information on specific cellular organelles. Cross-validation would be achieved by using targeted fluorescent labels. For example, MitroTracker® is a fluorescent dye that selectively stains mitochondria. MitoTracker® would be applied to a sample after scattering images are obtained. Then, by overlaying MitoTracker® images with darkfield hyperspectral images, unambiguous identification of mitochondria could be achieved. Similarly, chromatin within nuclei could be targeted with a DAPY fluorescent dye, and fluorescent dyes stoichiometric for collagen could be used to determine collagen scattering and density as a function of cancer progression.

5.3 CONCLUSIONS

In the studies included in this dissertation, the utility of a non-invasive optical method based on polarized light scattering spectroscopy was explored. *In vitro* and *in vivo* measurements demonstrated that this method could be used to extract nuclear morphology using a simple analytic model based on Mie theory. Pilot clinical results demonstrated that this method could be extended to the clinical environment to detect and diagnose severe dysplasia. The system is compact, robust, portable, and relatively inexpensive to construct, making it ideally suited for clinical use. Collection of scattered light with polarizations parallel and perpendicular to the incident illumination was found to be critical for detection of severe dysplasia. This contrasts with traditional reflectance techniques that do not utilize polarization.

Future work would include further development of the scattering model to include the changing stroma scattering signal with precancer progression. As mentioned earlier, collagen specific dyes can be used to quantify the collagen scattering and density within tissue of varying degrees of dysplasia. New probe designs can also aid the study of stromal scattering by improving the separation of epithelial and scattering signals, allowing each to be studied independently.

Further work to the scattering model would include information from polarization MC, where the polarization of a photon is monitored as it traverses tissue, and from Finite Difference Time Domain (FDTD) simulations, which can be used to study the effects of increased heterogeneity and increased chromatin content within nuclei. Parallel experimental studies can be performed with hyperspectral darkfield measurements of DAPY fluorescently labeled tissue which will selectively highlight chromatin within cells. Additionally, a library of the scattering profiles of the various cellular components can be compiled for integration into the scattering model.

Finally, the effect of residual hemoglobin absorption should be incorporated into the current scattering model. A simple Beer-Lambert approximation can incorporate blood absorption into the spectrum, and the effects of scattering from blood cells should also be explored.

Based on the results of this dissertation, a multicolor polarized imaging device is currently being constructed. Imaging devices are not limited to a small area of tissue, but can survey a large region within the oral cavity. Areas that show high abnormality can be highlighted in the image, thus directing point spectroscopy measurements, which can determine whether a biopsy is warranted. The work presented in this dissertation lays the foundation for the development of imaging devices, and for the study and improvement of the sensitivity and specificity of polarized reflectance spectroscopy as a diagnostic modality.

APPENDIX

New Probe Design

A.1 FIBER PROBE

All parts stainless steel. All measurements in millimeters, square brackets contain measurements in inches.

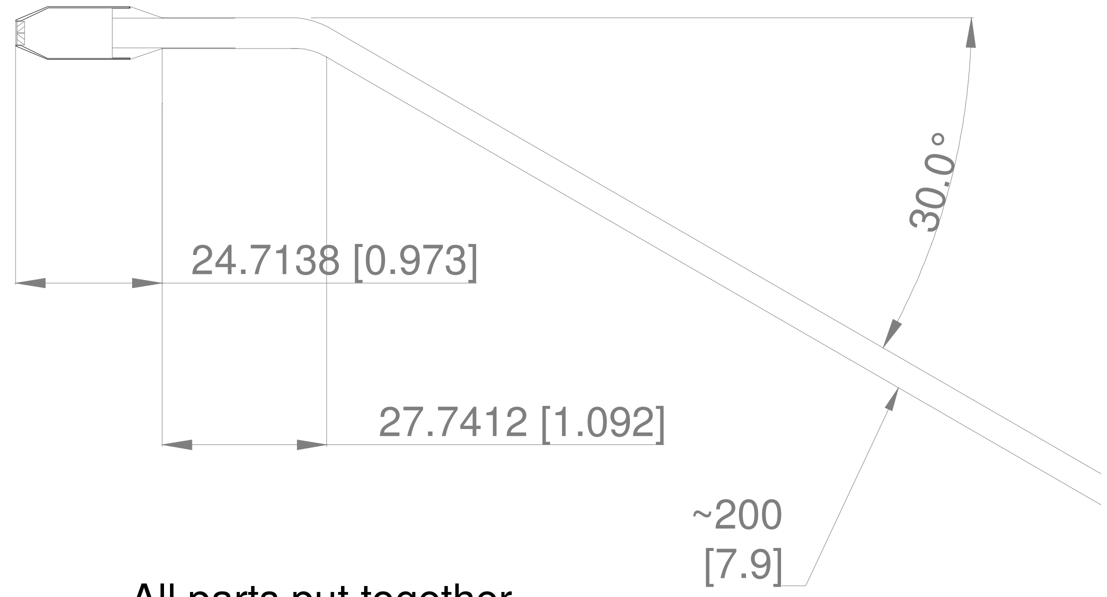

All parts put together

A.2 FIBER DISK HOLDER

Fiber disk holder to mount collection fibers at the desired angle. Six fibers can be inserted into each slot.

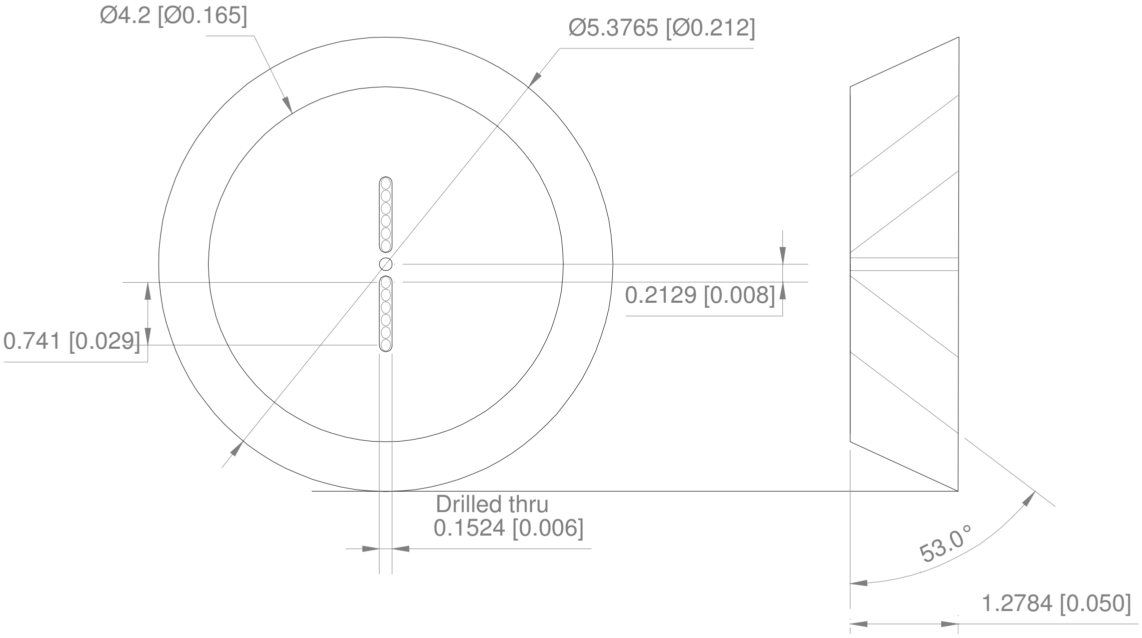

A.3 TOP VIEW OF DISTAL END OF FIBER PROBE

Top view of fiber probe with the fiber disk holder removed.

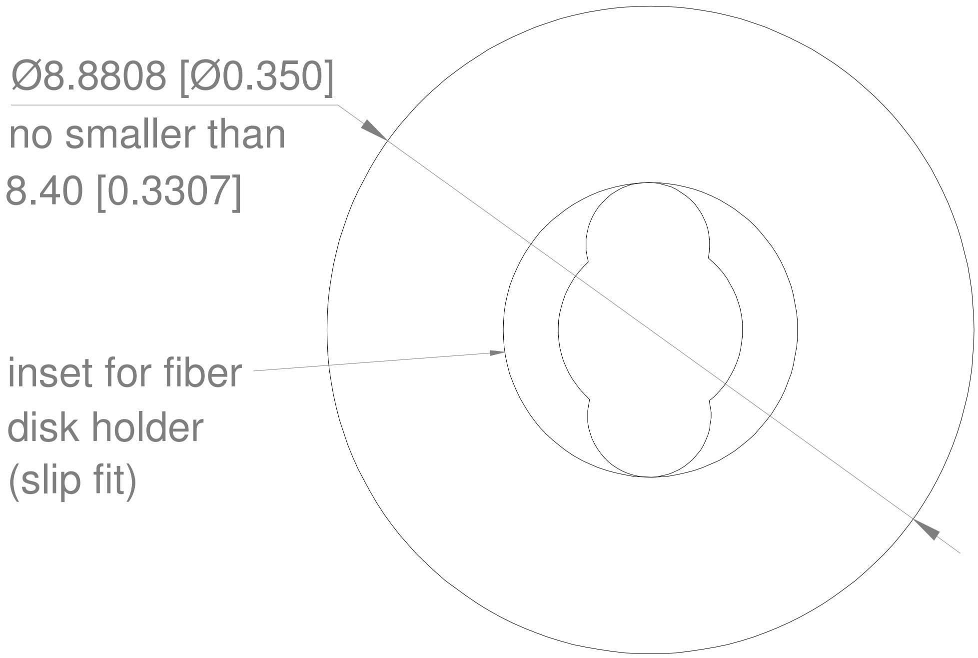

A.4 SIDE VIEW OF DISTAL END OF FIBER PROBE

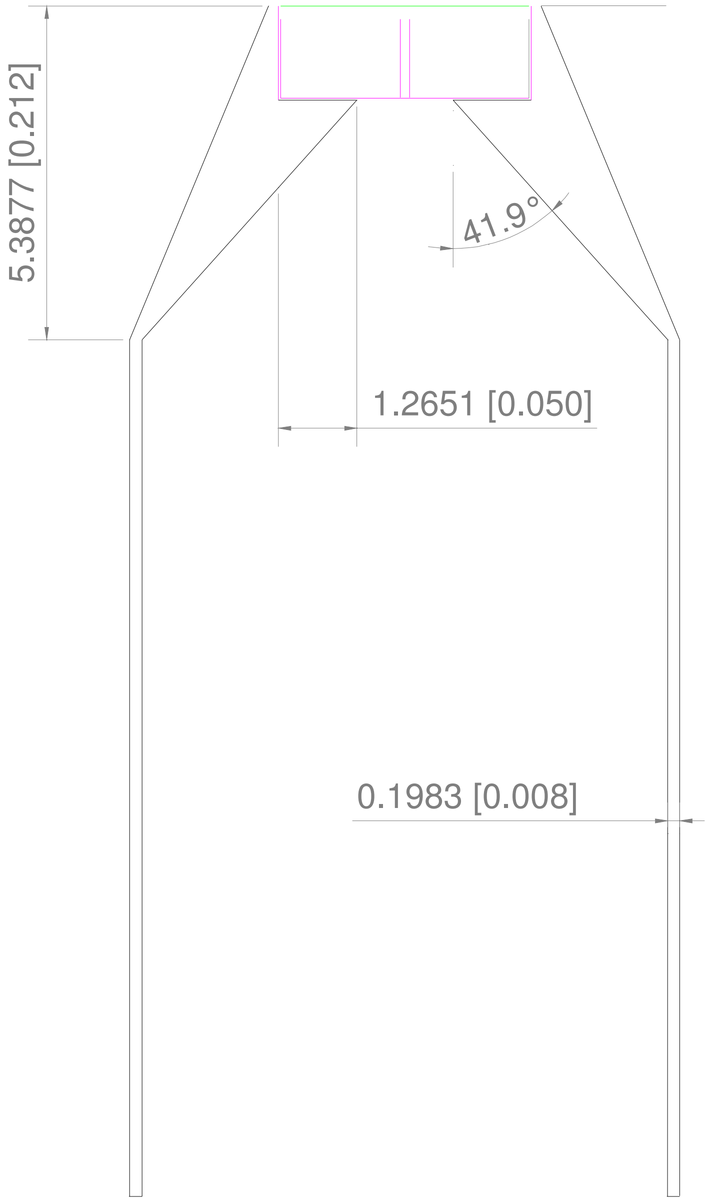

A.5 ALL PARTS AT DISTAL END

Pink lines indicate the bending radii of 100 micron core fibers. Blue lines indicate where the hollow tube, or handle, begins. Green lines indicate the position of an optical window.

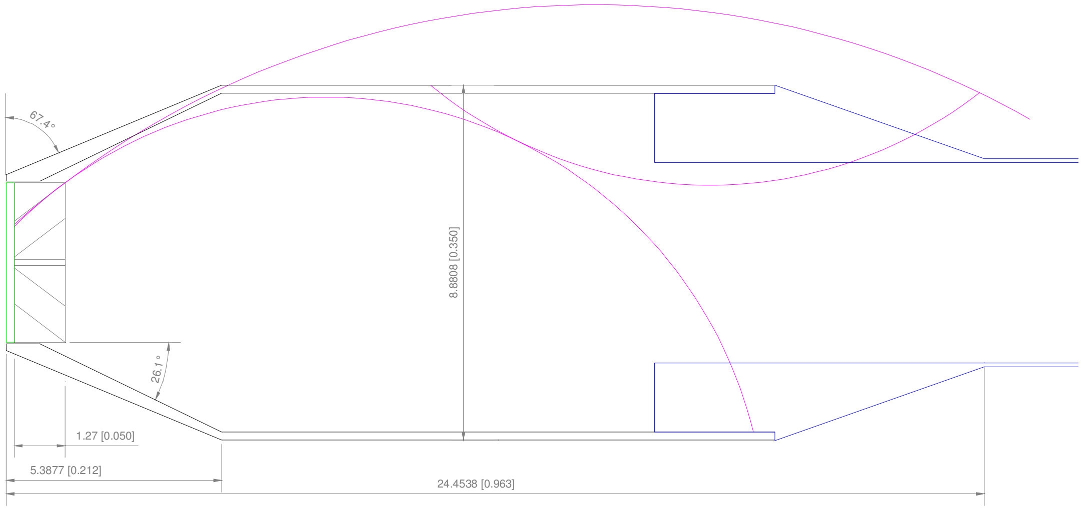

REFERENCES

1. Crawford, W.H., *Chapter 13: Mucosa: Cancer and premalignant diseases*. 2002.
2. Richards-Kortum, R. and E. Sevick-Muraca, *Quantitative optical spectroscopy for tissue diagnosis.* Annual Review of Physical Chemistry, 1996. **47**: p. 555-606.
3. Society, A.C., *Cancer Facts & Figures*. 2004.
4. http://www.adam.com. 2004.
5. Martini, F.H., *Fundamentals of Anatomy & Physiology*. Fifth ed. 2001, Upper Saddle River, N.J.: Prentice Hall.
6. Sciubba, J.J., *Oral cancer and its detection.* Journal of the American Dental Association, 2001. **132**: p. 12S-18S.
7. Scully, C. and S. Porter, *ABC of oral health: Swellings and red, white, and pigmented lesions.* British Medical Journal, 2000. **321**: p. 225-228.
8. http://omlc.ogi.edu/, *Oregon Laser Medical Center.*
9. http://www.microscopy.fsu.edu.
10. Cotran, R., V. Kumar, and S. Robbins, *Pathologic basis of disease*. 5th ed. 1994: W.B. Saunders Co. ch. 7.
11. Organization, W.H., *Cancer incidence, mortality, and prevalence worldwide*, in *Globocan 2000*, I.A.f.R.o. Cancer, Editor.
12. Sciubba, J.J., *Oral cancer: The importance of early diagnosis and treatment.* American Journal of Clinical Dermatology, 2001. **2**(4): p. 239-251.
13. Moore, S.R., N.W. Johnson, A.M. Pierce, and D.F. Wilson, *The epidemiology of mouth cancer: a review of global incidence.* Oral Diseases, 2000. **6**(2): p. 65-74.

14. Barasch, A., M. Safford, and E. Eisenberg, *Oral cancer and oral effects of anticancer therapy.* Mount Sinai journal of medicine, New York, 1998. **65**(5-6): p. 370-7.

15. Silverman, S., *Oral Cancer*. 1998, Hamilton, ON: American Cancer Society.

16. http://www3.cancer.org, *American Cancer Society*.

17. Silverman, S. and P.B. Sugerman, *Oral Premalignancies and Squamous Cell Carcinoma.* Clinics in Dermatology, 2000. **18**(5): p. 563-568.

18. Pavlova, I., K. Sokolov, R. Drezek, A. Malpica, M. Follen, and R. Richards-Kortum, *Microanatomical and biochemical origins of normal and precancerous cervical autofluorescence using laser-scanning fluorescence confocal microscopy.* Photochemistry and Photobiology, 2003. **77**(5): p. 550-5.

19. Drezek, R., C. Brookner, I. Pavlova, I. Boiko, A. Malpica, R. Lotan, M. Follen, and R. Richards-Kortum, *Autofluorescence microscopy of fresh cervical-tissue sections reveals alterations in tissue biochemistry with dysplasia.* Photochemistry and Photobiology, 2001. **73**(6): p. 636-41.

20. Georgakoudi, I., E. Sheets Ellen, G. Muller Markus, V. Backman, P. Crum Christopher, K. Badizadegan, R. Dasari Ramachandra, and S. Feld Michael, *Trimodal spectroscopy for the detection and characterization of cervical precancers in vivo.* American Journal of Obstetrics and Gynecology, 2002. **186**(3): p. 374-82.

21. Sciubba, J.J., *Oral Leukoplakia.* Crit Rev Oral Biol Med, 1995. **6**: p. 147-160.

22. Silverman, S. and R.D. Rosen, *Observation on the clinical characteristics and natural history of oral leukoplakia.* Journal of the American Dental Association, 1968. **76**(4): p. 772-777.

23. Silverman, S., Jr., M. Gorsky, and F. Lozada, *Oral leukoplakia and malignant transformation. A follow-up study of 257 patients.* Cancer, 1984. **53**(3): p. 563-8.

24. Goodman, H.S., J.A. Yellowitz, and A.M. Horowitz, *Oral cancer prevention. The role of family practitioners.* Archives of Family Medicine, 1995. **4**: p. 628-636.

25. Warnakulasuriya, K.A.A.S.W., *Sensitivity and specificity of OraScan toluidine blue mouthrinse in the detection of oral cancer and precancer.* Journal of Oral Pathology and Medicine, 1996. **25**: p. 97-103.

26. Sciubba, J.J., *Improving detection of precancerous and cancerous oral lesions: Computer-assisted analysis of the oral brush biopsy.* Journal of the American Dental Association, 1999. **130**: p. 1445-1457.

27. Gillenwater, A., R. Jacob, and R. Richards-Kortum, *Fluorescence spectroscopy: A technique with potential to improve the early detection of aerodigestive tract neoplasia.* Head & Neck, 1998. **20**: p. 556-562.

28. Heintzelman, D.L., U. Utzinger, H. Fuchs, A. Zuluaga, K. Gossage, A.M. Gillenwater, R. Jacob, B. Kemp, and R.R. Richards-Kortum, *Optimal excitation wavelengths for in vivo detection of oral neoplasia using fluorescence spectroscopy.* Photochemistry and Photobiology, 2000. **72**: p. 103-113.

29. Muller, M.G., T.A. Valdez, I. Georgakoudi, V. Backman, C. Fuentes, S. Kabani, N. Laver, Z. Wang, C.W. Boone, R.R. Dasari, S.M. Shapshay, and M.S. Feld, *Spectroscopic detection and evaluation of morphologic and biochemical changes in early human oral carcinoma.* Cancer, 2003. **97**(7): p. 1681-92.

30. Svistun, E., R. Alizadeh-Naderi, A. El-Naggar, R. Jacob, A. Gillenwater, and R. Richards-Kortum, *Vision enhancement system for detection of oral cavity neoplasia based on autofluorescence.* Head & Neck, 2004. **26**: p. 205-215.

31. Jullien, J.A., M.C. Downer, J.M. Zakrzewska, and P.M. Speight, *Evaluation of a screening test for the early detection of oral cancer and precancer.* Community Dent Health, 1995. **12**(3-7).

32. Dunn, A., C. Smithpeter, A.J. Welch, and R. Richards-Kortum, *FDTD simulation of light scattering from single cells.* Journal of Biomedical Optics, 1997. **2**: p. 262-266.

33. Drezek, R., A. Dunn, and R. Richards-Kortum, *Light scattering from cells: finite-difference time-domain simulations and goniometric measurements.* Applied Optics, 1999. **38**(16): p. 3651-3661.

34. Mourant, J.R., J.P. Freyer, A.H. Hielscher, A.A. Eick, D. Shen, and T.M. Johnson, *Mechanism of light scattering from biological cells relevant to noninvasive optical-tissue diagnositics.* Applied Optics, 1998. **37**: p. 3586-3593.

35. Brunsting, A. and P.F. Mullaney, *Differential light scattering from spherical mammalian cells.* Biophysical Journal, 1974. **14**(6): p. 439-453.

36. Sokolov, K., R. Drezek, K. Gossage, and R. Richards-Kortum, *Reflectance Spectroscopy with Polarized Light: Is it Sensitive to Cellular and Nuclear Morphology.* Optics Express, 1999. **5**(13): p. 302-317.

37. Myakov, A., L. Nieman, L. Wicky, U. Utzinger, R. Richards-Kortum, and K. Sokolov, *Fiber optic probe for polarized reflectance spectroscopy in vivo: design and performance.* Journal of Biomedical Optics, 2002. **7**(3): p. 388-97.

38. Nieman, L., A. Myakov, J. Aaron, and K. Sokolov, *Optical sectioning using a fiber probe with an angled illumination-collection geometry: evaluation in engineered tissue phantoms.* Applied optics, 2004. **43**(6): p. 1308-19.

39. Backman, V., M.B. Wallace, L.T. Perelman, J.T. Arendt, R. Gurjar, M.G. Muller, Q. Zhang, G. Zonios, E. Kline, J.A. McGilligan, S. Shapshay, T. Valdez, K. Badizadegan, J.M. Crawford, M. Fitzmaurice, S. Kabani, H.S. Levin, M. Seiler, R.R. Dasari, I. Itzkan, J. Van Dam, M.S. Feld, and T. McGillican, *Detection of preinvasive cancer cells.* Nature, 2000. **406**(6791): p. 35-6.
40. Drezek, R., M. Guillaud, T. Collier, I. Boiko, A. Malpica, C. Macaulay, M. Follen, and R. Richards-Kortum, *Light scattering from cervical cells throughout neoplastic progression: influence of nuclear morphology, DNA content, and chromatin texture.* Journal of Biomedical Optics, 2003. **8**(1): p. 7-16.
41. Mourant, J.R., T.M. Johnson, and J.P. Freyer, *Characterizing mammalian cells and cell phantoms by polarized backscattering fiber-optic measurements.* Applied Optics, 2001. **40**: p. 5114-5123.
42. Schmitt, J.M. and G. Kumar, *Optical scattering properties of soft tissue: a discrete particle model.* Applied Optics, 1998. **37**: p. 2788-2797.
43. Backman, V., M.B. Wallace, L.T. Perelman, J.T. Arendt, R. Gurjar, M.G. Muller, Q. Zhang, G. Zonios, E. Kline, T. McGillican, S. Shapshay, T. Valdez, K. Badizadegan, J.M. Crawford, M. Fitzmaurice, S. Kabani, H.S. Levin, M. Seiler, R.R. Dasari, I. Itzkan, J. Van Dam, and M.S. Feld, *Cancer screening: Detection of preinvasive cancer cells.* Nature (London), 2000. **406**(6791): p. 35-36.
44. Bigio, I.J., J.R. Mourant, J.D. Boyer, T.M. Johnson, T. Shimada, and R.L. Conn. *Noninvasive Identification of Bladder Cancer with Subsurface Backscattered Light*. in *Advances in Laser and Light Spectroscopy to Diagnose Cancer and Other Diseases*. 1994. Los Angeles, CA.

45. Mourant, J.R., I.J. Bigio, J. Boyer, R.L. Conn, T. Johnson, and T. Shimada, *Spectroscopic diagnosis of bladder cancer with elastic light scattering.* Lasers in Surgery and Medicine, 1995. **17**(4): p. 350-7.

46. Sokolov, K., K.-B. Sung, T. Collier, A. Clark, D. Arifler, A. Lacy, M. Descour, and R. Richards-Kortum, *Endoscopic microscopy.* Disease markers, 2002. **18**(5-6): p. 269-91.

47. Sung, K.-B., C. Liang, M. Descour, T. Collier, M. Follen, and R. Richards-Kortum, *Fiber-optic confocal reflectance microscope with miniature objective for in vivo imaging of human tissues.* IEEE transactions on bio-medical engineering, 2002. **49**(10): p. 1168-72.

48. Ramanujam, N., *Fluorescence spectroscopy of neoplastic and non-neoplastic tissues.* Neoplasia, 2000. **2**(1-2): p. 89-117.

49. Bigio, I.J. and J.R. Mourant, *Ultraviolet and visible spectroscopies for tissue diagnostics: fluorescence spectroscopy and elastic-scattering spectroscopy.* Physics in Medicine and Biology, 1997. **42**(5): p. 803-14.

50. Georgakoudi, I., B.C. Jacobson, J. Van Dam, V. Backman, M.B. Wallace, M.G. Muller, Q. Zhang, K. Badizadegan, D. Sun, G.A. Thomas, L.T. Perelman, and M.S. Feld, *Fluorescence, reflectance, and light-scattering spectroscopy for evaluating dysplasia in patients with Barrett's esophagus.* Gastroenterology, 2001. **120**(7): p. 1620-9.

51. Zonios, G., L.T. Perelman, V. Backman, R. Manoharan, M. Fitzmaurice, J. Van Dam, and F. M.S., *Diffuse reflectance spectroscopy of human adenomatous colon polyps in vivo.* Applied Optics, 1999. **38**: p. 6628-37.

52. Perelman, L.T., V. Backman, M. Wallace, G. Zonios, R. Manoharan, A. Nusrat, S. Shields, M. Seiler, C. Lima, T. Hamano, I. Itzkan, J.V. Dam, J.M. Crawford, and M.S. Feld, *Observation of Periodic Fine Structure in Reflectance from Biological Tissue: A New Technique for Measuring Nuclear Size Distribution.* Physical Review Letters, 1998. **80**: p. 627-630.

53. Backman, V., R. Gurjar, K. Badizadegan, I. Itzkan, R.R. Dasari, L.T. Perelman, and M.S. Feld, *Polarized light scattering spectroscopy for quantitative measurement of epithelial cellular structures in situ.* IEEE Journal of Selected Topics in Quantum Electronics, 1999. **5**(4): p. 1019-1026.

54. Mourant, J.R., T.M. Johnson, S. Carpenter, A. Guerra, T. Aida, and J.P. Freyer, *Polarized angular dependent spectroscopy of epithelial cells and epithelial cell nuclei to determine the size scale of scattering structures.* Journal of Biomedical Optics, 2002. **7**(3): p. 378-87.

55. Jacques, S.L., J.R. Roman, and K. Lee, *Imaging Superficial Tissues with Polarized Light.* Lasers Surg. Med., 2000. **26**: p. 119-129.

56. Anderson, R.R., *Polarized light examination and photography of the skin.* Archives of Dermatology, 1991. **127**(7): p. 1000-5.

57. Chandrasekhar, S., *Radiative Transfer*. 1960, New York: Dover.

58. Ishimaru, A., *Wave propagation and scattering in random media*. Vol. 1, 2. 1978, New York: Academic.

59. Welch, A.J. and M.J.C.v. Gemert, eds. *Optical-Thermal Response of Laser-Irradiated Tissue*. Lasers, Photonics, and Electro-Optics, ed. H. Kogelnik. 1995, Plenum Press: New York.

60. Asano, S., *Light scattering properties of spheroidal particles.* Applied Optics, 1979. **18**(5): p. 712-723.

61. Bohren, C.F. and D.R. Huffman, *Absorption and Scattering of Light by Small Particles*. 1998, New York: John Wiley & Sons, Inc.

62. Hulst, H.C.v.d., *Light Scattering by Small Particles*. 1957, New York: Dover.

63. Watson, J.V., *Flow Cytometry Data Analysis : Basic Concepts and Statistics*. 1992, Cambridge, New York: Cambridge University Press.

64. Givan, A.L., *Flow Cytometry: First Principles*. 2001, New York: Wiley-Liss.

65. Dunn, A. and R. Richards-Kortum, *Three-dimensional computation of light scattering from cells.* IEEE Journal on Selected Topics in Quantum Electronics, 1996. **2**(4): p. 898-905.

66. Drezek, R., A. Dunn, and R. Richards-Kortum, *A pulsed FDTD method for calculating light scattering from cells over broad wavelength ranges.* Optics Express, 2000. **6**(7): p. 147-157.

67. Mourant, J.R., T.M. Johnson, V. Doddi, and J.P. Freyer, *Angular dependent light scattering from multicellular spheroids.* Journal of Biomedical Optics, 2002. **7**(1): p. 93-9.

68. Mourant, J.R., M. Canpolat, C. Brocker, O. Esponda-Ramos, T.M. Johnson, A. Matanock, K. Stetter, and J.P. Freyer, *Light scattering from cells: the contribution of the nucleus and the effects of proliferative status.* Journal of Biomedical Optics, 2000. **5**(2): p. 131-7.

69. Chen, Z., A. Taflove, and V. Backman, *Equivalent volume-averaged light scattering behavior of randomly inhomogeneous dielectric spheres in the resonant range.* Optics Letters, 2003. **28**(10): p. 765-7.

70. Demos, S.G. and R.R. Alfano, *Optical polarization imaging.* Applied Optics, 1997. **36**(1): p. 150-155.

71. Jacques Steven, L., C. Ramella-Roman Jessica, and K. Lee, *Imaging skin pathology with polarized light.* Journal of Biomedical Optics, 2002. **7**(3): p. 329-40.

72. Johnson, T.M. and J.R. Mourant, *Polarized wavelength-dependent measurements of turbid media.* Optics Express, 1999. **4**: p. 200-216.

73. Mourant, J.R., T. Fuselier, J. Boyer, T.M. Johnson, and I.J. Bigio, *Predictions and measurements of scattering and absorption over broad wavelength ranges in tissue phantoms.* Applied Optics, 1997. **36**(4): p. 949-957.

74. Asano, S. and M. Sato, *Light scattering by randomly oriented spheroidal particles.* Applied Optics, 1980. **19**(6): p. 962-74.

75. Bicout, D., C. Brosseau, A.S. Martinez, and J.M. Schmitt, *Depolarization of multiply scattered waves by spherical diffusers: influence of the size parameter.* Physical Review E: Statistical Physics, Plasmas, Fluids, and Related Interdisciplinary Topics, 1994. **49**(2): p. 1767-70.

76. Sankaran, V., K. Schonenberger, J.T. Walsh, and D.J. Maitlant, *Polarization descrimination of coherently propagating light in turbid media.* Applied Optics, 1999. **38**: p. 4252-4261.

77. Sankaran, V., T. Walsh Joseph, Jr., and J. Maitland Duncan, *Comparative study of polarized light propagation in biologic tissues.* Journal of biomedical optics, 2002. **7**(3): p. 300-6.

78. Jarry, G., E. Steimer, V. Damaschini, M. Epifanie, M. Jurczak, and R. Kaiser, *Coherence and polarization of light propagating through scattering media and biological tissues.* Applied Optics, 1998. **37**: p. 7357-7367.

79. Demos, S.G. and R.R. Alfano, *Temporal gating in highly scattering media by the degree of optical polarization.* Optics Letters, 1996. **21**(2): p. 161-163.

80. Kim, Y.L., Y. Liu, R.K. Wali, H.K. Roy, M.J. Goldberg, A.K. Kromin, K. Chen, and V. Backman, *Simultaneous measurement of angular and spectral properties of light scattering for characterization of tissue microarchitecture and its alteration in early precancer.* IEEE Journal of Selected Topics in Quantum Electronics, 2003. **9**(2): p. 243-256.

81. Hielscher, A.H., J.R. Mourant, and I.J. Bigio, *Influence of particle size and concentration on the diffuse backscattering of polarized light from tissue phantoms and biological cell suspensions.* Applied Optics, 1997. **36**(1): p. 125-143.

82. Mourant, J.R., A.H. Hielscher, A.A. Eick, T.M. Johnson, and J.P. Freyer, *Evidence of intrinsic differences in the light scattering properties of tumorigenic and nontumorigenic cells.* Cancer, 1998. **84**(6): p. 366-74.

83. Sokolov, K., M. Follen, and R. Richards-Kortum, *Optical spectroscopy for detection of neoplasia.* Current Opinion in Chemical Biology, 2002. **6**(5): p. 651-658.

84. Hong, W.K. and M.B. Sporn, *Recent advances in chemoprevention of cancer.* Science (Washington, D. C.), 1997. **278**(5340): p. 1073-1077.

85. Streuli, C., *Extracellular matrix remodelling and cellular differentiation.* Current Opinion in Cell Biology, 1999. **11**(5): p. 634-640.

86. Georgakoudi, I., B.C. Jacobson, M.G. Muller, E.E. Sheets, K. Badizadegan, D.L. Carr-Locke, C.P. Crum, C.W. Boone, R.R. Dasari, J. Van Dam, and M.S. Feld, *NAD(P)H and collagen as in vivo quantitative fluorescent biomarkers of epithelial precancerous changes.* Cancer Research, 2002. **62**(3): p. 682-687.

87. Quan, L. and N. Ramanujam, *Relationship between depth of target in a turbid medium and fluorescence measured by a variable-aperture method.* Optics Letters, 2002. **27**: p. 104-106.

88. Pfefer, T.J., T. Schomacker Kevin, N. Ediger Marwood, and S. Nishioka Norman, *Multiple-fiber probe design for fluorescence spectroscopy in tissue.* Appl Opt, 2002. **41**(22): p. 4712-21.

89. Utzinger, U. and R. Richards-Kortum Rebecca, *Fiber optic probes for biomedical optical spectroscopy.* Journal of Biomedical Optics, 2003. **8**(1): p. 121-47.

90. White, W.M., M. Rajadhyaksha, S. Gonzalez, R.L. Fabian, and R.R. Anderson, *Noninvasive Imaging of Human Oral Mucosa In Vivo by Confocal Reflectance Microscopy.* Laryngoscope, 1999. **109**(10): p. 1709-1717.

91. Sokolov, K., J. Galvan, A. Myakov, A. Lacy, R. Lotan, and R. Richards-Kortum, *Realistic three-dimensional epithelial tissue phantoms for biomedical optics.* Journal of Biomedical Optics, 2002. **7**(1): p. 148-56.

92. Collier, T., D. Arifler, A. Malpica, M. Follen, and R. Richards-Kortum, *Determination of epithelial tissue scattering coefficient using confocal microscopy.* IEEE Journal of Selected Topics in Quantum Electronics, 2003. **9**(2): p. 307-313.

93. Takaha, N., L. Hawkins Anita, A. Griffin Constance, B. Isaacs William, and S. Coffey Donald, *High mobility group protein I(Y): a candidate architectural*

protein for chromosomal rearrangements in prostate cancer cells. Cancer Research, 2002. **62**(3): p. 647-51.

94. Koss, L.G., *Diagnostic Cytology and Its Histopathologic Bases*. 1992, Philadelphia: Lippincott.

95. Guillaud, M., A. Doudkine, D. Garner, C. MacAulay, and B. Palcic, *Malignancy associated changes in cervcial smears: systematic changes in cytometric features with the grade of dysplasia.* Anal. Cell. Pathol., 1995. **9**(3): p. 191-204.

96. Saidi, I.S., S.L. Jacques, and F.K. Tittel, *Mie and Rayleigh modeling of visible-light scattering in neonatal skin.* Applied Optics, 1995. **34**(31): p. 7410-7418.

97. Collier, T., A. Lacy, R. Richards-Kortum, A. Malpica, and M. Follen, *Near Real-Time Confocal Microscopy of Amelanotic Tissue: Detection of Dysplasia in ex Vivo Cervical Tissue.* Academic Radiology, 2002. **9**(5): p. 504-512.

98. Arifler, D., M. Guillaud, A. Carraro, A. Malpica, M. Follen, and R. Richards-Kortum, *Light scattering from normal and dysplastic cervical cells at different epithelial depths: finite-difference time-domain modeling with a perfectly matched layer boundary condition.* Journal of biomedical optics, 2003. **8**(3): p. 484-94.

VITA

Linda Tae Nieman was born in Lincoln Park, Michigan on February 10, 1973, the daughter of Michael Steven Nieman and Yuko Kasahara Nieman. After graduating from Oscar A. Carlson High School, she entered The University of Michigan-Dearborn. She graduated in May 1997 with a Bachelor of Science degree in physics. During those years she participated in nuclear physics research under the supervision of Dr. Aruna Nadasen and received the 1996 Physics Honors Scholar award. In September 1997, she entered The Graduate School of The University of Texas Austin to pursue a Doctorate of Physics. She obtained a Master of Arts in Physics in 2000 under the supervision of Robert Martinez. After receiving her M.A., she continued work on her Doctorate under the supervision of Konstantin Sokolov.

Permanent address: 29249 Glen Oaks Blvd., Farmington Hills, MI 48334

This dissertation was typed by the author.